J. Fluid Mech. (2001), *vol.* 432, *pp.* 219–283. Printed in the United Kingdom

The structure of weakly compressible grid-generated turbulence

By G. BRIASSULIS, J. H. AGUI† AND Y. ANDREOPOULOS

Experimental Aerodynamics and Fluid Mechanics Laboratory, Department of Mechanical Engineering, The City College of the City University of New York, New York, NY 10031, USA.

(Received 26 January 1999 and in revised form 2 October 2000)

A decaying compressible nearly homogeneous and nearly isotropic grid-generated turbulent flow has been set up in a large scale shock tube research facility. Experiments have been performed using instrumentation with spatial resolution of the order of 7 to 26 Kolmogorov viscous length scales. A variety of turbulence-generating grids provided a wide range of turbulence scales with bulk flow Mach numbers ranging from 0.3 to 0.6 and turbulent Reynolds numbers up to 700. The decay of Mach number fluctuations was found to follow a power law similar to that describing the decay of incompressible isotropic turbulence. It was also found that the decay coefficient and the decay exponent decrease with increasing Mach number while the virtual origin increases with increasing Mach number. A possible mechanism responsible for these effects appears to be the inherently low growth rate of compressible shear layers emanating from the cylindrical rods of the grid. Measurements of the time-dependent, three dimensional vorticity vectors were attempted for the first time with a 12-wire miniature probe. This also allowed estimates of dilatation, compressible dissipation and dilatational stretching to be obtained. It was found that the fluctuations of these quantities increase with increasing mean Mach number of the flow. The time-dependent signals of enstrophy, vortex stretching/tilting vector and dilatational stretching vector were found to exhibit a rather strong intermittent behaviour which is characterized by high-amplitude bursts with values up to 8 times their r.m.s. within periods of less violent and longer lived events. Several of these bursts are evident in all the signals, suggesting the existence of a dynamical flow phenomenon as a common cause.

1. Introduction

A fundamental understanding of compressible turbulence in the absence of shock wave interactions is necessary for the development of supersonic transport aircraft, combustion processes, and high-speed rotor flows. Compressibility effects on turbulence are significant when the energy associated with dilatational fluctuations is large or when the mean flow is compressed or expanded. Most of the previous work on compressible turbulence has been carried out in shear layers (see Gutmark, Schadow & Yu 1995, for the most recent review on compressible free shear flows) or boundary layers (see Spina, Smits & Robinson 1994). Previous work on homogeneous and isotropic compressible turbulence (see figure 1 for a typical flow schematic) is very limited although this flow is the best candidate for testing calculation methods and turbulence modelling. The reader is referred to the work by Lele (1994) where different contributions to the understanding of compressibility effects on turbulence

† Present address: NASA Glenn Research Center, Cleveland, OH 44135, USA.

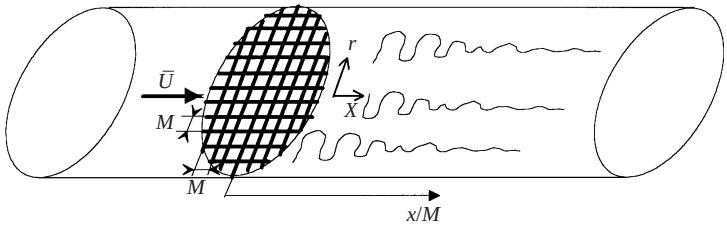

FIGURE 1. Grid-generated flow schematic.

are reviewed in detail. A substantial amount of experimental work dealing with the *incompressible* grid-generated turbulence already exists (see Compte-Bellot & Corrsin 1966, 1971). The effect of grids and perforated plates as flow straighteners on the free stream turbulence was studied by Tan-Atichat, Nagib & Loehrke (1982) for Reynolds number based on mesh size Re_M up to 735. They found that the performance of the grid depends on the characteristics of the incoming flow. For a larger range of mesh Reynolds number Re_M ranging from 12800 to 81000, Frenkiel, Klebanoff & Huang (1979) performed experiments where they observed that data exhibited a high degree of similarity. Their analysis of the higher-order correlations and moments of the turbulent velocity components revealed that the turbulent fluctuations are of non-Gaussian character. Tavoularis, Bennett & Corrsin (1978) presented a comprehensive study of values of the skewness of velocity derivative for a variety of flow fields and Re_λ. This study indicated that the skewness of the velocity derivative reaches a maximum at $Re_\lambda = 5$ and then gradually decreases as the turbulent Reynolds number increases.

Grid turbulence at large mesh Reynolds number (1.2×10^5 to 2.4×10^6) was studied by Kistler & Vrebalovich (1966). To avoid compressibility effects the mean flow was kept below $60\,\mathrm{m\,s^{-1}}$. From the literature review it is evident that in all of the above studies on grid-generated turbulence compressibility effects were absent or undesirable. One of the first attempts to generate compressible isotropic turbulence was described by Honkan & Andreopoulos (1992) and Honkan, Watkins & Andreopoulos (1994) who set up a flow with $Re_\lambda \approx 1000$. Recently Budwig *et al.* (1995) and Zwart, Budwig & Tavoularis (1997) worked on compressible streams with three different Mach numbers in a supersonic wind tunnel. The decay coefficient for the lowest Mach number of 0.16 was found to be -1.24, and -0.49 for the highest Mach number of 1.6. However, inhomogeneity across the test section prevented them from measuring decaying turbulence at high Mach numbers.

The present experimental work is a fundamental study of compressibility effects in grid-generated turbulence for flows with Mach numbers ranging from 0.3 to 0.6. The measurements were carried out inside the induced flow behind a travelling shock wave in a shock tube facility. Time-dependent measurements of one, two and three velocity components have been carried out. Measurements of the vorticity vector and the full dissipation tensor at a limited number of locations inside the flow have been also attempted for the first time in compressible flows.

In the present work there is no shock wave interaction with the flow which causes sudden compression of the flow field, as there was in our previous work (Briassulis & Andreopoulos 1994, 1996).

2. Experimental set-up

The experiments were performed in the Shock Tube Research Facility (STURF), shown in figure 2(*a*), which is located at the Mechanical Engineering Department of

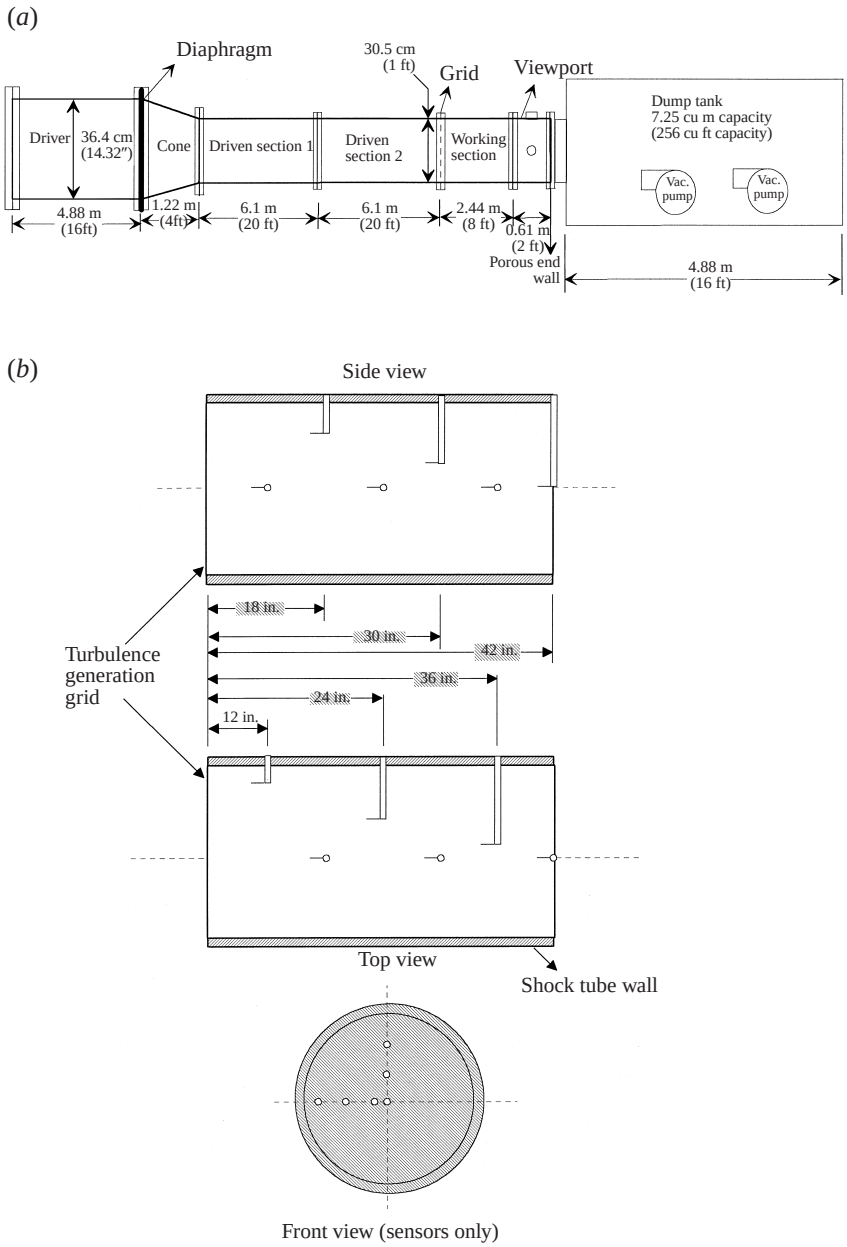

FIGURE 2. (*a*) Shock tube research facility (not to scale). (*b*) X-wire probe location and arrangement in the shock tube.

CCNY. The large dimensions of this facility, 1 ft in diameter and 88 ft in length, provide an excellent platform for high-spatial-resolution measurements of turbulence with long observation time of steady flow. The induced flow behind the travelling shock wave passes through a turbulence-generating grid installed in the beginning of the working section of the facility. Several turbulence-generating grids were used at three different flow Mach numbers. The velocity of the induced flow behind the shock wave depends on the rupture pressure of the diaphragm, i.e. driver strength.

The working (test) section is fitted with several hot-wire and pressure ports. Thus pressure, velocity and temperature data can be acquired simultaneously at various locations downstream from the grid (see figure 2*b*), therefore reducing the variance between measurements. High-frequency pressure transducers, hot-wire anemometry and Rayleigh scattering techniques for flow visualization have been used in the present investigation.

To assess the flow quality in the facility several tests were carried out. First the shock wave was visualized in order to check its inclination and planform by a non-intrusive optical technique using a Nd:YAG laser emitting in the UV range and a UV sensitive 16 bit CCD camera made by ASTROMED Corporation. Second the flow homogeneity was checked by a hot-wire rake constructed for simultaneous acquisition of velocity and temperature data at various radial positions. Details of an extensive evaluation of the flow quality can be found in the work of Briassulis *et al.* (1996) while quantitative results are presented in § 4 below.

To simultaneously resolve two-dimensional velocity components with hot wires, a cross-wire (X-wire) arrangement was used. New three-wire probes were designed and custom built by AUSPEX Corp. Six different three-wire probe assemblies were used concurrently at different downstream locations, all adjustable to different lengths, each carrying two hot wires in an X configuration and one cold wire for simultaneous velocity and temperature measurements respectively. The three-wire probes were equipped with 5 μm platinum/tungsten wires for velocity measurements and with a 2.5 μm platinum/tungsten wire for temperature measurements. To eliminate any wake effects from probes located upstream, all of the probes were staggered at increasing distances from the tube wall with downstream station and every other probe reoriented by 90° by using two axial array of probe taps along the test section. The cross-wires were driven by DANTEC anemometers model CTA56C01 and the temperature wires were connected to EG&G model 113 low-noise, battery-operated pre-amplifiers/filters. The output signal of the cold wire was digitally compensated for thermal lag up to frequencies of interest. For more details on the hot-wire techniques applicable to shock tubes, see Briassulis *et al.* (1995) where estimates of uncertainties in the measurements are also given.

Time-dependent pressure fluctuations were obtained by 6 miniature high-frequency-response Kulite pressure transducers installed on the shock tube wall.

During each experiment all signals were acquired simultaneously with the ADTEK data acquisition system. The ADTEK AD830 board is a 12-bit EISA data acquisition system, capable of sampling simultaneously eight channels at 333 KHz each channel. Three of those boards are currently available providing 24 simultaneous sampled channels at 333 KHz per channel. It should be mentioned that no sample-and-hold units were used in the present data acquisition since each channel was dedicated to an individual analog to digital converter. The data acquisition system was triggered by the arrival of the shock wave at the location of a wall pressure transducer 0.30 m upstream of the grid. The grid was installed in the beginning of the working section.

This experimental set-up provided time-dependent measurements of two velocity components, temperature and wall pressure at several locations of the flow field simultaneously. In addition, time-dependent three-dimensional vorticity measurements were carried out by using a new vorticity probe (see Andreopoulos & Honkan 1996 and Honkan & Andreopoulos 1997). Details of this technique are given in § 5 below.

The bulk flow parameters of the experiments performed are summarized in table 1 and include the grid mesh density, the mesh size M, the flow Mach number M_{flow}, the Reynolds number Re_M based on mesh size and mean flow velocity U_1, the Reynolds

Grid (meshes/in.)	M (mm×mm)	σ	M_{flow}	Re_M	Re_λ (range)
5×5	5.1×5.1	0.37	0.371	59 654	160–318
5×5	5.1×5.1	0.37	0.477	86 315	200–269
5×5	5.1×5.1	0.37	0.576	102 421	240–458
4×4	6.35×6.35	0.44	0.354	68 208	213–401
4×4	6.35×6.35	0.44	0.446	105 389	198–336
4×4	6.35×6.35	0.44	0.594	132 921	113–352
3×3	8.5×8.5	0.39	0.321	81 687	154–239
3×3	8.5×8.5	0.39	0.474	124 203	184–201
3×3	8.5×8.5	0.39	0.564	215 043	330–747
2×2	12.7×12.7	0.38	0.346	137 319	186–281
2×2	12.7×12.7	0.38	0.436	169 025	195–452
2×2	12.7×12.7	0.38	0.592	261 667	560–1331
1.33×1.33	19.05×19.05	0.26	0.368	200 371	210–278
1.33×1.33	19.05×19.05	0.26	0.504	295 721	217–612
1.33×1.33	19.05×19.05	0.26	0.607	398 661	257–760

TABLE 1. Bulk flow parameters of the experiments performed.

number Re_λ based on Taylor's microscale λ, and the solidity of the grids σ, defined as the projected solid area per unit total area so that $\sigma = 1 - [1 - d/M]^2$ where d is the rod diameter. The range of values of Re_λ obtained in the isotropic part of the flow downstream of the grid is also shown in table 1. All grids were fabricated from circular steel rods.

The values of M_{flow} were obtained in the flow downstream of the grid and they are slightly smaller than the Mach number values obtained in the approaching flow upstream of the grid (see Honkan *et al.* 1994). As the incoming shock wave reaches the grid, it is transmitted through it with some minor losses due to viscous effects, while a very weak reflected shock travels as a small disturbance in the opposite direction upstream as a result of the impact of the incident shock on the grid. This weak disturbance is stronger at higher shock Mach numbers and in impacts with higher solidity grids. This weakly reflected shock reduces the velocity and increases the temperature of the approaching flow by small amounts. The induced flow behind the incident shock, after it has experienced the effects of the upstream travelling weakly reflected shock, passes through the grid to form a nearly homogeneous and isotropic flow.

3. The shock tube flow

Unlike conventional low-speed grid turbulence, generated in a wind tunnel, the present flow is produced in a shock tube behind a moving shock wave. Shock tubes are traditionally used to study mainly moving shock waves and their reflections or interactions with solid surfaces and to generate high temperature environments. Our work is not the first one to configure a stationary flow behind a moving shock wave. There have been several attempts in the past to utilize the induced flow behind the shock to study several flow phenomena. Oppenheimer for instance (Majda 1999, private communication) used a shock tube at Berkeley to establish several flow instabilities in the early 1950s. More recently, Hesselink & Sturtevant (1988), Keller & Merzkirch (1990) and Honkan & Andreopoulos (1992) used a shock tube to study the interaction between grid turbulence and a shock wave.

The duration of the induced flow behind the shock wave may be limited by the arrival of reflected expansion waves from the driver endwall which are formed during the rupture of the diaphragm, by the arrival of shock or expansion waves formed at the downstream endwall and the arrival of the contact surface which is characterized by a large temperature gradient.

The present shock tube has been designed to study interactions of turbulent flows, including the current one, with normal shock waves in the absence of streamline curvature (see Andreopoulos, Agui & Briassulis 2000). This facility has three distinguishing features. The most significant one is the ability to control the strength of the reflected shock and the flow quality behind it by using a removable porous endwall, placed at the flange between the dump tank and the working section. The impact of a shock wave on the endwall would result in a full normal shock reflection for zero porosity (solid wall), a weak shock reflection for moderate porosity, or expansion waves for infinite porosity (open endwall). The second feature of the facility is the ability to vary the total length of the driven section by adding or removing one of the several pieces or modules that are available or rearrange their lay-out. Proper arrangement of the lay-out of the various modules of the shock tube can maximize the duration of the useful flow. The third feature of the facility is its large diameter, which allows a large area of uniform flow in the absence of wall effects to be available while at the same time providing a platform for high spatial resolution in the measurements of turbulence.

Figure 3(*a*) shows the x–t diagram of the measured pressure data in a flow with a Mach number 0.7. The contours were obtained by interpolating the time-dependent signals of 12 wall pressure transducers installed at various locations along the driven and working sections. Figure 3(*b*) shows the corresponding theoretical x–t diagram obtained from one-dimensional theory. Also on figure 3(*b*), experimental data are plotted which are related to the arrival of the incident, and reflected shock waves and the reflected expansion waves. It appears that the agreement between experimental data and theoretical predictions for both the incident and reflected shock is good. The experimental data also suggest a shock speed which is always less than the theoretical one. In most facilities this is the case. Figure 3 can be used to obtain an estimate of the duration of the uniform induced flow behind the incident shock. As can be seen from the figure, at the location $x/L = 0.8$, which corresponds to the location of the working section, the duration of the flow bounded by the incident shock, the contact surface and the arrival of the expansion waves and reflected shock is about $tc_1/L = 0.2$ to 0.4 which indicates a 14 to 24 ms flow duration at this Mach number $M_{flow} = 0.7$.

Figure 4(*a*) shows typical signals of velocity and temperature, acquired in the present investigation, non-dimensionalized by the corresponding mean values obtained over the time of interest. The arrival of the incident and reflected shocks is also marked in this figure. It can be observed that the passage of the incident shock increases the velocity as well as the temperature of the induced flow while the passage of the reflected shock decreases the local velocity and increases the temperature. In principle, the time between the arrival of the incident shock and the arrival of its reflection over the endwall define the duration of data non-contaminated by interactions with shock waves or expansion waves. In the present case, this time appears to be about 14.5 ms. However, this time cannot be considered entirely as containing useful data because immediately after the incident shock the induced flow corresponds to the air mass located between the grid and the location of measurement before it was put into motion by the shock. This mass of air flow has not passed through the grid and

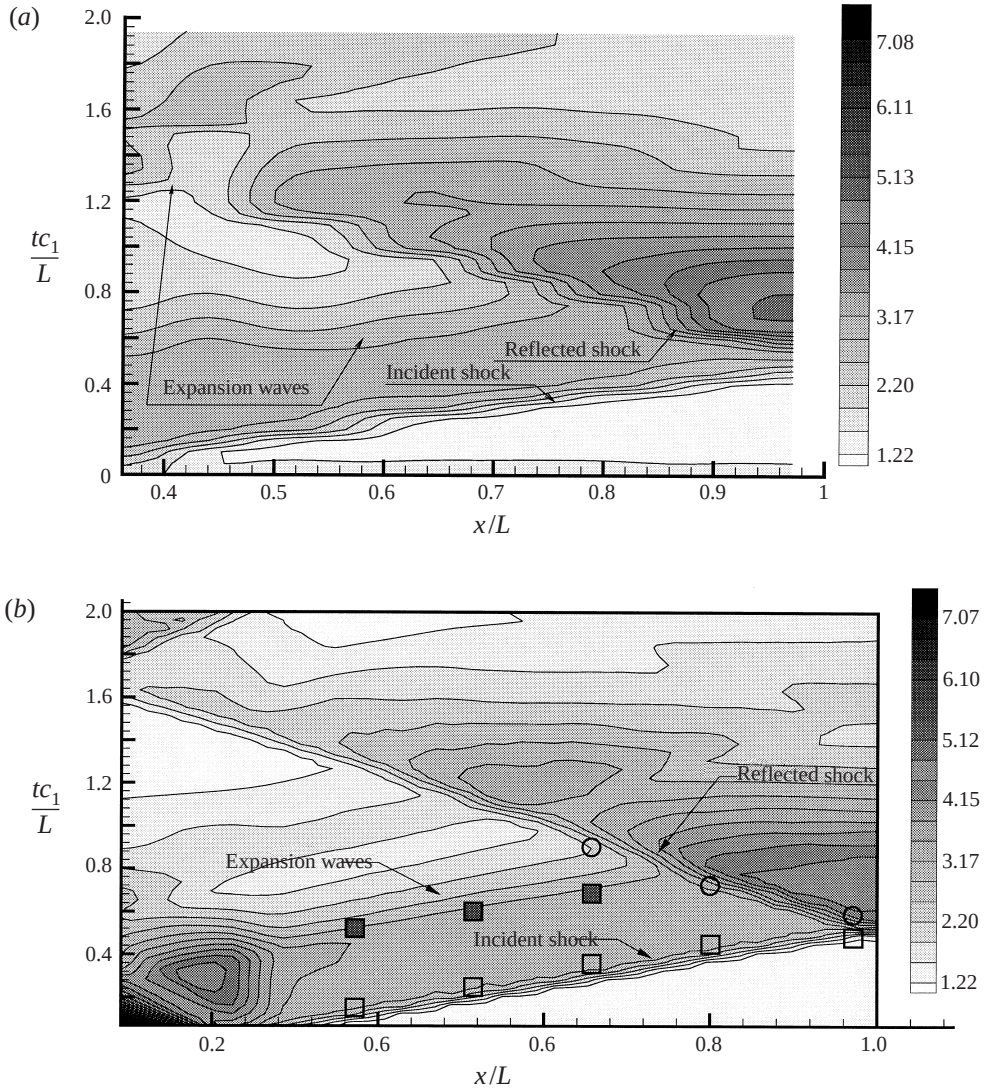

FIGURE 3. x–t diagram of static pressure: (a) experimental data; (b) from numerical simulation (symbols indicate arrival of shock and expansion wave fronts of the corresponding experimental data).

has to be excluded in our consideration of useful data. Thus the effective origin of the useful data is shifted after the passage of the incident shock by time of at least $t_0 = x/\overline{U_1}$, where x is the measurement location measured from the grid and $\overline{U_1}$ is the mean velocity. Values of this time shift are in the range of 1 ms to 3 ms.

Although all signals were visually inspected for the presence of undesirable reflected expansion or shock waves in the flow field, a more objective criterion was used to determine whether the data were seriously biased or contaminated by the arrival of these reflections: The mean time derivative $\overline{\partial Q}/\partial t$ was computed for the quantity Q where Q can be any one of $U, \rho U, T_0, p$, or vorticity. This derivative was computed by summing the central difference $\Delta Q_i = (Q_{i+1} - Q_{i-1})/2$ between two points and then

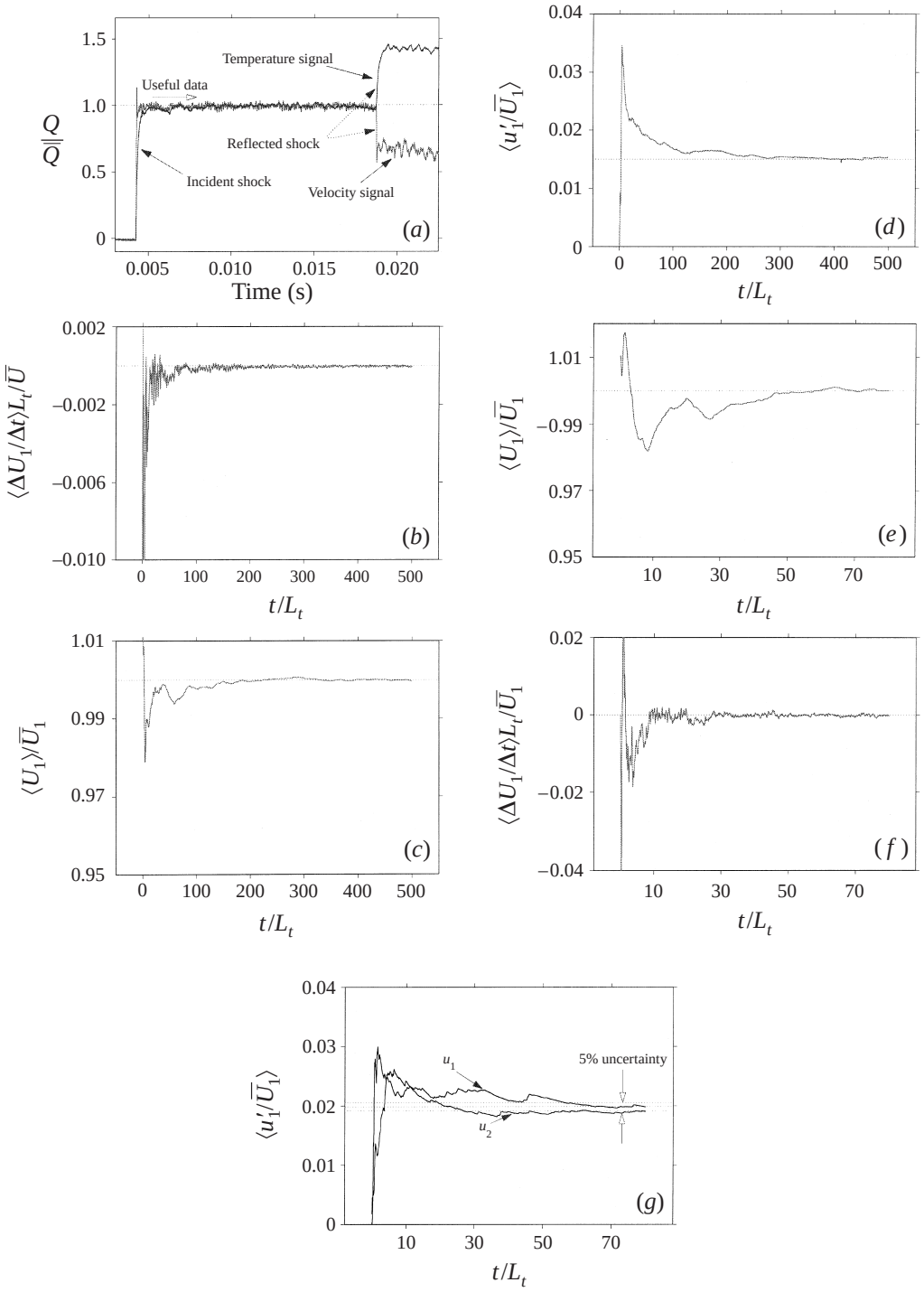

FIGURE 4. (*a*) Typical velocity and temperature signals. (*b*) Time derivative of mean velocity at a location close to the grid. (*c*) Mean velocity convergence at a location close to the grid. (*d*) Turbulence intensity convergence at a location close to the grid. (*e*) Mean velocity convergence at a location far away from the grid. (*f*) Time derivative of mean velocity at a location far away from the grid. (*g*) Turbulence intensity convergence at a location far away from the grid.

summing to compute the ensemble average:

$$\left\langle \frac{\overline{\partial Q}}{\partial t} \right\rangle = \frac{1}{N} \sum_{i=1}^{N} \frac{\Delta Q i}{\Delta t}$$

where Δt is the sampling interval and N is the number of samples under consideration. If this mean slope was close to zero within a small quantity e, the number of samples was reduced and the computation of statistical averages was repeated until the criterion $\overline{\partial Q}/\partial t < e$ was satisfied. In addition to checking for the presence of possible expansion or shock waves, the integral time scale L_t was used to determine the number of independent statistical realizations needed to ensure convergence. It is defined as

$$L_t = \int_0^\infty R_{uu}(\tau) \mathrm{d}\tau$$

where $R_{uu}(\tau)$ is the autocorrelation function defined as $R_{uu}(\tau) = \overline{u(t) \cdot u(t+\tau)}/\overline{u^2}$. To calculate the time scale, numerical integration of $R_{uu}(\tau)$ was carried out up to the first zero crossing point. This particular case shown in figure 4(*a*) indicated that the time scale was about 0.030 ms corresponding to 10 times the sampling interval.

Figure 4(*b*) shows values of the ensemble averages of the time-derivative of the mean velocity properly normalized, as a function of the number of large-eddy realizations, t/L_t. The data show that the mean velocity slope rapidly becomes small as the number of realizations increases. The major cause for the fluid acceleration in shock tube flows is the displacement effects caused by the growth of the wall boundary layer. The large diameter of the present shock tube, however, considerably suppresses this effect. As a result all signals in the present investigation were practically stationary.

Convergence of the statistical averages was also monitored closely. Figure 4(*c*), for instance, shows the rate of convergence of the mean velocity $\langle \overline{U_1} \rangle \overline{U_1}$ as a function of t/L_t, for the same data shown in figures 4(*a*) and 4(*b*). Mean velocity data seem to converge to within 1% very quickly, i.e. within 30 realizations. The rate of convergence of the turbulence intensity $\langle u_1'/\overline{U_1} \rangle$, which is shown in figure 4(*d*), is much slower than that of the mean velocity. About 200 independent realizations were needed for this case, while about 500 were available before the arrival of the reflected shock.

Far away from the grid, the number of statistically independent available realizations was reduced considerably for two reasons: first because the duration of the useful data was reduced by the earlier arrival of the reflected shock and the longer time shift of the origin t_o, and second because of the rapid increase of the integral time scales further downstream from the grid where the eddies amalgamate and form larger ones. Integral time scales can increase up to 3 times further downstream from the grid while the useful flow time duration can be reduced by 50% from the values closer to the grid. Thus the increase in L_t has a greater impact on the number of available realizations than the reduced time duration of useful data. Figure 4(*e*) shows the rate of convergence of mean velocity $\langle \overline{U_1} \rangle$ in a case where only 80 realizations were available. Convergence to within 1% is obtained with 15 realizations. The time derivative of mean velocity $\langle \Delta \overline{U_1}/\Delta t \rangle L_t/\overline{U_1}$ has also been computed and it reaches values 0.1% almost within 15 realizations.

Figure 4(*g*) shows the rate of convergence the two r.m.s. values $\langle u_1'/\overline{U_1} \rangle$ and $\langle u_2'/\overline{U_1} \rangle$. Convergence is achieved within 65 large eddy realizations while the difference between the two r.m.s. values is less than 2.5%, which is indicative of good isotropic conditions in the flow.

Information from statistics indicates that reliable statistical averages can be obtained from 80 independent samples. For instance, 60 samples are enough to capture 99% of the standard deviation obtained from unlimited samples. The need to use additional realizations from other experiments under the same conditions in cases like the previous one was considered in detail in relation with the repeatability of the measurements. Tests show that the repeatability of statistical averages obtained from different experiments was within 25% of the uncertainties involved. It was found that if this value is used to satisfy the convergence criteria, convergence could be obtained within one experimental realization only. In that respect the statistical averages presented here have been obtained by considering the data from one experiment only. It is of interest to address the future values of what is called tolerance limits (Wilks 1962) i.e. the lowest and highest values which define the range. Based on values obtained in this investigation and with a confidence level of 99%, the probability that all future values will be within the present limits is between 95% and 99%.

4. Flow quality

An extensive programme has been undertaken to assess the quality of the grid flow established in the shock tube. This was accomplished by measuring the flow uniformity and homogeneity in the working section on planes normal to the flow and in the longitudinal direction.

Two rakes of hot-wire probes were designed and used to measure velocity and temperature simultaneously at five or six locations in the radial direction at a given cross-section of the working section. Specially designed probes with high-frequency-response pressure transducers were also used as Pitot tubes to measure the flow Mach number at various locations in the flow field. These Mach number measurements were compared to those obtained from hot wires. In addition, wall pressure transducers located circumferentially at several positions around the same cross-section were used to monitor the flow and the passage of shock or expansion waves.

Figure 5(*a*) shows time-dependent velocity traces obtained in the flow with the 3×3 grid at $M_{flow} = 0.321$ at several radial locations spanning the whole diameter of the shock tube at $x/M = 50$. The signals are non-dimensionalized by their average value and they are displaced in the y-direction so that the arrival of incident and reflected shock waves, as well as the corresponding velocity behind them, can be easily observed. The flow immediately behind the incident shock, which has not passed through the grid, is also evident in these signals. The major feature of this flow region is its smaller velocity fluctuations compared to the fluctuations of the grid turbulence flow which arrives at roughly $t = 0.0095$ s. These signals demonstrate that the shock wave arrives at all sensor locations at the same time and therefore they provide an indication that the shock is planar. They also demonstrate that the grid flow remains stationary with their mean velocity traces very close to each other suggesting a high degree of flow uniformity. As the M_{flow} increases, the duration of useful data increases because the duration of flow which has not passed through the grid is reduced proportionally to U^{-1} while the speed of the reflected shock is not affected substantially. This is shown in figure 5(*b*) where the signals, obtained at $M_{flow} = 0.564$, are plotted. The useful grid flow velocity appears to be about 10% less than the velocity of the flow which has not passed through the grid. This is a result of the upstream travelling reflected shock which was generated during the impact of the incident shock on the grid. This weak disturbance reduces the flow velocity and increases the turbulent fluctuations of the flow approaching the grid by a very small

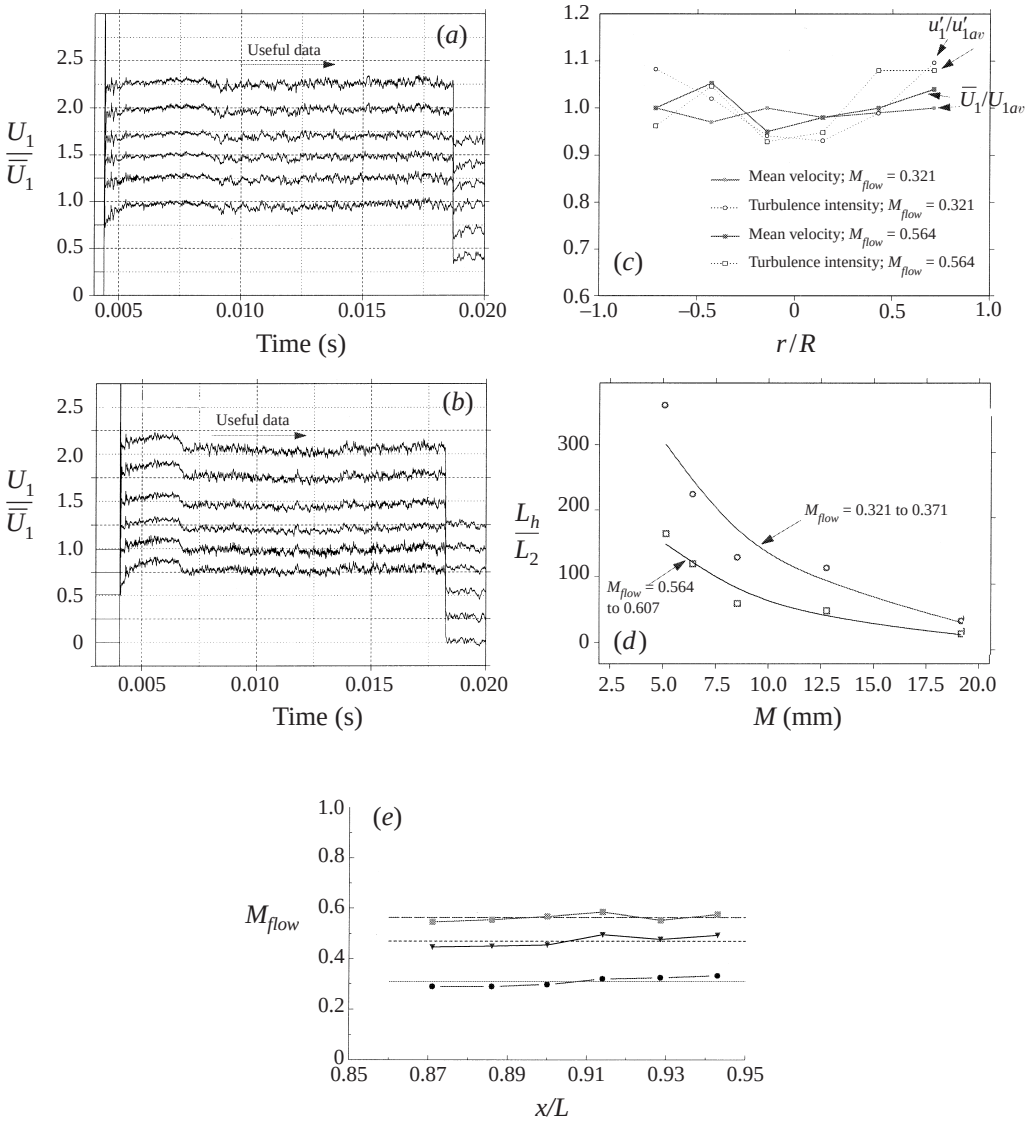

FIGURE 5. (*a*, *b*) Typical velocity traces at $M_{flow} = 0.321$ and 0.564; 3×3, $M = 8.5$ mm. (*c*) Radial distribution of mean velocity and turbulence intensity for the 3×3 grid flow at $M_{flow} = 0.321$ and 0.564. (*d*) Flow inhomogeneity as a function of grid/mesh size. (*e*) Mean flow Mach number along the working section. 3×3 grid, $M = 8.5$ mm.

amount. The present work has shown that the flow downstream of the grid is nearly homogeneous and isotropic despite this weak interaction.

Figure 5(*c*) shows the distribution of the mean velocity $\overline{U_1}$ and the turbulence intensity $u_1'/\overline{U_1}$ normalized by their average value $U_{1,av}$ and $u_{1,av}'$ respectively, at all six locations. This is a typical example of flow uniformity for the case of the 3×3 grid with mesh size $M = 8.5$ mm obtained at two different Mach numbers at a distance $x/M = 50$ from the grid. The standard deviation of all six values of mean velocity is no more than 1% from $U_{1,av}$ while the standard deviation of the values of turbulence

intensity is about 2% of average $u'_{1,av}$. The data in figure 5(*c*) suggest a high degree of uniformity of mean velocity and turbulence intensity in the radial direction. Similar levels of uniformity of mean velocity, mean temperature and statistical moments of their fluctuations have been observed through at least 85% of the area of any cross-section.

In general, the degree of inhomogeneity could be better expressed in terms of a scale of inhomogeneity defined as $L_h = \overline{u_i^2}/\partial\overline{u_i^2}/\partial x_2$ which should be compared with the size of the energy-containing eddies L_2 in the x_2-direction. L_2 is typically a fraction of the mesh size M and it can be approximated by $L_2 \approx M$. The scale L_h should be several times larger than L_2 for the effects of flow inhomogeneity to be ignored. Figure 5(*d*) shows the values of the ratio L_h/L_2 for various grid mesh sizes M for one low and one high M_{flow}. The higher the ratio the better the flow homogeneity. The data show that the homogeneity improves with decreasing mesh size M, i.e. finer grids have better flow homogeneity. The present data also show that mean flow Mach number effects tend to decrease slightly the flow homogeneity. Nevertheless even in the case of flows with coarse grids ($M = 19$ mm) $L_h/L_2 > 28$, a value which is considered adequate to assure that inhomogeneity in the present flows has minimal effect in the evolution of turbulence.

The mean flow Mach number data at various locations along the working section are also documented in figure 5(*e*) for three different flow fields. Values of M_{flow} have been plotted against distance from the grid normalized by the length of the shock tube L. It can be seen that the mean Mach number remained constant within 2.6% in the case of the highest M_{flow} and within about 4% for the lowest M_{flow}.

In conclusion, it appears that the quality of the flow established in the shock tube, in terms of uniformity of statistical averages, is very good. Thus the degree of near homogeneity of the flow field, defined as invariance to translation, has been achieved reasonably well.

5. The vorticity probe

A new multi hot-wire probe has been developed which is capable of measuring velocity-gradient-related quantities in non-isothermal flows or in compressible flows. The present probe has been built using the experience gained with vorticity measurements in incompressible flows (see Honkan & Andreopoulos 1997) by a probe with nine wires, and with velocity measurements in compressible flows by single- and cross-wire probes (see Briassulis *et al.* 1995). The present vorticity probe, which consists of 12 wires is a modification of the original design by Honkan & Andreopoulos (1997, hereafter referred as HA). The three additional wires were operated in the so-called constant-current mode and used to measure time-dependent temperature.

Since the probe essentially consists of a set of three modules, it is necessary to provide several key features of the individual hot-wire modules. Each module contains three hot wires operated in the constant-temperature mode (CTM) and one cold-wire sensor operated in the constant-current mode (CCM). Each wire of the triple wire sub-module is mutually orthogonal to the other two, thus oriented at 54.7° to the probe axis. Each of the 5 μm diameter tungsten sensors is welded on two individual prongs which have been tapered at the tips. Each sensor is operated independently since no common prongs are used. Each of the 2.5 μm diameter cold wires was located on the outer part of the sub-module.

The hot-wire output voltage E_i of the ith sensor is related to the effective cooling

velocity, $U_{i,eff}$ through the well-known King's law:

$$\frac{E_i^2}{T_w - T_0} = A_i \left[\frac{T_0}{T_r}\right]^a + B_i \left[\frac{T_0}{T_r}\right]^b (\rho U_{i,eff})^n, \tag{5.1}$$

where T_w is the hot-wire temperature, T_0 is the total temperature of the flow and T_r is a reference temperature, the ambient temperature in the present case. The values of the exponents a and b were taken as suggested by Kovasznay (1950) $a = b = 0.768$. The effective velocity is related to $U_{i,N}$, $U_{i,T}$ and $U_{i,B}$, the normal, tangential and binormal components of the velocity vector in reference to the ith sensor respectively, by

$$U_{i,eff}^2 = U_{i,N}^2 + k^2 U_{i,T}^2 + h^2 U_{i,B}^2, \tag{5.2}$$

where k and h are coefficients which, for a given probe, depend on the yaw and pitch angle of the velocity vector. Details of the techniques associated with the use of triple-wire probes can be found in Andreopoulos (1983*a*) while estimates of errors related to probe geometry and turbulence intensity are described by Andreopoulos (1983*b*).

The probe, shown schematically in figure 6 consists of a set of three individual modules with four wire sensors each, put together so that the probe remains geometrically axisymmetric.

In selecting the dimensions of the vorticity probe several conflicting considerations have to be taken into account. The individual wire length, the size of the individual sub-module and the size of the overall probe should be as a small as possible so that small scales can be resolved adequately since it is known that most of the contributions to vorticity come from small scales of turbulence. However, small wire spacing can lead to thermal interference and cross-talk between the wires. This was of particular concern in the present case because of the high overheat ratio used in the experiments. Yaw and pitch tests of the probe were carried out in order to identify any thermal effects on wires located in the heated wake of a neighbouring wire located upstream. These tests indicated no thermal interference among the wires. The reason for this behaviour is that the spreading rate of the thermal wakes is reduced in high Reynolds number flows.

The requirement to reduce the probe size had to be counterbalanced with the requirement that the spacing between the sub-modules and the individual wires should be finite so that the velocity gradients, which were used to compute vorticity and strain rates, do not disappear.

The present probe design differs from that used in HA in the following aspects:

(i) It consists of 12 wires with three of them measuring total temperature. The capability to measure time-dependent total temperature makes the probe suitable for measurements in non-isothermal flows while, at the same time, the availability of temperature information allows decoupling of the velocity and density.

(ii) The overheat ratio in which the hot wires were operated was close to 130%. This high overheat ratio was required in order to maintain the heat transfer rate from the wire to the driven flow at substantial levels.

(iii) The diameter of the velocity sensing wires was 5 μm. This reduced the length-to-diameter ratio of each wire to about 200 which is large enough to suppress end heat conduction effects. Attempts to work with 2.5 μm wires were unsuccessful because of substantial strain-gauging effects and wire breakage.

Velocity calibrations were carried out inside the shock tube by firing the tube at various pressures corresponding to Mach numbers anticipated to be found in the

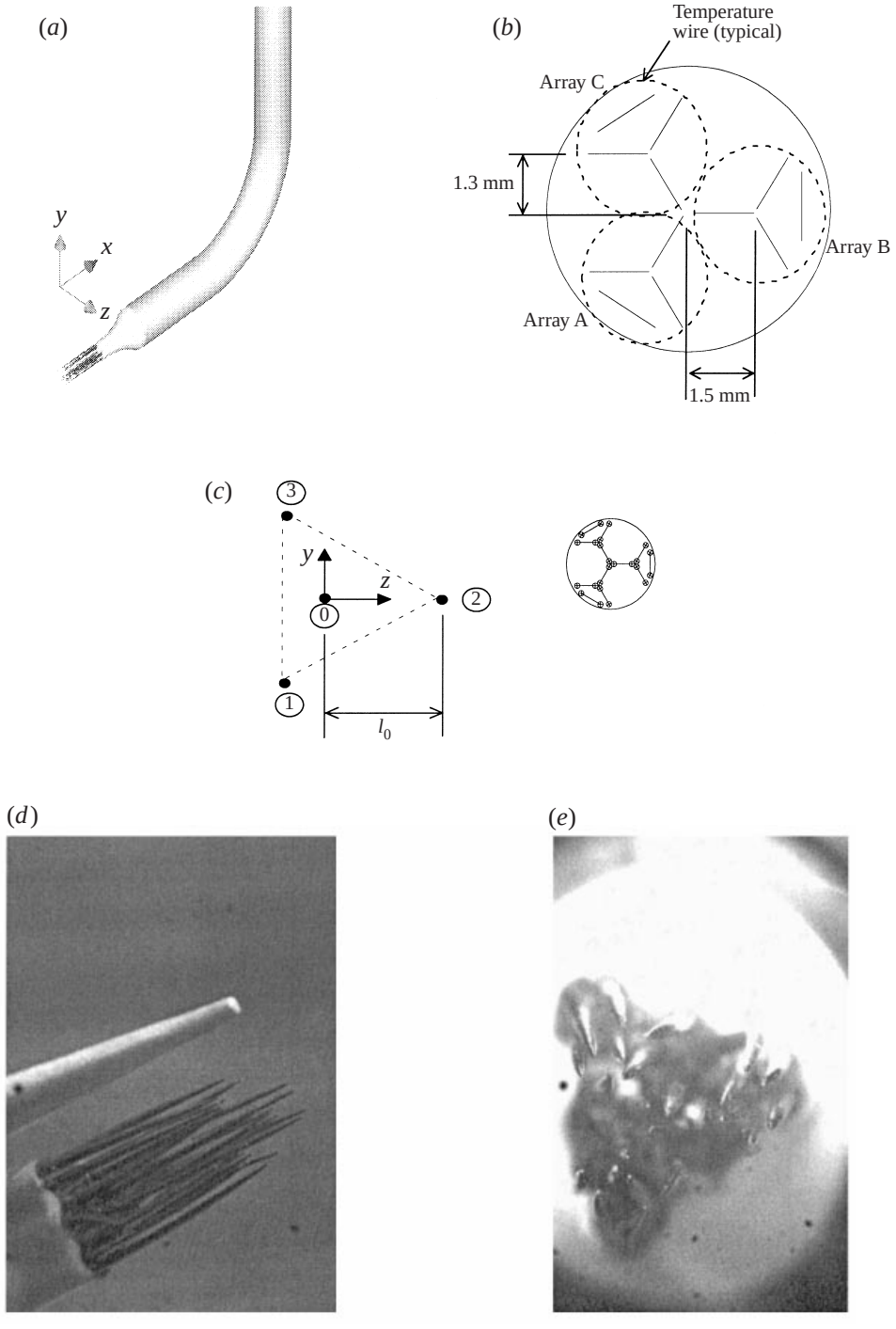

FIGURE 6 (*a–e*). For caption see facing page.

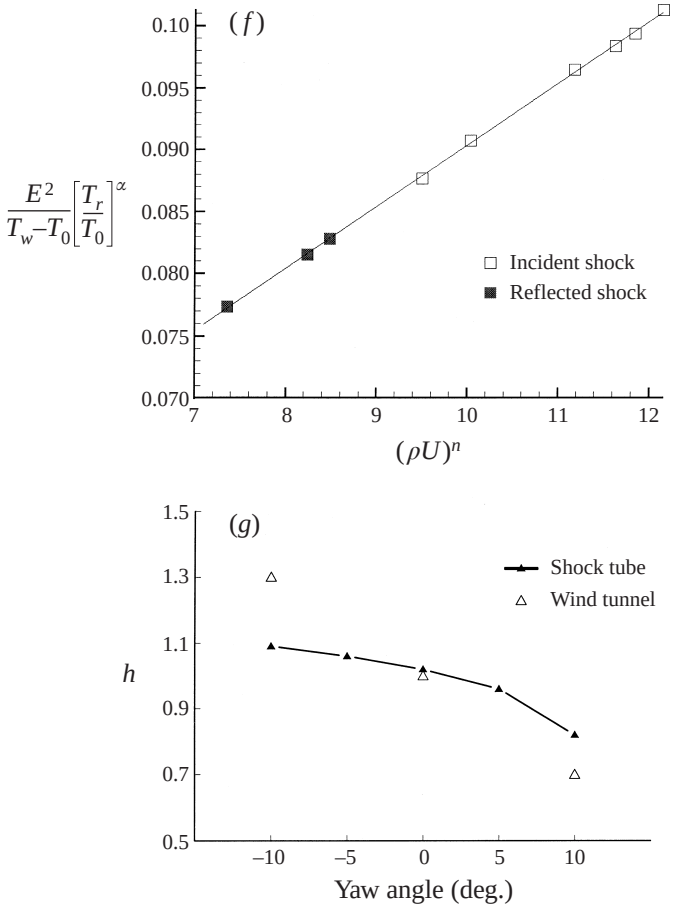

FIGURE 6. Vorticity probe: (*a*) perspective view, (*b*) probe sensor geometry, (*c*) layout of probe centroids, (*d*) photograph showing size comparison with toothpick, (*e*) close up view directly into probe. (*f*) Typical hot-wire calibration. (*g*) Yaw response in shock tube and low-speed wind tunnel.

flows under investigation. Figure 6(*f*) shows a typical velocity (mass flux) calibration carried out in this shock tube. Two sets of values of E_i, total temperature T_0, pressure p, and velocity U were obtained from each run: one set upstream and one downstream of the reflected shock. The data downstream of the reflected shock front correspond to a flow field with lower velocity and higher density than the flow field upstream. The fact that both sets of data collapse on the same curve gives a strong indication that the technique is valid. It should be noted that this technique was also applied successfully to a flow with a strong turbulence–shock interaction carried out in a smaller diameter shock tube (see Honkan & Andreopoulos 1992).

Yaw and pitch calibration of the probe was also carried out *in-situ*. These data help to extend a complete and detailed map of the yaw and pitch response of the probe obtained in a low-speed wind tunnel to the subsonic range of flow velocities needed in the present investigation. Values of the coefficient h of equation (5.2) obtained in the shock tube over a range of yaw angle from -10° to $+10^\circ$ are shown in figure 6(*g*). The data indicate that there is no appreciable change of h with yaw or pitch angle in the Mach number range of flows considered here. This suggests that there is no need to use iterations in the data processing to account for any dependence of h

on yaw or pitch angle as has been demonstrated in the work of Andreopoulos (1981). Calibration in yaw was not extended beyond the range of $\pm 10^{\circ}$ because the expected range of the yaw or pitch angle of the velocity vector is in the same range since turbulence intensity never exceeds 7%. It is also interesting to see that the values of h obtained in the shock tube do not vary as much as the values obtained in the wind tunnel and therefore are less sensitive to changes in flow direction.

The digitized signals were processed off-line. The cold-wire signals were first converted to total temperature which together with the hot-wire signals were used to obtain instantaneous three-dimensional mass fluxes at three neighbouring locations within the probe. Numerical techniques and algorithms used in the computations of velocity gradients were very similar to those described by HA. The only difference is that in the present case mass fluxes and their gradients were computed at the centroid of each module instead of velocities and velocity gradients.

Mass fluxes were further separated into density and velocity by using the method adopted by Briassulis *et al.* (1996). Decoupling density from mass fluxes assumes that static pressure fluctuations are small. This is the 'weak' version of the original 'strong Reynolds analogy' hypothesis of Morkovin (1956). The original hypothesis is based on the assumption that pressure *and* total temperature fluctuations are very small. In the present work, total temperature was measured directly and therefore no corresponding assumptions were needed. The pressure, however, was measured at the wall and not at the location of the hot-wire measurement. The mean value of this pressure signal was used to separate the density and velocity signals since no mean pressure variation has been detected across a given section of the flow. The procedure involves an expression for mass flux, m_i, in terms of total temperature, T_0, and pressure, p, at the centroid of each module:

$$m_i = \rho U_i = \frac{pU_i}{RT} = \frac{pU_i}{R\left[T_0 - U_k U_k/(2c_p)\right]}. \tag{5.3}$$

U_i is the instantaneous velocity component, $i = 1, 2$ or 3 and $U_k U_k = U_1^2 + U_2^2 + U_3^2$. The velocity can be decomposed into $U_i = \overline{U_i} + u_i$.

An iterative scheme was used to decouple density and velocity. During the first iteration it was assumed that the quantity $(u_2^2+u_3^2)/2c_p$, where u_2 and u_3 are the velocity components in the spanwise and normal directions respectively, is substantially smaller that the quantity $T_0 - U_1^2/2c_p$. Then relation (5.3) can be rearranged to obtain a quadratic equation for U_i,

$$\frac{Rm_i}{2c_p} U_i^2 + pU_i - m_i R T_0 = 0. \tag{5.4}$$

For each digitized point, T_0 and m_i were available instantaneously at the centroid of each module while pressure was measured at the wall. If the thin shear layer approximation is invoked then the pressure at the centroid of the module which appears in (5.4) can be substituted by the mean pressure at the wall. This assumption is justified because pressure fluctuations are extremely small and therefore their impact on velocity fluctuations is minimal.

The discriminant of (5.4), $\Delta = p^2 + 2m_i^2 R^2 T_0/c_p$, is always positive and therefore there are two real roots. The product of the two roots, as expressed by the ratio of the last term of the left-hand side of equation (5.4) to the coefficient of the first term, is always negative. Therefore one root is positive and one negative. The negative root is unrealistic and only the positive root was accepted. The longitudinal velocity component U_1 was computed first while the other two components were obtained

from the mass flux ratios as $u_2 = m_2/m_1 U_1$ and $u_3 = m_3/m_1 U_1$. These values provided the first estimate of the velocity components which were used to obtained a better estimate of $U_k^2/2c_p$ in (5.3), which subsequently was used to improve the estimate of the velocity components. This iterative scheme required no more than two iterations for convergence.

In summary, it should be emphasized that the major contribution of the present hot-wire techniques is the addition of temperature wires to obtain instantaneous information on total temperature. This allowed decoupling of all partial sensitivities of the probe from each other. Thus, $S_\rho = \partial E/\partial\rho \neq S_{\rho u} = \partial E/\partial \rho u \neq S_u = \partial E/\partial u$.

6. Uncertainty estimates

The pressure and total temperature measurements depend directly, through obtained calibration constants, on the raw voltage data from the individual sensors. These probes, because of their linear response, produced two calibration constants, sensitivity and d.c. offset. Therefore estimates of the uncertainty in the measurements of pressure and total temperature acquired through a 12-bit A/D converter depended mostly on the bit resolution and the residual errors from the calibration constants. Uncertainties in the range of less than 0.5% in pressure and about 2% in total temperature were found for typical measurements of these two quantities.

The mass flux measurements were tied to significantly more-complex relations which depended on the individual and relative geometry of different sensors. Mass flux was found to depend on the following variables: captured raw voltage E_i, reference temperature T_r, total temperature T_0, wire temperature T_w, calibration constants and yaw or pitch coefficients. Estimates of the uncertainty in the measurements of mass flux after considering all the above contributing factors was found to be 1–3%. Uncertainty values for the velocity were estimated to be 1.5–3.5%. In obtaining all these estimates the square root of the squares of all partial uncertainties involved was assumed to model the error propagation in the final results. MATHCAD was used to calculate the partial uncertainties.

Following the work of HA estimates of the uncertainties associated with the measurements of velocity gradients were also obtained by considering the propagation of the uncertainties in the measurement of each quantity involved in the process. A typical velocity gradient is measured through the following approximation:

$$\frac{\partial U_i}{\partial x_j} \approx \frac{U_2 - U_1}{l_p} = F$$

where U_2 and U_1 are the velocities at two nearby locations and l_p is the distance between these locations. If the uncertainties in the measurements of U_2 and U_1 are the same, $\Delta U_1 = \Delta U_2 = \Delta U$, and l_p is determined accurately, then the relative uncertainty $\Delta F/F$ will be given by

$$\frac{\Delta F}{F} = \left(2\left(\frac{\Delta U}{U_2 - U_1}\right)^2\right)^{1/2}.$$

A typical ΔU is 2% of mean U which corresponds to about $2\,\mathrm{m\,s^{-1}}$ while typical velocity differences $U_2 - U_1$ can be up to six times the r.m.s. value, u'. If a typical value of this velocity difference is assumed of about $30\,\mathrm{m\,s^{-1}}$ in the near field of the grid and $15\,\mathrm{m\,s^{-1}}$ further downstream, then the uncertainty $\Delta F/F$ appears to be 10% in the near field and 14% in the far field.

Lower uncertainty estimates have been found if the relation

$$\frac{\partial U_i}{\partial x_j} \approx \frac{u'}{\lambda} = F$$

is used for their computation. In this case the relative error is

$$\frac{\Delta F}{F} = \left(\left(\frac{\Delta u'}{(u')} \right)^2 + \left(\frac{\Delta \lambda}{\lambda} \right)^2 \right)^{1/2}.$$

For a typical relative error in u' of 5% and 10% in λ the relative error appears to be about 11%. It should be note that the relative error $\Delta F/F$ increases as the distance away from the grid increases because the absolute value of F decreases.

Finally the finite number of statistically independent events considered in the analysis of data obtained at low M_{flow} and at large distances from the grid may introduce an uncertainty in the statistical results. As mentioned before, the arrival of the reflected shock affects first the measurement locations closer to the porous endwall which are the furthest from the grid, by reducing the duration of useful data. The onset of the useful data duration is also delayed by the arrival of air mass which has not gone through the grid. Computations of the integral time scale L_t from auto-correlation functions $R_{uu}(\tau)$ indicated that the number of independent samples in these cases was about $N \simeq 100$. Bendat & Piersol (2000) indicate that the relative error in the estimate of the variance of the velocity fluctuations is $2/N$ which for this specific case at large x/M is 2%. It should be noted that N depends on R_{uu} which can be extended to large values if low-frequency disturbances are present in the flow fields which are not related to the actual flow turbulence. If a high-pass filtering at 200–400 Hz is applied to the present data L_t is reduced substantially and N increases by a factor of 2. No such filtering has been applied to the present data other than what is imposed by the record length. For 10 ms record length the lowest frequency of interest is about 100 Hz.

Further direct evidence of the adequacy of statistical samples can be provided by the rate of convergence of the various statistical quantities which are computed in the present data analysis. As was shown earlier, estimates of the convergence uncertainties observed in the present analysis indicate an error of less than 2%. This error is substantially less at higher Mach numbers and closer to the grid locations.

7. Qualification tests

Assessment of the performance of the newly designed probe was accomplished by carrying out measurements in the present compressible grid flow of the shock tube and in a two-dimensional turbulent boundary layer configured in a low-speed wind tunnel. In the first case, statistical averages of conventional quantities obtained with this probe were compared directly with those obtained with single- or cross-wire probes. Statistical quantities including velocity gradients, like the dissipation rate of turbulent kinetic energy, were also compared whenever it was possible. These comparisons, which are described later in the section on results, indicated that turbulent normal stresses are within 8% of each other while the dissipation rate obtained with the vorticity probe is about 5% to 15% higher than those obtained from the decay rate of turbulent kinetic energy. This is the first evidence that the probe performs well in the present compressible flow.

U_e (m s^{-1})	Boundary layer thickness δ (mm)	Momentum thickness θ (mm)	Re_θ	Friction velocity u_τ (m s^{-1})
9.1	97	9.21	5300	0.315

TABLE 2. Incompressible boundary layer flow parameters.

Dimension	Resolution in Kolmogorov scales
Wire length	$\eta_w = 5$
Separation of sub-modules in normal direction	$\eta_{\Delta x1} = 6$
Separation of sub-modules in spanwise direction	$\eta_{\Delta x2} = 8$

TABLE 3. Spatial resolution estimates in incompressible boundary layer experiment.

The probe was further evaluated by carrying out measurements of vorticity and turbulent stresses in the incompressible boundary layer flow where the data of HA were obtained. This allowed a direct comparison of the present data obtained at $Re_\theta = 5300$ with the data of HA obtained at $Re_\theta = 2800$.

The bulk flow parameters of the boundary layer experiments are given in table 2.

The estimates of the flow scale resolution expressed in Kolmogorov microscale (viscous scale) units are shown in table 3.

The performance characteristics of the present probe are demonstrated in figure 7 where the shear stress $-\rho\overline{u_1 u_2}$ across the boundary layer, normalized by the wall mean shear ρu_τ^2, is plotted against the distance from the wall normalized by the boundary layer thickness $\delta, x_2/\delta$. Among all the turbulent stresses, shear stress is the most challenging quantity to measure accurately. The reason is that it is sensitive to small changes in probe alignment and experimental conditions which can increase substantially the uncertainty of the measurements. The data presented in figure 7 are the averaged data obtained at the centroid of the probe. The present data are compared with the measurements of HA, the data of Balint, Wallace & Vukoslavcevic (1991) and the data of Klebanoff (1954) as well as with the direct numerical simulation results of Spalart (1988). The present data seem to agree well with previous data in the logarithmic and outer ($x_2/\delta > 0.05$) region of the boundary layer.

Figure 8 shows the distribution of the mean velocity gradient $\overline{(\partial U_1/\partial x_2)}$ across the boundary layer as measured at the centroid of the probe by time-averaging its instantaneous values. On figure 8 the mean velocity derivative in the logarithmic law region, $1/\kappa x_2^+$, where κ is von Kármán's constant, is also plotted for comparison. It appears that the measured mean velocity gradient data are in very good agreement with those obtained theoretically from the log-law. The present data are also in good agreement with those of HA (not shown here) which were obtained in the same facility at $Re_2 = 2790$ which is considerably lower than the present value.

A comparison of the r.m.s. of fluctuations of the three vorticity components across the boundary layer measured by the present probe with data obtained by other investigators is shown in figures 9(*a*), 9(*b*) and 9(*c*). These data are scaled with the boundary layer thickness δ and friction velocity u_τ. The values are compared with the DNS results of Spalart (1988) and the experimental results of HA, Balint *et al.* (1991) and Lemonis (1995), for the three vorticity components. Additionally the measurements of Klewicki (1989) are also indicated on the plots for the spanwise component.

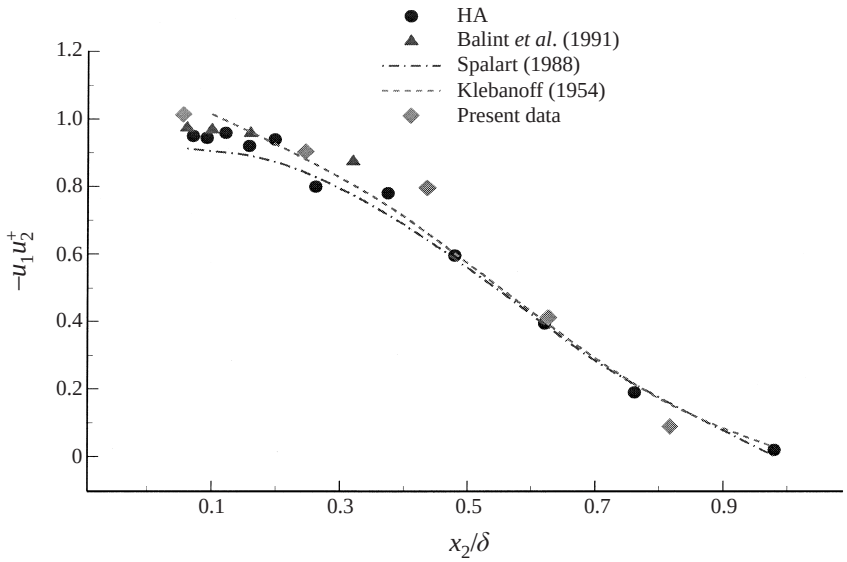

FIGURE 7. Normalized shear stress in boundary layer experiment and comparison with previous measurements.

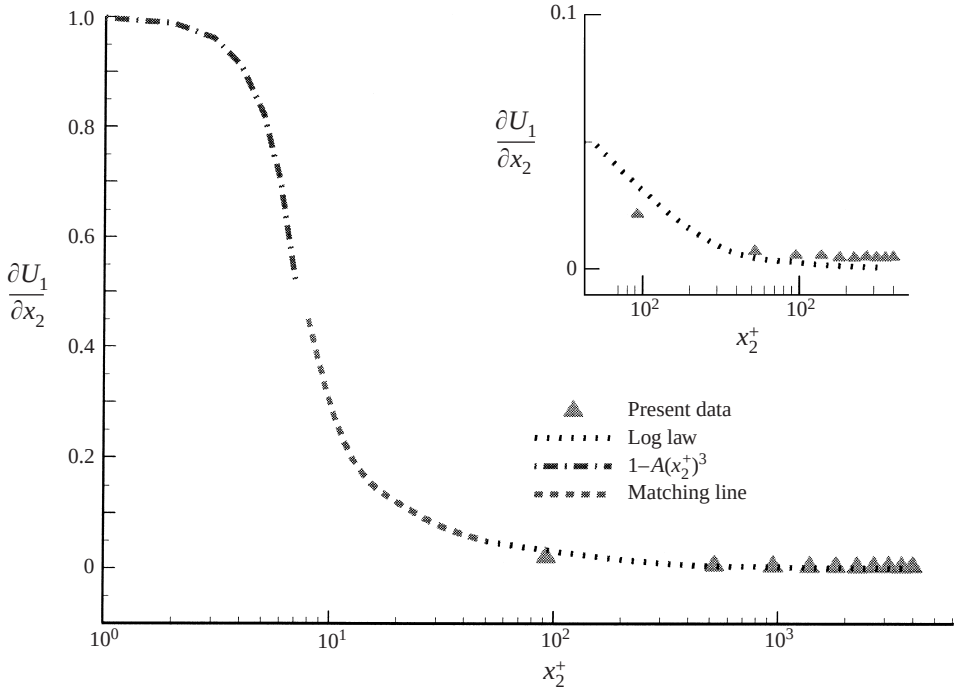

FIGURE 8. Mean velocity gradient across boundary layer.

The present data for ω_1 are very close to those HA and of Balint *et al.* (1991). These three experimental data sets, as a group, have values considerably greater than the DNS results of Spalart (1988).

The present values of the r.m.s. of the normal vorticity component ω_2 agree rather

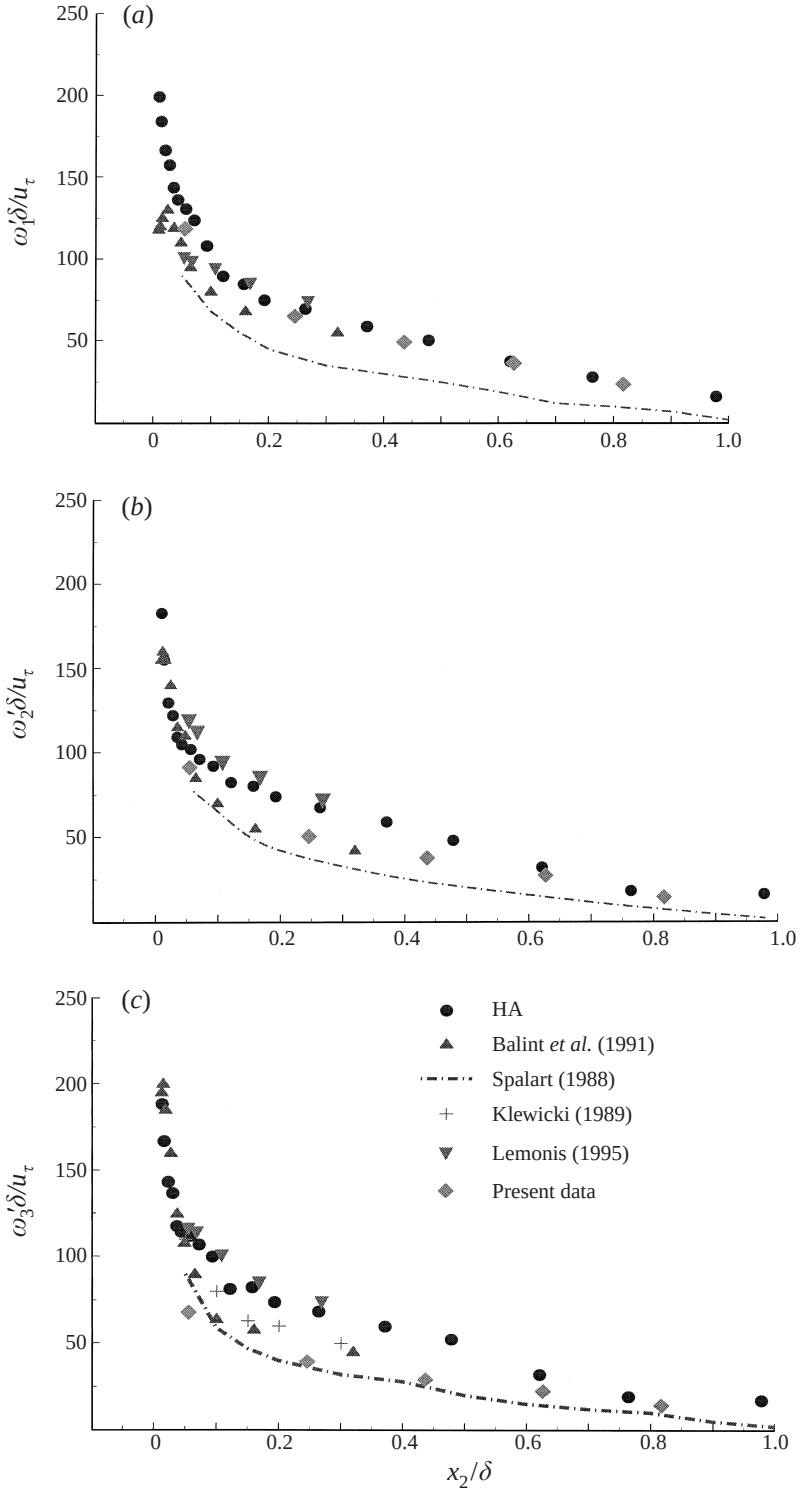

FIGURE 9. Root-mean-square of vorticity fluctuations normalized by u_τ and δ: (*a*) axial, (*b*) normal, and (*c*) spanwise.

well with the data of Balint *et al.* and they are substantially lower than those of HA in the outer part of the boundary layer $x_2/\delta > 0.1$ which agree with the measurements of Lemonis (1995). The fluctuations of the dominant component of vorticity ω_3 as measured by the present probe compare well with the data of Balint *et al.*

It should be noted that there is a substantial difference in Re_θ among all data sets under consideration. The present data and those of Lemonis which correspond to $Re_\theta = 5300$ and $Re_\theta = 6500$ respectively represent the higher Reynolds number data for comparison while the DNS data of Spalart with $Re_\theta = 1410$ represent the lower Re_θ data. Several of the differences among the data sets can be attributed to Re_θ effects although it is not known how increasing Re_θ will affect vorticity fluctuations and their averages. It may be expected, for instance, that the r.m.s. of vorticity fluctuations will decrease in the outer layer of the boundary layer as Re_θ increases. Evidence to support this argument can be found in the r.m.s. values of wall vorticity flux shown in HA, which have one of the strongest Reynolds number dependence ever observed of any quantity involving vorticity: for a factor of 3 increase of Re_θ a decrease by a factor 5 in the r.m.s. of wall vorticity flux has been observed. This evidence points to a tendency in which the r.m.s. of ω_1, ω_2 and ω_3 are expected to decrease with increasing Re_θ. In fact the present data, if one limits the comparison to the HA data only, clearly support this conclusion. This comparison is more meaningful because both data sets were obtained in the same wind tunnel facility by almost identical techniques and procedures. Thus, it is plausible to expect that the present data should be lower than the data of HA because of Re_θ effects.

The conclusion of the qualification tests of the newly designed vorticity probe is that it performed very well in the measurements of mean and fluctuating vorticity in turbulent boundary layers as well as in the measurements of shear and normal stresses. Comparison of the data with previous measurements was very satisfactory. This provided considerable confidence in the use of the probe in weakly compressible, grid-generated turbulence.

8. Isotropic decay relations

Three characteristic regions can be found in the flow behind a grid. First is the developing region close to the grid where rod wakes are merging and production of turbulent kinetic energy takes place. This region is followed by one where the flow is nearly homogeneous and isotropic but where appreciable energy transfer from one wavenumber to another occurs. This region is best described by the power-law decay of velocity fluctuations

$$\frac{\overline{u^2}}{\overline{U^2}} = A\left[\frac{x}{M} - \left(\frac{x}{M}\right)_0\right]^{-n}, \tag{8.1}$$

where A is the decay coefficient, $(x/M)_0$ is the virtual origin, and n is the decay exponent. The third or final region of decay is farthest downstream of the grid and is dominated by strong viscous effects acting directly on the large energy-containing eddies.

Decay laws for compressible homogeneous and isotropic turbulence have yet to be established. However, relation (8.1) can be a starting point to consider possible compressibility effects. The decay coefficient A, for instance, is strongly related to the drag coefficient of the rods of the grid C_d (see Batchelor 1953) which becomes Mach-number dependent in compressible flows. Thus it is reasonable to assume that A as well as the exponent n and the virtual origin $(x/M)_0$ are also Mach-number dependent.

The turbulent or fluctuation Mach number $M_t = q_t/\bar{c}$ with $q_t = (\overline{u_i u_i})^{1/2}$, seems to be the most appropriate parameter describing compressible turbulence. It is hypothesized here, and it will proven experimentally, that Mach number fluctuations in weakly compressible turbulence decay according to the power law

$$M_t^2 = B\left[\frac{x}{M} - \left(\frac{x}{M}\right)_0\right]^{-n}, \tag{8.2}$$

where $B = 3AM_{flow}^2$ and B, $(x/M)_0$ and n depend on the grid size and/or solidity, mesh Reynolds number (Re_M) and the mean flow Mach number M_{flow}, which simply comprise the initial conditions.

9. Dissipation rate of turbulent kinetic energy

The transport equation for the instantaneous kinetic energy $\frac{1}{2}U_iU_i$ in compressible flows is

$$\rho\frac{\mathrm{D}(\frac{1}{2}U_iU_i)}{\mathrm{D}t} = -U_i\frac{\partial p}{\partial x_i} + U_i\frac{\partial \tau_{ij}}{\partial x_j}, \tag{9.1}$$

where τ_{ij} is the stress tensor, $\tau_{ij} = 2\mu S_{ij} + \lambda\delta_{ij}S_{kk}$, and where λ is the second coefficient of viscosity which is related to the bulk viscosity μ_b through $\lambda = \mu_b - (2/3)\mu$.

The above equation can be manipulated to yield

$$\rho\frac{\mathrm{D}(\frac{1}{2}U_iU_i)}{\mathrm{D}t} = \frac{\partial(-pU_j + \tau_{ij}U_i)}{\partial x_j} + pS_{kk} - \tau_{ij}S_{ij}, \tag{9.2}$$

where the last term on the right hand side contains the dissipation rate of kinetic energy, E, converted into thermal/internal energy. The term pS_{kk} represents the work done by pressure forces during compression or expansion of the flow. Both terms, the dissipation rate $E = \tau_{ij}S_{ij}$ and the pressure work term, also appear with opposite sign in the transport equation for internal energy. While the dissipation rate is always positive at any given point in space and time, the pressure–dilatation term can, in principle, be positive or negative.

The dissipation rate is given by

$$E = \tau_{ij}\frac{\partial U_i}{\partial x_j} = \tau_{ij}S_{ij} = 2\mu S_{ij}S_{ij} + \lambda\frac{\partial U_k}{\partial x_k}\delta_{ij}\frac{\partial U_i}{\partial x_j}. \tag{9.3}$$

After invoking Stokes hypothesis which suggests that the bulk viscosity is negligible, $\mu_b \approx 0$, the above equation becomes

$$E = 2\mu S_{ij}S_{ij} - \tfrac{2}{3}\mu\frac{\partial U_k}{\partial x_k}\frac{\partial U_m}{\partial x_m}. \tag{9.4}$$

The second term in the right-hand side of (9.4) represents the additional contribution of compressibility to the dissipation rate of kinetic energy. This term disappears in the cases of incompressible flows.

Since $(\partial U_k/\partial x_k)\partial U_m/\partial x_m = (\partial U_k/\partial x_k)^2$ this term is always positive; the negative sign may erroneously suggest that compressibility reduces dissipation. This is incorrect because the term $S_{ij}S_{ij}$ also contains contributions from dilatation effects which can be revealed if one considers

$$S_{ij}S_{ij} = \tfrac{1}{2}\Omega_k\Omega_k + \frac{\partial U_i}{\partial x_j}\frac{\partial U_j}{\partial x_i}, \tag{9.5}$$

where $\Omega_k\Omega_k$ is the enstrophy rate. The second term in the right-hand side represents

the inhomogeneous contribution in the case of incompressible flows. In the case of compressible flows, terms related to dilatation can be extracted through

$$\left(\frac{\partial U_i}{\partial x_j}\frac{\partial U_j}{\partial x_i}\right) = \left(\frac{\partial U_k}{\partial x_k}\right)\left(\frac{\partial U_m}{\partial x_m}\right) + \left[\left(\frac{\partial U_i}{\partial x_j}\frac{\partial U_j}{\partial x_i}\right) - \left(\frac{\partial U_k}{\partial x_k}\right)\left(\frac{\partial U_m}{\partial x_m}\right)\right]. \tag{9.6}$$

Then, the dissipation rate becomes

$$E = \mu\Omega_k\Omega_k + \tfrac{4}{3}\mu\frac{\partial U_k}{\partial x_k}\frac{\partial U_m}{\partial x_m} + 2\mu\left[\frac{\partial U_i}{\partial x_j}\frac{\partial U_j}{\partial x_i} - \frac{\partial U_k}{\partial x_k}\frac{\partial U_m}{\partial x_m}\right]$$

or

$$E = \mu\Omega_k\Omega_k + \tfrac{4}{3}\mu S_{kk}^2 + 2\mu\left[\frac{\partial U_i}{\partial x_j}\frac{\partial U_j}{\partial x_i} - S_{kk}^2\right]. \tag{9.7}$$

The second term on the right-hand side describes the direct effects of compressibility, i.e. dilatation, on the dissipation rate. It is obviously zero in the case of incompressible flows.

The first two terms on the right-hand side of (9.7) are quadratic with positive coefficients and positive signs and they are, therefore, always positive. The last term on the right-hand side indicates the contributions to the dissipation rate by the purely non-homogeneous part of the flow. Its time-averaged contribution disappears in homogeneous flows like the present one. This term, in principle, can obtain negative values and thus it can reduce the dissipation rate. This does not violate the second thermodynamic law as long as the total dissipation remains positive at any point in space and time. It should be noted that the dissipation term appears as a source term in the transport equation for entropy. In the present context we will try to evaluate the contribution of the first two terms to the total dissipation as it has been computed from our measurements.

It has been customary in the past, (see for instance Zeman (1990)) to decompose E into a solenoidal part E_s, which is the traditional incompressible dissipation, and the dilatational part E_d. In this case

$$E = E_s + E_d \quad \text{with} \quad E_s = \mu\,\Omega_k\Omega_k + 2\mu\left[\frac{\partial U_i}{\partial x_j}\frac{\partial U_j}{\partial x_i} - S_{kk}^2\right] \quad \text{and} \quad E_d = \tfrac{4}{3}\mu S_{kk}^2.$$

Since all the mean velocity gradients are zero in the present homogenous flow the above can be transformed into

$$E = \mu\omega_k\omega_k + \tfrac{4}{3}\mu s_{kk}^2 + 2\mu\left[\frac{\partial u_i}{\partial x_j}\frac{\partial u_j}{\partial x_i} - s_{kk}^2\right] \tag{9.8}$$

where the lower-case letters represent the fluctuating part only.

It is also useful to consider the time-averaged turbulent kinetic energy transport equation. This is usually expressed in terms of the mass-weighted averages of Favre (1965). In the present case, velocity fluctuations were decoupled from mass fluxes and therefore the transport equation for turbulent energy $(1/2)\overline{u_i u_i}$ will be used. However, reference will be made to the mass-weighted averages when the order of magnitude of various terms appearing in the equation is considered.

If V is the specific volume defined as $V = 1/\rho$ then

$$\frac{1}{V}\frac{\mathrm{D}V}{\mathrm{D}t} = S_{kk}$$

and equation (9.1) can be transformed to yield the transport equation for $\frac{1}{2}u_i u_i$ after

considering that mean pressure and velocity gradients are zero in the present flow:

$$\bar{U}_k \frac{\partial \overline{(u_i u_i/2)}}{\partial x_k} = \overline{u_i u_i s_{kk}} + \overline{p u_i \frac{\partial v}{\partial x_i}} - \overline{\frac{\partial v u_i p}{\partial x_i}} - \frac{\partial \bar{V} \overline{u_i p}}{\partial x_i} + \overline{v p s_{kk}} + \bar{V} \overline{p s_{kk}} - \frac{\partial (\overline{u_i u_i u_k}/2)}{\partial x_k}$$
$$- \overline{u_i \tau_{ik} \frac{\partial v}{\partial x_k}} + \overline{\frac{\partial v u_i \tau_{ik}}{\partial x_k}} + \frac{\partial \bar{V} \overline{u_i \tau_{ik}}}{\partial x_k} - \overline{v \tau_{ij} s_{ij}} - \bar{V} \overline{\tau_{ij} s_{ij}}. \tag{9.9}$$

In the present context lower-case letters represent fluctuations about the mean, which is denoted with an overbar. The first term on the right-hand side represents production of turbulent kinetic energy by the fluctuating dilatation s_{kk} which, as found in our measurements, is very small and it can be neglected. DNS results of Lee, Lele & Moin (1993) in homogeneous and isotropic turbulence indicated that all the pressure transport terms are negligible and they can be ignored. The turbulent transport term $\partial u_i u_i u_k / \partial x_k$ and the viscous transport are also found to be negligible. The work of Lee *et al.* refers to mass-weighted quantities while the present analysis uses the specific volume as an independent variable. However their conclusions can be extended to the present context if one considers the relation between fluctuating density ρ' and fluctuating specific volume v:

$$v = \frac{-\rho' \bar{v} + \overline{v \rho'}}{\bar{\rho} + \rho'}, \quad \bar{V} = \frac{1 - \overline{\rho' v}}{\bar{\rho}}.$$

If the time-average product of the two fluctuations is small, i.e. $\overline{\rho' v} \ll 1$ then $\bar{V} \approx 1/\bar{\rho}$ and $v \approx -\rho' \bar{v}/\bar{\rho}$. These relations link the fluctuating and mean density with fluctuating and mean specific volume and therefore the conclusions of Lee *et al.* can be invoked to obtain

$$\bar{U}_k \frac{\partial \overline{(u_i u_i/2)}}{\partial x_k} = \overline{p u_i \frac{\partial v}{\partial x_i}} + \overline{v p s_{kk}} + \bar{V}\, \overline{p s_{kk}} - \overline{u_i \tau_{ik} \frac{\partial v}{\partial x_k}} - \overline{v \tau_{ij} s_{ij}} - \bar{V}\, \overline{\tau_{ij} s_{ij}}.$$

Terms containing the fluctuating specific volume v or its derivative are also expected to be small because they are of third order.

Therefore, for the present case of homogeneous turbulence

$$\bar{U}_k \frac{\partial \overline{(u_i u_i/2)}}{\partial x_k} \approx \bar{V}\, \overline{p s_{kk}} - \bar{V}\, \overline{\tau_{ij} s_{ij}}. \tag{9.10a}$$

As has been argued, the pressure–dilatation term in the absence of shock waves is negligible and can also be ignored. Therefore

$$\bar{U}_k \frac{\partial q^2}{\partial x_k} \approx -\bar{V}\, \overline{\tau_{ij} s_{ij}}, \tag{9.10b}$$

where $\epsilon = \bar{E}\, \bar{V}$ and $\overline{q^2} = (1/2)\overline{u_i u_i}$.

Thus measurement of the convection of q^2 by the mean flow can provide a good estimate of the dissipative viscous term ϵ and its length scale L_e through

$$-\bar{U} \frac{\partial \overline{q^2}}{\partial x} = \epsilon = \frac{(\overline{q^2})^{3/2}}{L_e}. \tag{9.11}$$

Once the dissipation length scale is obtained then the dissipation rate ϵ as well as the associated microscales (length, time, velocity) can be calculated. The above equation can be transformed to the following relation by non-dimensionalizing with

the mesh size M:

$$-\frac{\epsilon M}{\bar{U}^3} = \frac{3}{2}\frac{\partial(\overline{u^2}/\bar{U}^2)}{\partial(x/M)}\frac{3}{2}\frac{\overline{(u^2)}^{3/2}}{L_e}\left[\frac{M}{\bar{U}^3}\right]. \tag{9.12}$$

The decay rate of equation (9.12) can be calculated using the coefficients of the power law of equation (8.1). Substitution of (8.1) in (9.12) yields

$$\epsilon = \tfrac{3}{2}nA\left[\frac{x}{M} - \left(\frac{x}{M}\right)_0\right]^{(-n-1)}\left[\frac{\overline{U^3}}{M}\right] \tag{9.13}$$

where A is the decay coefficient, $(x/M)_0$ is the virtual origin, n is the decay exponent, U is the mean flow velocity and M the mesh size.

10. Dissipation rate estimates

The complete time-averaged dissipation rate of turbulent kinetic energy is, for the present homogeneous and isotropic flow,

$$\bar{E} = \mu\,\overline{\omega_k\omega_k} + \tfrac{4}{3}\mu\overline{s_{kk}^2}.$$

Direct evaluation of E requires simultaneous, highly resolved measurements of nine velocity gradients at a given location of the flow field as has been described in the previous section. This has been attempted at several locations in the present flow field. Traditionally, for truly isotropic turbulent flows with moderate or low Mach number fluctuations, the above relation is considerably simplified to $\epsilon = 15\nu\overline{(\partial u/\partial x)^2}$ (Tennekes & Lumley 1972). Thus in the present case the dissipation rate ϵ has been computed by five different methods:

(i) From the decay rate of turbulent kinetic energy and the use of equation (6.12) or (6.13).

(ii) From frequency spectra of velocity fluctuations after invoking Taylor's hypothesis to compute the three-dimensional wavenumber spectrum $E(k)$. The dissipation ϵ can be computed from the integral

$$\epsilon \approx 2\nu\int_0^\infty k^2E(k)\mathrm{d}k. \tag{10.1}$$

(iii) From estimates of $\overline{(\partial u/\partial x)^2}$ and the isotropic relation $\epsilon = 15\nu\overline{(\partial u/\partial x)^2}$. The quantity $\overline{(\partial u/\partial x)^2}$ has been computed by differentiating in time the velocity fluctuation signal and invoking Taylor's hypothesis of frozen turbulence convection.

(iv) From estimates of Taylor's microscale λ obtained from autocorrelations of longitudinal velocity fluctuations. Then the r.m.s. of the fluctuations of the velocity gradient $\overline{(\partial u/\partial x)^2}$ can be obtained independently from $\overline{(\partial u/\partial x)^2} = \overline{u^2}/\lambda^2$ and therefore dissipation can be computed from $\epsilon = 15\nu u^2/\lambda^2$.

(v) By direct measurement of all time-dependent velocity gradients and computation of all the terms appearing in (9.8). This method can also provide an assessment of all the assumptions made in the previous methods of estimating ϵ. The estimates usually obtained from these methods are not identical since the assumptions associated with, and the uncertainties involved in, each of them may differ considerably. The lack of adequate spatial resolution is one of the major source of errors and affects each estimate of ϵ differently. However, even in cases where the estimates of ϵ differ by 50% or more, the estimates of L_e or Kolmogorov's viscous scale $\eta \equiv (\nu^3/\epsilon)^{1/4}$ differ only by 8.5% (see Andreopoulos & Honkan 1996). In the present case the estimates

of ϵ obtained from the decay rate of q^2 and those obtained from Taylor's microscale (autocorrelations) were the most reliable and very close to those obtained by method (v). Based on these estimates of ϵ, the spatial resolution of the probe used in the present investigation was between 7η and 26η, depending on the flow. If one considers that the spatial resolution usually achieved in measurements of compressible flows is of the order of $10^3\eta$ (see Andreopoulos & Muck 1987; Smits & Muck 1987) then the present one appears to be very satisfactory. These values are also comparable to values usually achieved in low Reynolds number incompressible flows. In the case of vorticity measurements the spatial resolution was also in the range of 7η to 30η. However, increasing evidence suggest that Taylor's microscale λ and not η should be used to evaluate the spatial resolution of probes (see Tsinober, Kit & Dracos 1992, and HA). In this case the spatial resolution of the probe is between 0.6λ and 3λ and therefore the expected attenuation of the measurement of vorticity r.m.s. is not very significant.

11. Flow homogeneity and isotropy

The flow visualization experiments and quantitative analysis of velocity and temperature obtained at different locations simultaneously across a section of the tube indicated that the flow is homogeneous within 85% of the diameter. Evidence of the flow quality was provided in § 4 while a full documentation of the flow quality in the shock tube is provided by Briassulis *et al.* (1995).

The flow isotropy was verified directly and indirectly. Direct verification is provided by computing the anisotropy tensor b_{ij} of the velocity field:

$$b_{ij} = \frac{\overline{u_i u_j}}{\overline{u_i u_i}} - \tfrac{1}{3}\delta_{ij}, \tag{11.1}$$

where u is velocity fluctuation about the mean and δ is the Kronecker delta. Generally, grid-generated turbulence tends to be anisotropic with the streamwise component slightly larger than the cross-stream components. Compte-Bellot & Corrsin (1966) were able to generate turbulence very close to an isotropic state by introducing a contraction after the grid. However, in most experiments where isotropic turbulence has been configured by using biplane grids all turbulent quantities have been found to agree reasonably well with isotropic conditions at sufficiently large distances from the grid, even with the presence of slight anisotropy which usually decreases with downstream distance from the grid.

The present data, shown in figure 10, suggest a rather good degree of isotropy, with minor variations, well within established margins. For comparison it should be mentioned that for boundary layers $b_{11} = 0.45$ and $b_{12} = 0.15$. Anisotropy of the present flow field is compared with one of the latest and most complete studies, that of Tsinober *et al.* (1992) in incompressible flows. It appears the values of b_{ij} in the present experiment are confined within the band ± 0.075 in the region $30 < x/M < 60$ and within the band ± 0.035 in the region $65 > x/M$. It is also evident from figure 10 that the degree of flow isotropy achieved in the present flow configuration is slightly better than that of Tsinober *et al.* (1992). Both data sets show that anisotropy decrease with downstream distance.

The anisotropy of the vorticity field is also shown in figure 10. The anisotropy tensor for vorticity is defined similarly as

$$c_{ij} = \frac{\overline{\omega_i \omega_j}}{\overline{\omega_i \omega_i}} - \tfrac{1}{3}\delta_{ij}. \tag{11.2}$$

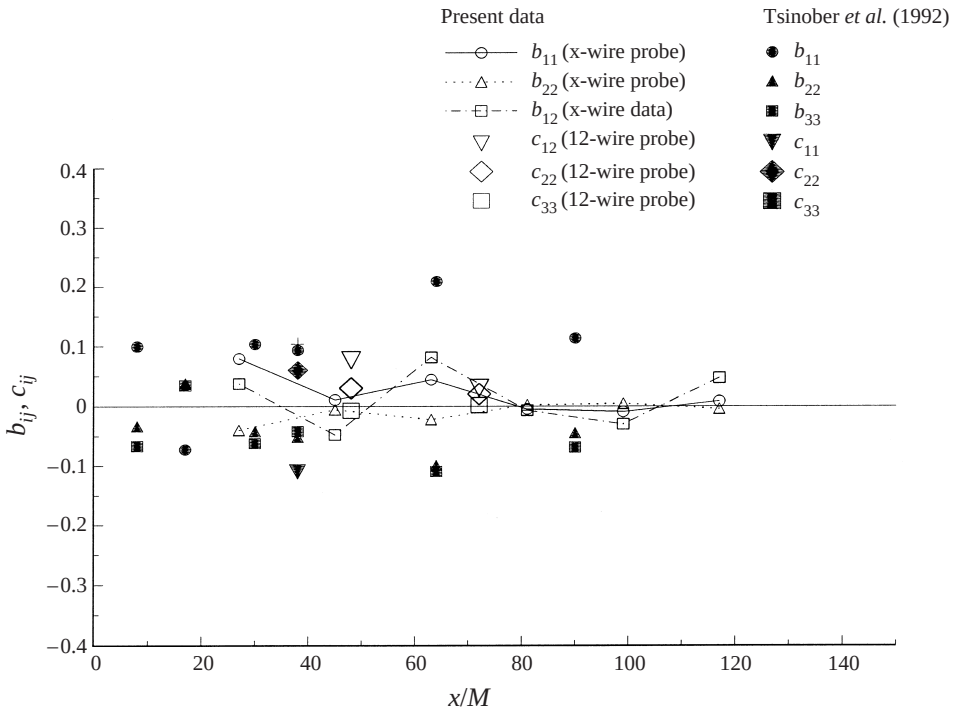

FIGURE 10. Anisotropy tensors b_{ij} (velocity field) and c_{ij} (vorticity field).

Values of c_{ij} are compared with the vorticity data of Tsinober *et al.* (1992). Our present vorticity data indicate that the anisotropy of the flow is well within the established limits. The reasonably low values of the anisotropic tensors b_{ij} and c_{ij}, shown in figure 10, establish the isotropic nature of the present flow generated in the shock tube.

Indirect evidence of isotropy was provided by considering the skewness of velocity fluctuations and the skewness of velocity derivative (Tavoularis *et al.* 1978; Mohamed & LaRue 1990).

Figure 11 presents the skewness of velocity fluctuations for three mean flow Mach numbers obtained in the experiments with the 5×5 ($M = 5.08$ mm) and 3×3 ($M = 8.5$ mm) grids. It appears that S_u remains constant and close to zero for all measured downstream locations. The data of S_u obtained with the 12-wire probe are also plotted for comparison with those obtained with x-wires. These values are also close to zero.

The skewness of the velocity derivative $S_{\partial u/\partial x}$ represents the average rate of production of mean-square vorticity by vortex stretching (Batchelor 1953) and it is related, according to Tavoularis *et al.* (1978), to the spectral energy transfer which depends on the turbulent Reynolds number, Re_λ. Computations of $S_{\partial u/\partial x}$ indicated that the results are affected by the numerics of the algorithm used to evaluate $\partial u/\partial x$ or $\partial u/\partial t$. In order to avoid excessive spikes and overshoots in the signal, the central-difference numerical scheme was used to compute $\partial u/\partial t$, which required the use of three sequential digital points. However, very high rates of data sampling were required in the present experiments in order to capture accurately the arrival of the incident or reflected shock waves. This created over-sampled turbulence data which biased the computation of $S_{\partial u/\partial x}$. In order to demonstrate the effects of sampling rate on $S_{\partial u/\partial x}$

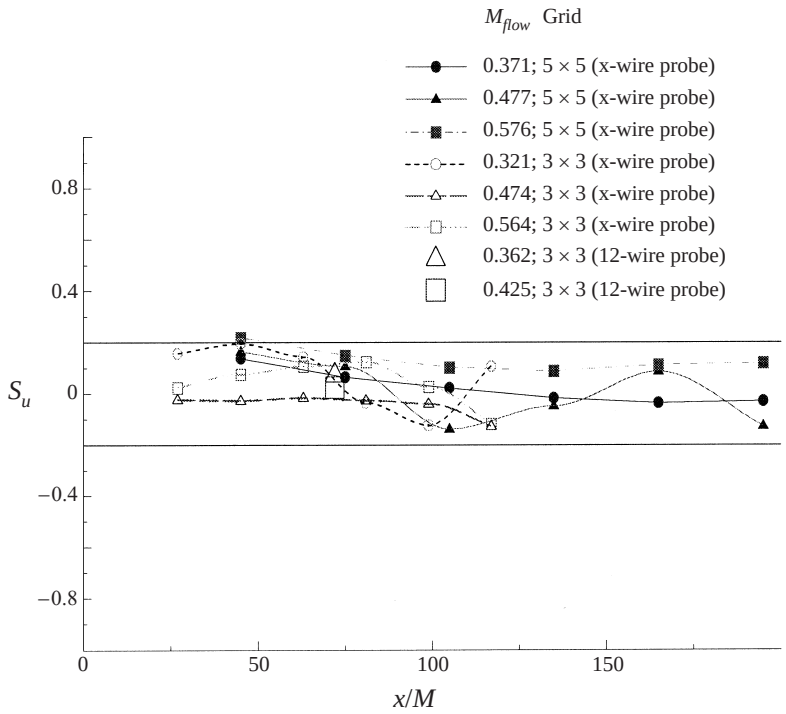

FIGURE 11. Skewness of velocity fluctuations for three different flow fields.

adjustable sampling was performed by skipping data points in the computations. Taylor's hypothesis was used to convert the time interval between measurements Δt to spatial distance Δx. Figure 12(*a*) shows the effect different effective sampling has on the value of $S_{\partial u/\partial x}$ for three M_{flow}. Values of Δx have been non-dimensionalized by the corresponding Taylor microscale λ of each flow field. It has been found in the past by Tsinober *et al.* (1992) and HA that the most appropriate scale for the statistics of velocity gradients is λ, which also represents the smallest scale to resolve for reliable measurements of these velocity gradients. It is therefore appropriate to adopt the value of $S_{\partial u/\partial x}$ at $\Delta x = \lambda$ as the most plausible value.

Tavoularis *et al.* (1978) presented a comprehensive study of values of the skewness of velocity derivative for a variety of flow fields and Re_λ. From this study, if one considers the data obtained from isotropic grid turbulence, it can be observed that $S_{\partial u/\partial x}$ decreases with Re_λ for $Re_\lambda > 5$. The theoretical analysis of George (1992) also suggests that $S_{\partial u/\partial x}$ varies as Re_λ^{-1}. Typical values for $S_{\partial u/\partial x}$ are shown in figure 12(*b*) for three different flow cases of the present investigation together with values obtained by other researchers in various turbulent flow fields. Since λ increases with distance from the grid the values obtained in the present investigation and shown in this figure represent the average value of all the measured values downstream of the grid for a given experiment. The values obtained are between 0.2 and 0.4, a range which is lower than the $S_{\partial u/\partial x}$ value at $Re_\lambda \approx 5$.

The self-preservation theory of George (1992) suggests that the value of the product $S_{\partial u/\partial x}\, Re_\lambda$ depends on initial conditions and asymptotically should vary as $Re_M^{1/2}$ as it has also been proposed by Batchelor & Townsend (1947). Figure 12(*c*) shows values of the ratio $S_{\partial u/\partial x} Re_\lambda / Re_M^{1/2}$ plotted against Re_M for three different Mach numbers, M_{flow}, computed from measured data obtained in the present investigation. The

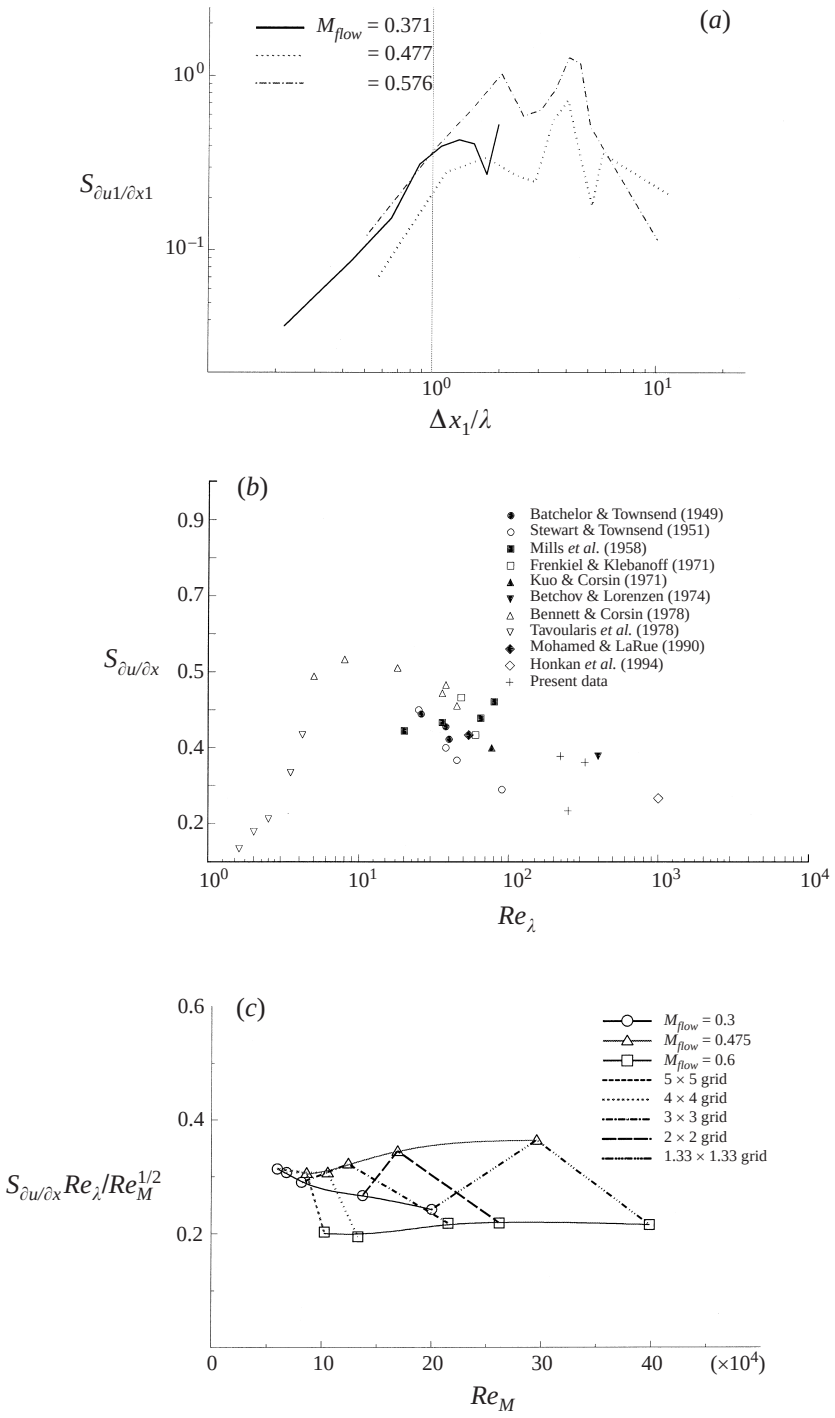

FIGURE 12. Skewness of (*a*) velocity fluctuations and (*b*) the derivative of velocity fluctuations, for different flow fields. (*c*) The ratio $S_{\partial u/\partial x}Re_\lambda/Re_M^{1/2}$ for various M_{flow}. Values obtained with the same grid are connected with dashed lines.

data show that this ratio maintains a reasonably constant value which depends on M_{flow}. For the lowest $M_{flow} = 0.3$ this value appears to be 0.28 on average, while for $M_{flow} = 0.475$ it increases to a new level of 0.32. The value of the constant reduces to 0.21 for $M_{flow} = 0.6$. It should be noted that the data of Batchelor & Townsend show that the asymptotic value of this constant is 0.12. The apparent difference between the present data and those of Batchelor & Townsend may be due to the fact that all flow cases investigated in the present work can be considered compressible. Thus compressibility may increase the value of this constant. The self-similarity theory of George (1992) has been developed for incompressible flows. It remains to be seen whether self-similarity is an attainable state of compressible turbulence. The fact that there is a constant value of the ratio $S_{\partial u/\partial x} Re_\lambda / Re_M^{1/2}$ for each M_{flow} suggests that self-similarity theory may be extended to weakly compressible turbulence. It should be noted that in the present approach an attempt has been made to identify the effects of flow Mach number on $S_{\partial u/\partial x}$ by considering that M_{flow} is part of the initial conditions. Another approach could be to only consider the data obtained with the same grid. Figure 12(*c*) also shows the same data as before with dashed lines connecting data points corresponding to the same grid. This type of interpretation ignores the effect of flow Mach number and the data clearly show that the ratio $S_{\partial u/\partial x} Re_\lambda / Re_M^{1/2}$ is not constant. Both interpretations of the present data clearly demonstrate that the theory needs modification to account for the effects of compressibility.

It can therefore be concluded from all the results presented in this section that direct and indirect evidence exists to support the argument that the present flow is nearly homogeneous and isotropic.

12. Decay of turbulent kinetic energy and Mach number fluctuations

In general, it is expected that turbulence quantities downstream of the grid will depend on the grid itself which is characterized by its shape and geometry, including solidity, σ, and mesh size, M, and the initial conditions which include the Reynolds number based on mesh size Re_M and flow Mach number M_{flow} downstream of the grid. It is not always possible to separate the effects of each of $\sigma, M/Re_M$ or M_{flow} on flow quantities, from each other.

The typical decay of turbulent kinetic energy data with x/M was fitted with the power law of equation (8.2). It should be noted that this relation which describes the decay rate of turbulence is based on entirely empirical grounds. In the early experiments of Simmons & Salter (1934) and Dryden (1943) the decay rate of turbulence was found to be inversely proportional to $x - x_0$. Subsequent experiments by Corrsin and co-workers indicated that the decay rate described by (8.1) provides a better fit to the experimental data with n in the range of 1.1 to 1.35.

In the present work, the variables $A, (x/M)_0$, and n were determined so that the residual deviation from the original data is minimized. Thus all variables were determined concurrently under the condition of minimum deviation. In that respect this approach represents a departure from previous practice where only two of the three parameters were determined through a best fit procedure while the third one was fixed. An exception to this past practice is the work of Mohamed & LaRue (1990). A consequence of this approach is that n can reach any positive value and not only values > 1 as usually is the case in previous works.

A sensitivity analysis was carried out to demonstrate how uncertainties in the measurements could affect the values of $A, (x/M)_0$, and n and the estimates of dissipation rates and length scales obtained through the power law. The Appendix

gives the analysis and provides estimates of the expected variation in the values of these quantities. This analysis has indicated that a 10% variation in q^2 results in a 10% variation in ϵ, 5% variation in L_e and 3% variation in λ. In general, the present flow parameters remain within reasonable limits of variation even when the power-law decay coefficients were allowed to vary in an arbitrary manner.

It should be emphasized that the applicability of the empirical power-law decay does not necessarily imply isotropy. Thus the data used for the best fit procedure not only had to obey the power law but also to be in the region where nearly isotropic conditions hold. Thus not all experimental data were considered in the determination of $A, (x/M)_0$, and n. In several experiments, the point closest to the grid had to be excluded because the isotropy requirements were not satisfied. The criterion used to determine the degree of flow isotropy was based on the values of the anisotropy tensors in a particular experiment like those shown in figure 10. Values of the anisotropy tensor b_{ij} were available for all experiments while values of c_{ij}, the vorticity anisotropy tensor, were available for a few cases only.

The present work documents the effects of the mesh size/mesh Reynolds number as well as the flow Mach number on the quantities $A, (x/M)_0$, and n. The importance of these parameters is evident when one considers (9.13). Once these parameters are available the dissipation rate of turbulent kinetic energy ϵ, the corresponding dissipative length scale L_e and Taylor's microscale λ can be computed.

Several grids were used in the present experiments so that the Reynolds number based on the mesh size Re_M, as well as the dominant length scales present in the flow, can be varied. The mesh Reynolds number ranged from 35 000 to 600 000 while the mesh size ranged from 3 to 25 mm. The Reynolds numbers achieved in the present investigation are amongst the highest ever attempted in laboratory configurations of nearly homogeneous and nearly isotropic turbulence. Measurements were obtained at three different driver pressures/shock strengths. The bulk parameters of all flow cases are shown in table 1. The grids in terms in their solidity σ can be classified in three different groups. The low solidity group with $\sigma = 0.26$ is composed of the 1.33×1.33 grid only. The medium solidity group contains three grids, the 5×5, the 3×3 and the 2×2, each with solidity very close to each other and within 2.5% of their average value of $\sigma = 0.38$. The last group contains the 4×4 grid only, with solidity $\sigma = 0.44$, which is the highest used in the present experiments.

Figure 13(a) demonstrates the power-law decay behaviour of the measured data as described by equation (8.2). The results of nine experiments are plotted in logarithmic scales in this figure. They include three different grids at three different pressures/mean flow Mach numbers which are in the subsonic range of $0.3 \leqslant M_{flow} \leqslant 0.6$, placing the flows in the weakly to moderately compressible regime. These grids have approximately the same solidity, $\sigma = 0.38$.

Several conclusions can be drawn from these data. First those shown in this log-log plot indicate that Mach number fluctuations M_t decay with downstream distance x/M according to the proposed power law

$$M_t^2 = B\left[\frac{x}{M} - \left(\frac{x}{M}\right)_0\right]^{-n}. \tag{12.1}$$

Second, the exponent n and the constant B depend on the grid, Mach number or Re_M. Third, the region where isotropy starts depends more on the grid for a given solidity than on the flow Mach number or Re_M. The onset of isotropy is delayed for fine grids, i.e. grids with small mesh size M. It also appears that M_t increases with increasing Mach number of the flow, M_{flow}, in all experiments with the same grid.

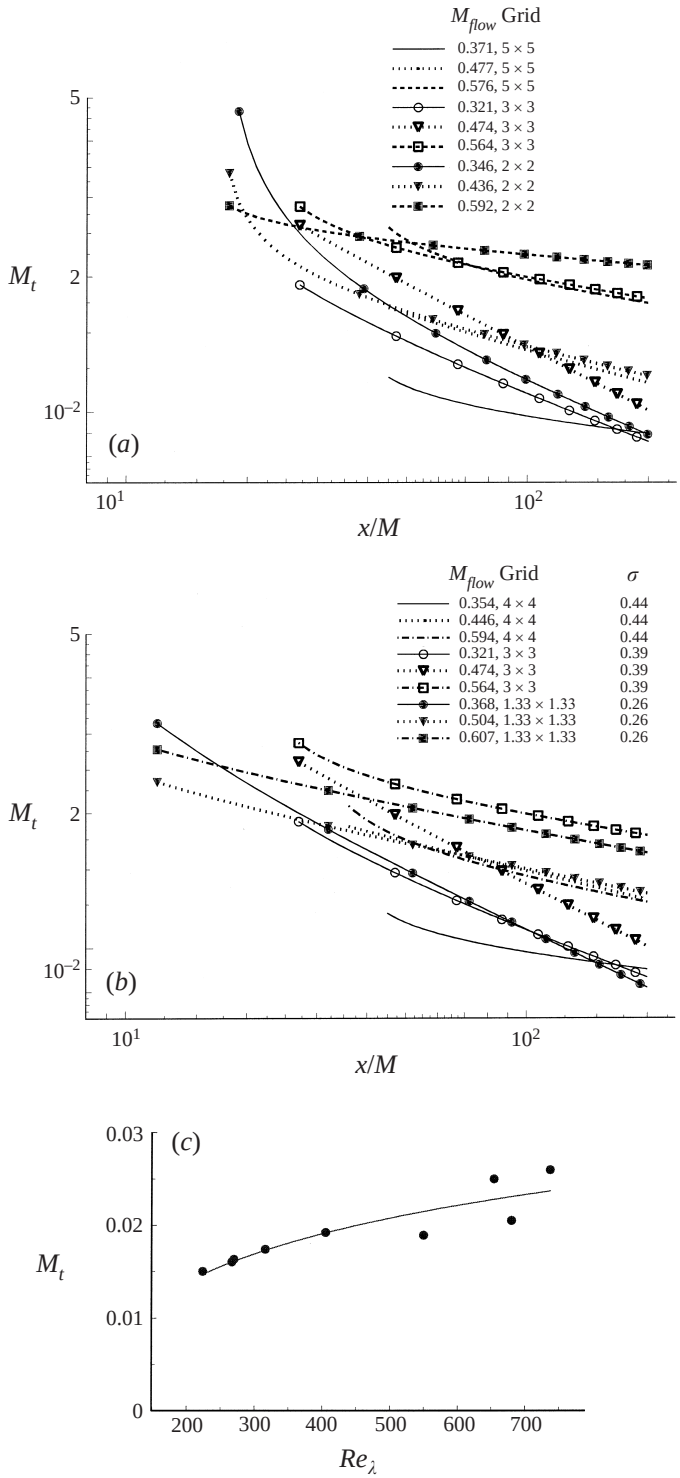

FIGURE 13. Mach number fluctuations for various experiments with (*a*) grids of nearly the same solidity of $\sigma = 0.38$ and (*b*) grids of various solidity. (*c*) Typical turbulent Mach number fluctuations at $x/M = 60$ against Re_λ.

This behaviour is more evident at downstream positions with $x/M > 30$. Mach number fluctuations, M_t, for a given M_{flow} also increase with increasing mesh size.

In order to identify the effects of solidity on Mach number fluctuations, the data of the three major solidity classes have been plotted separately in figure 13(b). The 3×3 grid has been chosen as a typical of the medium solidity group. The results of the Mach number fluctuation decay show that isotropy starts sooner at low solidity grids with $\sigma = 0.26$ rather than at grids with high σ. The data also show that there is no apparent trend of how M_t changes with σ at constant M_{flow}. There is, however, evidence that M_t increases with increasing M_{flow} at constant σ, except for the 4×4 grid where the values of M_t are about the same at the two highest M_{flow}. Unfortunately no combination of grids could be obtained so that the effect of solidity σ on M_t could be considered at constant mesh size M.

Figure 13(c) shows a typical variation of the Mach number fluctuations obtained in the present investigation with Re_λ at $x/M = 60$, a location where turbulence appears to be homogeneous and isotropic in all experiments carried out at various mean flow Mach numbers M_{flow}. M_t and Re_λ are two independent variables used frequently in DNS to characterized the isotropic turbulence instead of M_t and Re_M, which are used mostly in experimental research where grids are used to generate isotropic turbulence. The present data demonstrate a general trend showing that Mach number fluctuations increase with increasing Re_λ, a finding which has also been supported by DNS observations.

In the following an attempt has been made to investigate the effects of M_{flow} and Re_M on B, n and x_0 which appear in (12.1). The effect of Re_M or M on the coefficient B for three different Mach numbers is shown in figure 14(a). It should be mentioned that the coefficient B shown above is related to the coefficient A of the velocity fluctuation power-law decay through the relation $B = 3AM_{flow}^2$ which clearly suggests that B depends on M_{flow}^2. In addition to this rather obvious dependence of B on M_{flow}, there is the yet unknown Mach number dependence of A. This is shown in figure 14(b) where the effects of Re_M or M on the coefficient A for three different Mach numbers is demonstrated. Reynolds number variation was produced by changing the mesh size under a relatively constant velocity, i.e. Mach number M_{flow}.

For the lowest velocity flow field tested ($U \approx 120\,\mathrm{m\,s^{-1}}$), which corresponds to a mean flow Mach number of 0.30, the decay coefficients A or B, which are proportional to each other at a specific M_{flow}, increase in a nonlinear fashion with increasing mesh size M or Re_M as shown in figure 14(a). As the Mach number increases, B is substantially decreased and it appears to be independent of mesh size. The same holds for the highest Mach number tested, where the decay coefficient is further suppressed. It can be concluded that the decay coefficient A or B decreases when the flow Mach number increases and that it is independent of the mesh size M and M_{flow} at high M_{flow}.

In the above discussion the effects of grid solidity, σ, on B or A, in addition to the effects of M_{flow} and Re_M, was not considered. If the three grids which have the same solidity are considered then the effects of M_{flow} and Re_M on B or A will be the same as previously described and all the conclusions made above will still be valid. An attempt has been made, however, to assess independently the effects of solidity on B or A by assuming that the dependence of σ on the resistence or static pressure drop coefficient, K, is the same as in the case of fine screens (see Laws & Livesey 1978; Groth & Johansson 1988):

$$K = f(Re_d)\left[\frac{1}{(1-\sigma)^2} - 1\right], \tag{12.2}$$

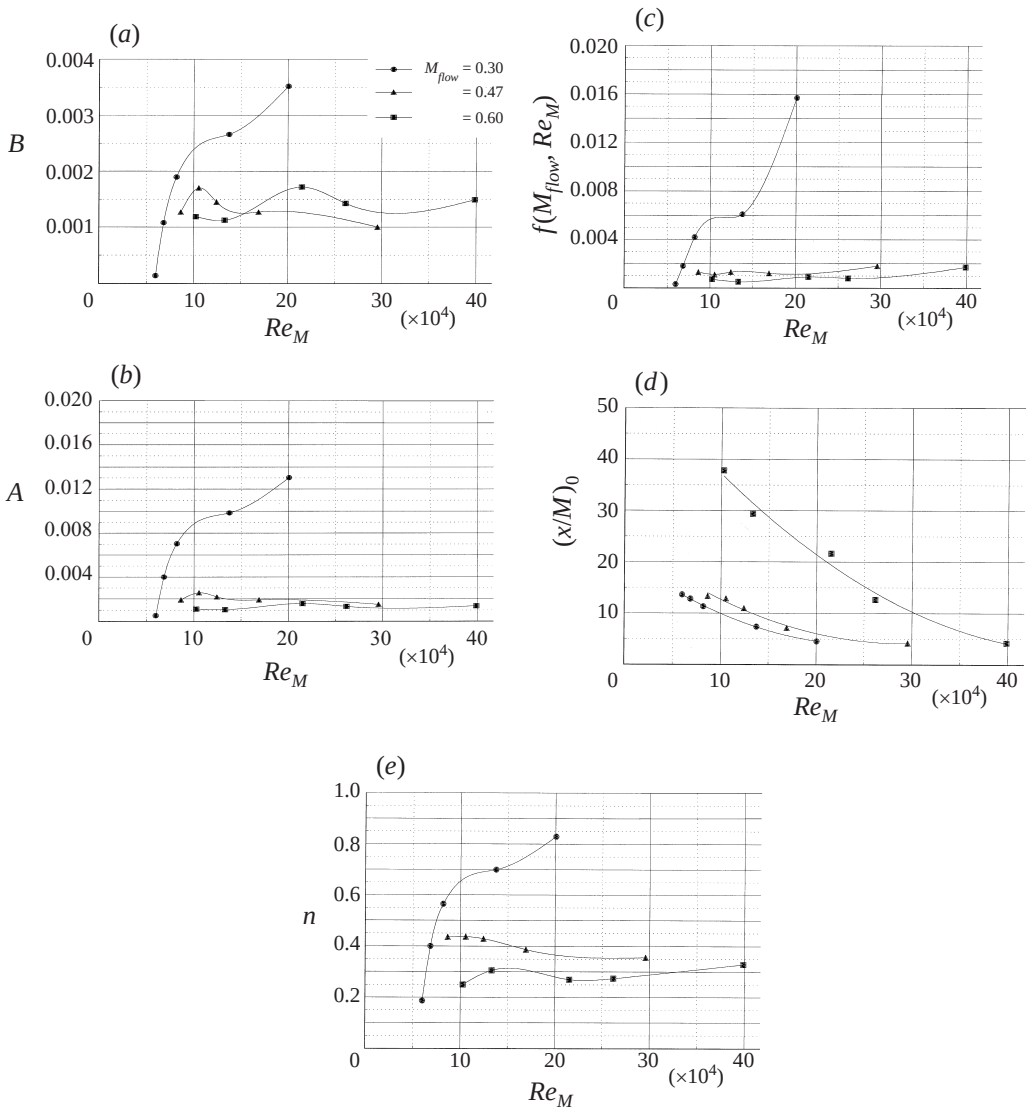

FIGURE 14. (*a*) Decay coefficient B and (*b*) decay coefficient A vs. Re_M for three different Mach numbers. (*c*) Effects of Re_M and M_{flow} on function $f(Re_M, M_{flow}) = A/F_\sigma$. (*d*) Virtual origin and (*e*) decay exponent n vs. Re_M for three different Mach numbers.

where f is a function depending only on the Reynolds number based on the rod diameter, Re_d. It is known that A is proportional to K for fine screens and therefore the above relation can be extended into compressible flow cases to yield

$$A = f(Re_M, M_{flow})F_\sigma, \tag{12.3}$$

where $F_\sigma = [1/(1-\sigma)^2 - 1]$ is the function which describes the effects of σ. Typical values for F_σ are 0.86 for the 1.33×1.33 grid, 1.68 for the 3×3 grid and 2.188 for the 4×4 grid. Thus the values of A will not be substantially affected if the effects of solidity have to be taken into account. Figure 14(*c*) shows the dependence of the function $f(Re_M, M_{flow}) = A/F_\sigma$ on Re_M, and M_{flow}. These data indicate that qualita-

tively A and $f(Re_M, M_{flow})$ exhibit the same Re_M and M_{flow} effects. Quantitatively, the data show some differences between them which cannot be considered as substantial.

It should be noted that the values of $f(Re_M, M_{flow})$ obtained in the present investigation at rather high Reynolds numbers could not be directly compared with the low Reynolds data reported by Groth & Johansson (1988) for fine grids because of the large difference in Re_d.

In the past, it has been demonstrated that only the coefficient A depends on solidity. If this behaviour is assumed to be valid in the present case then the exponent, n, and the virtual origin, $(x/M)_0$ will depend on Re_M, and M_{flow} only. In the following, the effects of Re_M and M_{flow} on n and $(x/M)_0$ will be demonstrated.

The virtual origin $(x/M)_0$ strongly depends on the mesh size/Re_M. This is shown in figure 14(d) where the position of the virtual origin is plotted against Re_M for a constant Mach number flow for three different flow Mach numbers. In all cases it was observed that the virtual origin approaches the grid as the mesh size or Re_M increases.

The effects of the Mach number at a particular Re_M can also be seen in figure 14(d). The virtual origin is strongly affected at the highest Mach number only, while for the medium and low M_{flow} cases it is moderately affected. At the highest Mach number where the associated compressibility effects are expected to play a bigger role, the virtual origin moved further away from the grid at a given Re_M. It is also interesting to observe, in the same figure, that this effect is diminished for the largest mesh size grid. Namely, the virtual origin at high Re_M appears to reach the same normalized value of about 5 for each of the investigated Mach numbers.

The decay exponent n, shown in figure 14(e), is also substantially affected by the Mach number of the flow field. It is clear from this figure that n is decreasing with increasing Mach number. The effect of the mesh size on the decay exponent can also be observed. It behaves similarly to the decay coefficient A. Namely, for the lowest Mach number it increases with increasing mesh size/Re_M. That means that for finer grids, i.e. of small mesh size, there are larger decay rates than for coarser grids. At a first glance this statement appears to contradict previous notions based on fixed-n fitting of the data, but if we consider equation (9.13) then the dissipation rate ϵ is proportional to $nA[(x/M) - (x/M)_0]^{-(n+1)}$. Thus ϵ will increase if n decreases.

When the Mach number increases the decay exponent n decreases substantially. From a value of 0.8 at $M_{flow} = 0.3$, for instance, n drops to 0.3 at $M_{flow} = 0.6$ in the case of $Re_M = 200\,000$. This is a reduction in the decay of more than 60% for a 100% increase in Mach number. Thus, it appears that the major effect of compressibility is a substantial reduction in the decay rate. The second interesting behaviour of the exponent n is that at high M_{flow} it remains almost independent of Re_M where it reaches a value of about 0.3.

A typical decay of velocity fluctuations, as fitted by the power law, for the 5.08 mm mesh size grid is shown in figure 15. The velocity fluctuations are higher at higher Mach numbers which also correspond to higher Re_M. The effect of higher velocity fluctuations cannot simply be attributed to the increase of the mean Mach number and the associated compressibility effects of the flow but also to the increase of Re_M. Although Mach number and Reynolds number are two different independent variables they may cause quite similar effects on the flow which may be difficult and sometimes impossible to distinguish clearly from each other. A 4-fold increase in pressure, for instance, which corresponds to 100% change in Mach number and Reynolds number, results in a 3-fold increase in the Mach number fluctuations M_t,

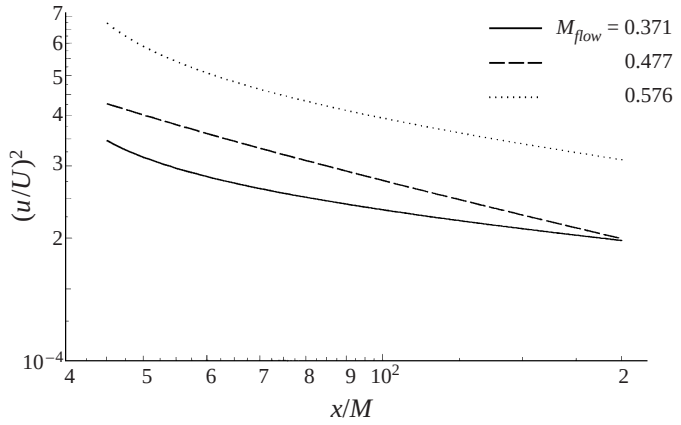

FIGURE 15. Decay of velocity fluctuations for various Mach numbers; $M = 5.08$ mm.

throughout the entire flow field. Most probably this increase in M_t and $(u/U)^2$ can be attributed to both parameters, i.e. M_{flow} and Re_M.

An attempt has made to identify the effects of M_{flow} and Re_M on M_t, ϵ, L_e and λ in several of the present cases, by considering the dependence of the power law decay coefficients on M_{flow} and Re_M shown in figure 14(*a–e*). In order to explore how q^2 or M_t^2 will change with M_{flow} or Re_M, the partial derivatives $(\partial M_t^2/\partial M_{flow})|_{Re_M}$ or $(\partial M_t^2/\partial Re_M)|_{M_{flow}}$ must first be evaluated. Differentiation of (12.1) yields

$$\frac{1}{M_t^2}\left(\frac{\partial M_t^2}{\partial M_{flow}}\right)\Bigg|_{Re_M} = \frac{1}{B}\left(\frac{\partial B}{\partial M_{flow}}\right) - \left(\frac{\partial n}{\partial M_{flow}}\right)\log\left[\frac{x}{M} - \left(\frac{x}{M}\right)_0\right] + n\Big/\left[\frac{x}{M} - \left(\frac{x}{M}\right)_0\right]\left(\frac{\partial (x/M)_0}{\partial M_{flow}}\right). \tag{12.4}$$

The experimental data shown in figure 14 indicate that $(\partial B/\partial M_{flow}) < 0$, $(\partial n/\partial M_{flow}) < 0$ and $(\partial (x/M)_0/\partial M_{flow}) > 0$. Thus the relative magnitude of the three terms in the right-hand side of (12.4) will determine the sign of $(\partial M_t^2/\partial M_{flow})|_{Re_M}$. It appears that the first term is always negative and the last two terms are always positive. The above derivatives were numerically calculated and it was found that $(\partial M_t^2/\partial M_{flow})|_{Re_M} > 0$ in any flow with $[x/M - (x/M)_0] > 60$ through the range of Mach numbers investigated here. This finding agrees well with the data shown previously in figure 13(*a*), where it was shown that M_t fluctuations increase with M_{flow}.

Similarly to (12.4) the other partial derivative can be estimated:

$$\frac{1}{M_t^2}\left(\frac{\partial M_t^2}{\partial Re_M}\right)\Bigg|_{M_{flow}} = \frac{1}{B}\left(\frac{\partial B}{\partial Re_M}\right) - \left(\frac{\partial n}{\partial Re_M}\right)\log\left[\frac{x}{M} - \left(\frac{x}{M}\right)_0\right] + n\Big/\left[\frac{x}{M} - \left(\frac{x}{M}\right)_0\right]\left(\frac{\partial (x/M)_0}{\partial Re_M}\right). \tag{12.5}$$

The present data show that $(\partial B/\partial Re_M) > 0$ and $(\partial n/\partial Re_M) > 0$ for $M_{flow} = 0.3$ and that both $(\partial B/\partial Re_M) \approx 0$ and $(\partial n/\partial Re_M) \approx 0$ for the higher M_{flow}. The data also show

that $\partial(x/M)_0/\partial Re_M < 0$ for all M_{flow}. Consequently it appears that $\partial M_t^2/\partial Re_M|_{M_{flow}}$ is positive at low M_{flow} and slightly negative at high M_{flow}.

The availability of values of the partial derivatives at several values of Re_M and M_{flow} allows us to evaluate contributions to changes in M_t^2 which are caused by Re_M effects and/or by M_{flow} effects through the relation

$$\Delta M_t^2 = [\partial M_t^2/\partial M_{flow}]\Delta M_{flow} + [\partial M_t^2/\partial Re_M]\Delta Re_M. \tag{12.6}$$

The data show that Re_M effects are about the same order of magnitude and of the same sign as Mach number effects at low Mach numbers and low Re_M. They diminish gradually as M_{flow} and Re_M increase, as is evident from the data of figure 14(*a*). Thus, in most cases, compressibility effects prevail over Reynolds number effects at high M_{flow} and high Re_M.

13. Dissipation rate and length scales

Figure 16(*a*) shows the dissipation rate of kinetic energy ϵ for one grid (5×5) with mesh size $M = 5.08$ mm at different flow Mach numbers. Two dissipation datasets are shown in this figure, which have been computed by two different methods. In the first method, ϵ has been determined from the decay rate of turbulent kinetic energy by using equation (9.13). The second set of dissipation data has been computed from the dissipation spectra calculated through the relation (10.1). The two datasets agree reasonably well with each other, particularly in the far field.

From the data shown in figure 16(*a*), it appears that ϵ increases with increasing Mach number in all investigated flows with the $M = 5.08$ mm grid. This behaviour is quite similar to that of the decay of q^2. Dissipation varies proportionally to x^{-n-1} while q^2 varies as x^{-n}. It remains to be seen whether this is a Mach number effect or is due to Reynolds number increase.

The data shown in figure 16(*a*) are non-dimensionalized by M/U_1^3 and replotted in figure 16(*b*) where the same behaviour can be observed: non-dimensional dissipation increases with flow Mach number M_{flow}. However, in the case of coarser grids non-dimensional dissipation $\epsilon M/U_1^3$ is decreased with increased M_{flow}. Figure 16(*c*) shows values of the non-dimensional dissipation for the case of the 2×2 grid with $M = 12.7$ mm and the same solidity as the 5×5 grid. These data demonstrate that dissipation is reduced when the flow Mach number increases in the case of coarse grids. As will be seen later, direct measurements of dissipation also confirm this conclusion.

The difference between coarse and fine grids as to how the dissipation $\epsilon M/U_1^3$ varies with M_{flow} can be attributed to the effects of Re_M in addition to the obvious reason of grid dependence. It should be noted that in the case of the fine grids with $M = 5.08$ mm Re_M reaches values from 59 000 to 102 000 while in the case of the coarser grids with $M = 12.7$ mm Re_M reaches values from 137 000 to 260 000.

The dissipation rate of kinetic energy ϵ for various mesh sizes is shown in figure 17 for the highest Mach number tested. In this figure the effects of Re_M or M at a fixed flow Mach number, M_{flow}, are depicted. The data in figure 17 suggest that coarser grids, i.e. higher Re_M, produce lower dissipation rates, ϵ, at constant M_{flow} when compressibility effects are high. In the absence of large compressibility effects, which are typical in the lowest Mach number flow fields tested, the reverse influence of the mesh size on ϵ can be found as shown in figure 18. In this figure, dissipation data non-dimensionalized by the mean velocity and mesh size for the lowest Mach number flow field tested, $M_{flow} = 0.35$, is plotted for various mesh sizes. The reverse

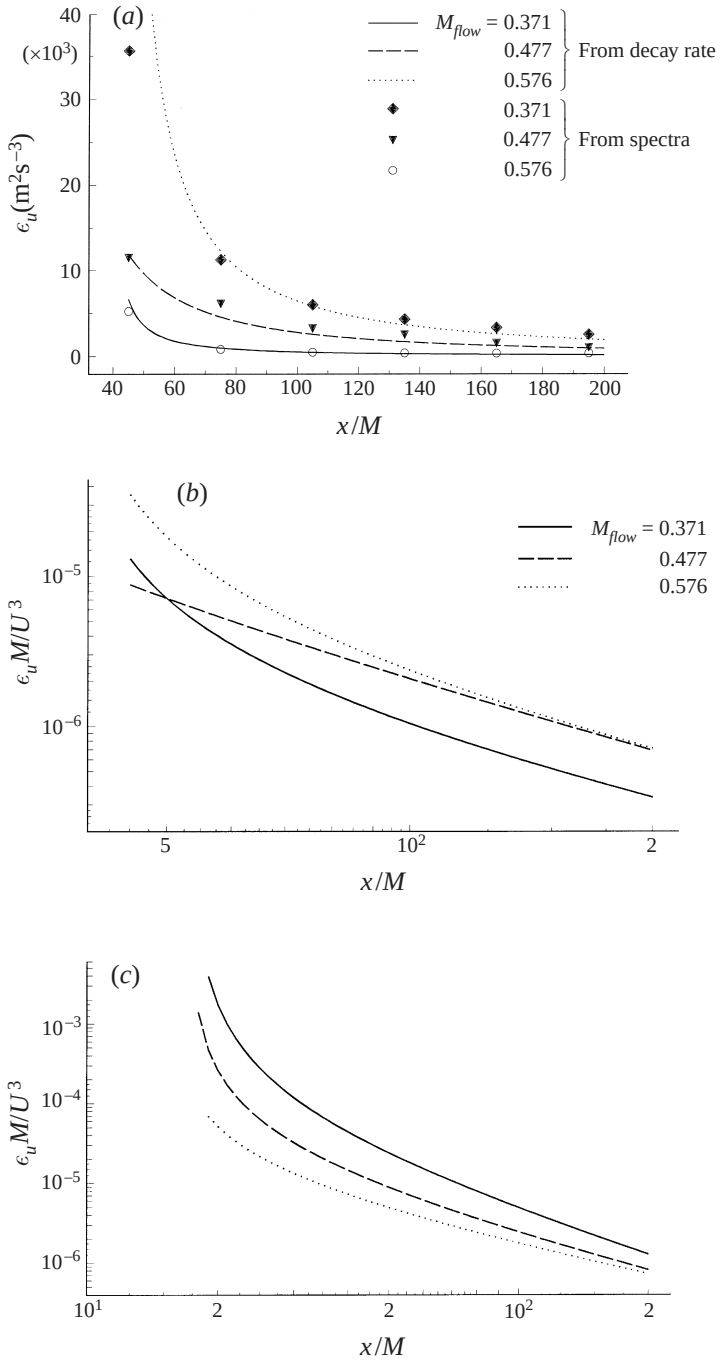

FIGURE 16. (*a*) Dissipation rate of kinetic energy (for $M = 5.08$ mm), and (*b*, *c*) non-dimensional dissipational dissipation rate for $M = 5.08$ and 12.7 mm, respectively, vs. x/M for three Mach numbers.

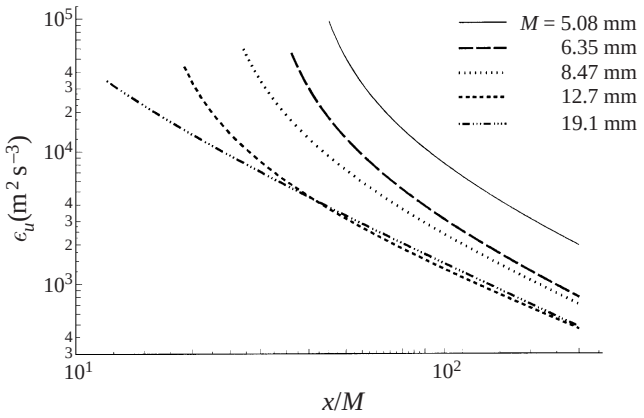

FIGURE 17. Dissipation rate of kinetic energy for various mesh sizes. $M_{flow} = 0.6$.

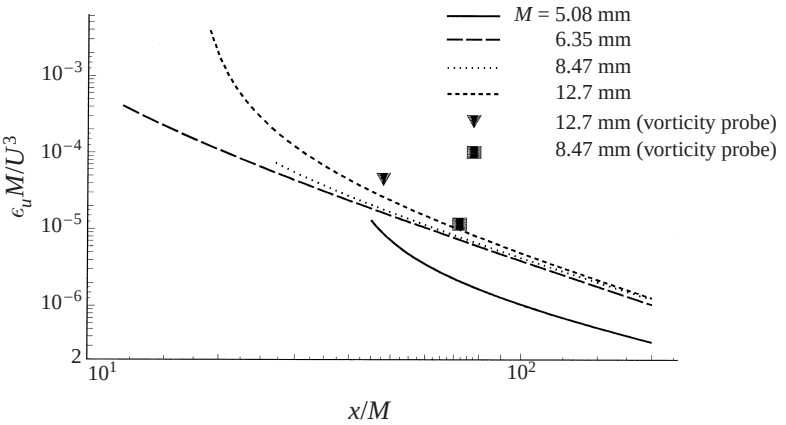

FIGURE 18. Non-dimensional ϵ for $M_{flow} = 0.35$ and various mesh sizes.

trend is observed for $\epsilon M/U^3$ in the absence of strong compressibility effects. In this case, the coarser grid with the largest mesh size and highest Re_M shows the largest non-dimensionalized dissipation rate of kinetic energy. Since the mean flow field velocity U is equal for all cases plotted the effect presented in this figure is mainly due to the Mesh size M and Re_M.

Figure 18 also shows the dissipation rate data obtained with the vorticity probe. In this case the total dissipation rate was computed directly from the measured time-dependent velocity and density gradients. These data appear to be 5% to 15% higher than the data obtained from the decay rate of turbulent kinetic energy. This difference is well within the experimental uncertainty associated with the measurements of dissipation.

The data shown in figure 17 are non-dimensionalized with M/U^3 and replotted in figure 19. The effect of compressibility is rather striking at this $M_{flow} = 0.6$ and the results consistently indicate that $\epsilon M/U^3$ increases with decreasing mesh size/Re_M.

Even in the case of the medium Mach number flow field tested, compressibility effects can be observed in the dissipation data shown in figure 20. These data also demonstrate that the coarser grids with the greater mesh sizes and higher Re_M flow field produce a lower dissipation rate, ϵ. The dissipation rate of kinetic energy for

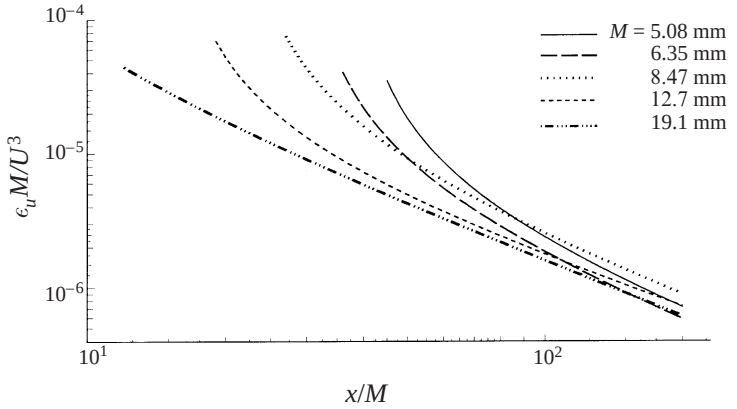

FIGURE 19. Non-dimensional ϵ for $M_{flow} = 0.6$ and various mesh sizes.

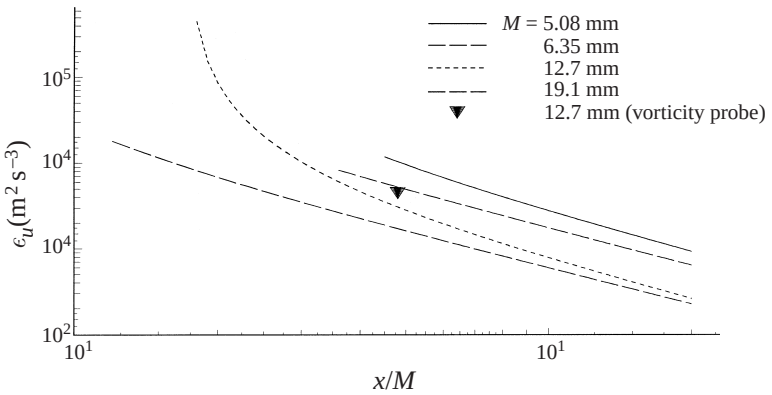

FIGURE 20. Dissipation rate of kinetic energy for various mesh sizes at $M_{flow} = 0.475$.

the medium Mach number follows the trend that exists for the highest Mach number and therefore suggests that the presence of compressibility effects are felt in this flow field too. The quantitative difference of the degree of compressibility effects between $M_{flow} = 0.6$ and $M_{flow} = 0.475$ flow fields can be estimated upon closer observation of the data shown in figures 17 and 20. For almost a 4-fold increase in the mesh size and Re_M the dissipation rate decreased 10 times for $M_{flow} = 0.6$ and approximately 5 times for the $M_{flow} = 0.475$ flow field. This behaviour also suggests that, as expected, higher Mach number flow fields introduce higher compressibility effects on dissipation.

The result of single measurement of total dissipation obtained with the multi-wire vorticity probe is also plotted in figure 20. The measurements were obtained in the flow with the $M = 12.7$ mm grid and with $M_{flow} = 0.425$ which is lower than the flow Mach number of the rest of the data. This value of dissipation rate is also slightly higher than the values obtained from the decay rate of turbulent kinetic energy.

The present measurements indicate that, in addition to the particular grid used to generate the flow and the Reynolds number Re_M, dissipation rate depends also on the flow Mach number M_{flow}. Following the same reasoning as in the previous section, the change in dissipation $\Delta\epsilon$ can be decomposed into the two contributions

$$\Delta\epsilon = [\partial\epsilon/\partial M_{flow}]\Delta M_{flow} + [\partial\epsilon/\partial Re_M]\Delta Re_M. \tag{13.1}$$

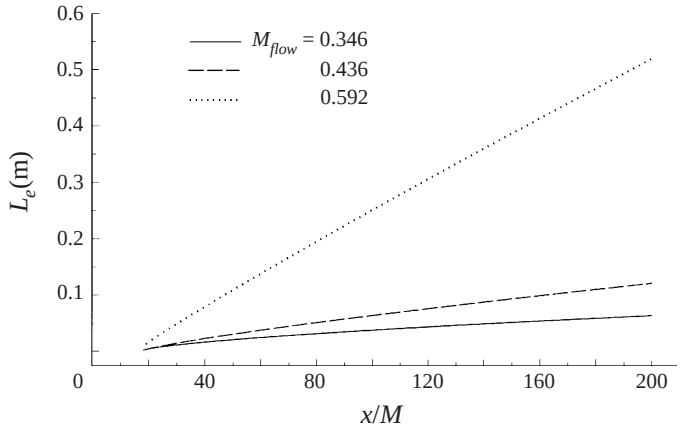

FIGURE 21. Dissipative length scale for three mean flow Mach numbers. $M = 12.7$.

The present experimental data show that the changes due to M_{flow} effects dominate the behaviour of (13.1). It appears that $\partial\epsilon/\partial M_{flow} < 0$ in the low M_{flow} range from 0.3 to 0.47 and $\partial\epsilon/\partial M_{flow} > 0$ in the high M_{flow} range from 0.47 to 0.6. The partial derivative is positive, $\partial\epsilon/\partial M_{flow} > 0$ at $M_{flow} = 0.3$ and $\partial\epsilon/\partial M_{flow} < 0$ at $M_{flow} = 0.47$ or higher. The data of figures 17, 18 and 19 verify this behaviour.

Similar considerations can be used to find the dependence of the dissipative length scale L_e on M_{flow} and Re_M. A summary of the present findings can be found in table 5 in § 15.

The dissipation length scale L_e indicates how fast the advected turbulent kinetic energy q^2, at a given location, is dissipated into heat. It is a longitudinal length scale since advection of q^2 in the present flow takes place only in the longitudinal direction. As Mach number increases the results of the present investigation show that the dissipative length scale L_e increases, although the dissipation rate of turbulent kinetic energy, ϵ, also increases for a given mesh size (see figure 16). This increase in L_e is attributed to the increase in q^2 with Mach number, which apparently is larger than the corresponding increase of ϵ.

A typical result is shown in figure 21. These data correspond to the three flow fields with different Mach numbers and are obtained with the same grid of mesh size $M = 12.7$ mm. It is interesting to observe that for the highest mean flow Mach number the dissipation length scale grows faster, and reaches values much greater, than the medium Mach number flow case. This behaviour can be attributed to higher compressibility and higher Re_M effects which can cause such a drastic increase. In the case of fine grids (not shown here), however, the trend observed is reversed: the dissipation length L_e decreases with increasing M_{flow}. For both grids, i.e. the 5×5 and the 4×4 with $M = 5.08$ mm and $M = 6.35$ mm respectively, L_e decreases with M_{flow}. The data indicate a fast dissipation process in flows produced by fine grids.

The effect of the grid mesh size on the dissipation length scale is shown in figure 22. The dissipation length scale L_e increases with increasing mesh size and Re_M. From this figure it can be seen that for the same mean Mach number a 5-fold or more increase in L_e occurs for a 3-fold increase in the mesh size/Re_M. Thus the pivotal effect that the grid size exerts on the length scales in the flow field is that coarser grids result in longer L_e. It is also apparent from both previous figures that the dissipation length scale strongly depends on x/M and that it increases with downstream distance.

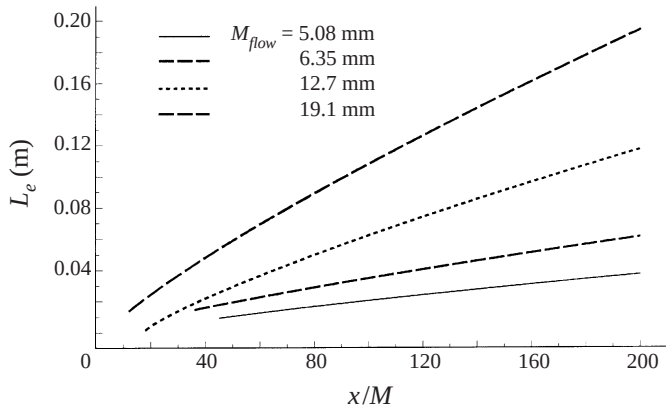

FIGURE 22. Dissipative length scale for several mesh sizes. $M_{flow} = 0.475$.

The data presented in figure 21 for the highest Mach number flow field shows large values of L_e which are indicative of a very slow dissipation process. These values exceed the shock tube diameter $D = 0.305\,\mathrm{m}$ at distances $x/M > 130$ and at about $x/M = 200$ reach values of $L_e = 0.5\,\mathrm{m} = 1.63D$. In general, it is expected that at large distances from the grid the growth of eddies due to amalgamation will be affected by the cross-sectional size of the facility which in the present case is described by the diameter D. This requires that at any point in the flow the *lateral* length scale L_{22} should be smaller than D. Since L_{22} is related to the mesh size of the grid M the above requirement introduces for consideration the parameter D/M, which has to be reasonably high in order to avoid these wall effects on the flow development. In this context, however, L_e represents a *longitudinal* length scale which characterizes the dissipative motions, which are mostly taking place at the level of small-scale eddies which are isotropic although, indirectly, they may be affected by the motion of the large eddies. Thus no direct effect of D is expected on L_e and therefore L_e can reach values of the order of D.

In order to estimate the length scales in the longitudinal ξ_1-direction and normal ξ_2-direction, the cross-correlation coefficients

$$r_{ij}(\xi_k) = \frac{\overline{u_i(x)u_j(x+\xi_k)}}{\sqrt{u_i^2(x)}\sqrt{u_j^2(x+\xi_k)}}$$

were evaluated by two-point measurement in the ξ_2-direction and from auto-correlations in the ξ_1-direction after invoking Taylor's hypothesis.

Figure 23 shows the $L_{11}(\xi_1)$ scale in the longitudinal direction for the three different flow cases. There exists some scatter in the data at each particular case which is attributed to the various grids used. No attempt has been made to present any Re_M effects since no clear trend or pattern among the data obtained could be identified. From the data of figure 23, it can be seen that the integral length scale increases with downstream non-dimensional distance x/M for all cases investigated. It is also evident that L_{11} in the case of $M_{flow} = 0.475$ is higher than in the case of $M_{flow} = 0.36$. However when the flow Mach number increases to $M_{flow} = 0.6$ and therefore stronger compressibility effects are present, then the values of the integral length scale drop.

The two-point correlation $r_{11}(\xi_2)$ in the lateral direction ξ_2 of the longitudinal velocity fluctuations is shown in figure 24. These data were obtained by a specially

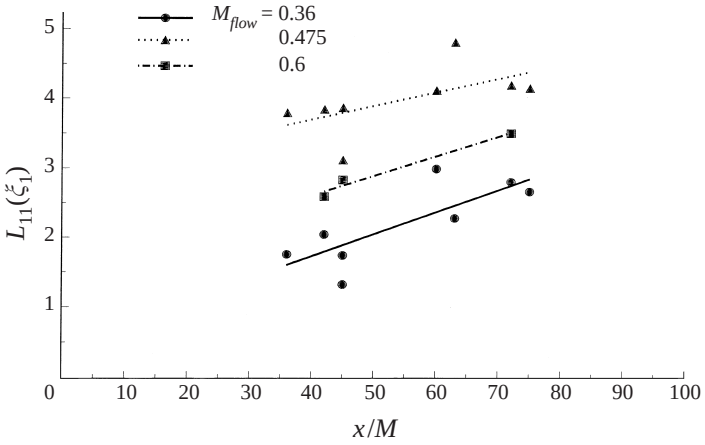

FIGURE 23. Longitudinal length scale for various experiments.

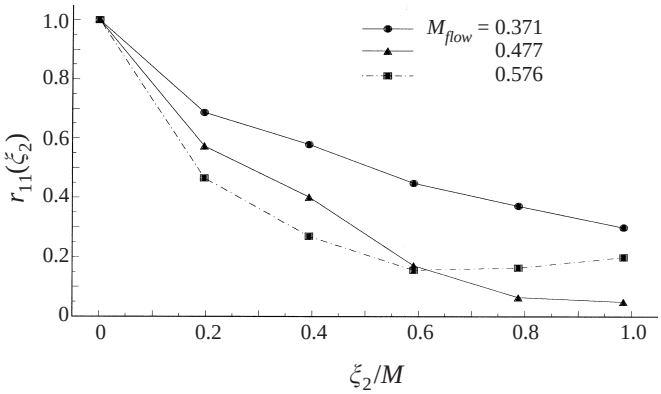

FIGURE 24. Space correlation in the lateral direction for three different flow cases. $x/M = 45$; 5×5 grid.

designed cross-correlation probe consisting of six parallel wires and three temperature wires separated from each other by 1 mm. Not all the curves cross the zero line and therefore it is very difficult to integrate them in order to obtain the classically defined length scale in the lateral direction. However-the slopes of these curves are indicative of their trend. It is rather obvious that the length scales are reduced with increasing flow Mach number. This behaviour is very similar to that of $L_{11}(\xi_1)$.

The effect of Mach number on Taylor's microscale computed from

$$\epsilon = 15\nu\overline{\left(\frac{\partial u}{\partial x}\right)^2} = 15\nu\frac{\overline{u^2}}{\lambda^2}$$

is shown in figure 25 for three different Mach numbers and for one grid with mesh size 12.7 mm. Taylor's microscale appears to increase with increasing Mach number. Increase of Taylor's microscale is also observed in flow fields produced by coarser grids. This is shown in figure 26 where the data from four different grids are plotted for the same flow Mach number. It is clear that the coarser the grid, i.e. larger mesh size, the greater Taylor's microscale. The dependence (increase) with increasing x/M, as shown earlier for the dissipation length scale, is also shown for Taylor's microscale.

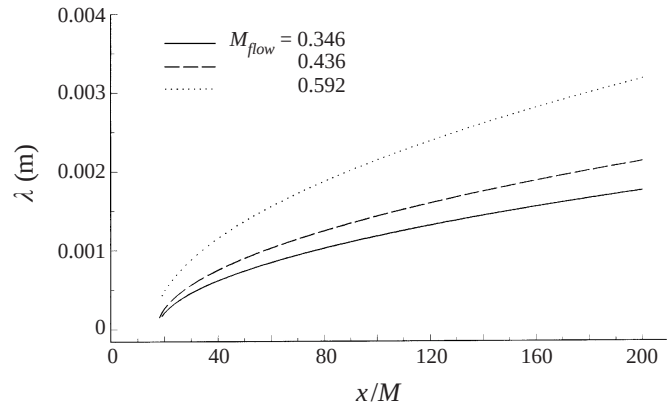

FIGURE 25. Taylor's microscale for three mean flow Mach numbers. $M = 12.7$ mm.

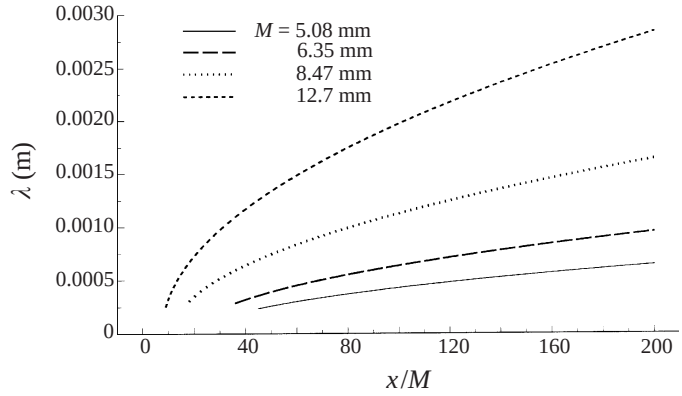

FIGURE 26. Taylor's microscale for several mesh sizes. $M_{flow} = 0.475$.

However, in the case of the grid with $M = 5.08$ mm, which is considered a fine grid, λ appears to decrease with M_{flow} (not shown here). This difference in the behaviour between the coarse and fine grids is a direct outcome of a similar behaviour in the dissipation distribution which was discussed earlier in reference to dissipation data shown in figures 16(*b*) and 16(*c*).

The effect of the flow Mach number on the viscous scales is investigated next. The data for three different Mach numbers are shown in figure 27 for the case of the 5×5 grid with mesh size 5.08 mm. They all increase with downstream distance. The results also show that as the Mach number increases, Kolmogorov's length scale, η decreases. This viscous scale appears to increase with increasing M_{flow} even in the case of coarse grids.

The effect of mesh size/Re_M on η is shown in figure 28 where the data are plotted for four different mesh sizes and for a decaying flow field at a constant mean Mach number of 0.6. Similar results are obtained for the rest of the flow fields tested. It appears that η increases with increasing M or Re_M, a behaviour which is similar to that of λ or L_e.

The last two figures (27 and 28) demonstrate the effects of compressibility on the viscous scales. In particular, compressibility effects appear to reduce their size. This behaviour imposes a severe requirement for spatial resolution in high Mach number

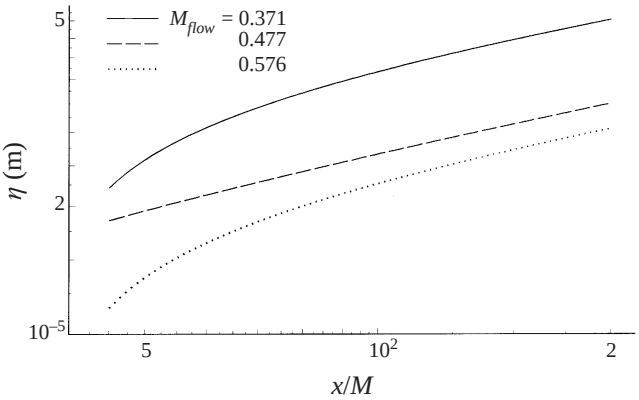

FIGURE 27. Kolmogorov's length scale for three mean flow Mach numbers. $M = 5.08$ mm.

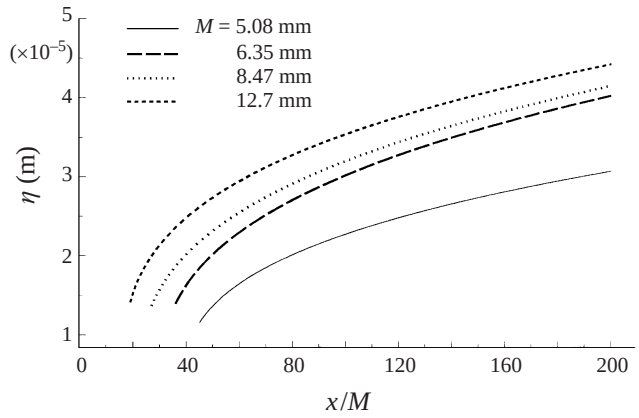

FIGURE 28. Kolmogorov's length scale for various mesh sizes. $M_{flow} = 0.6$.

turbulent flows. The present measurements indicate values of η ranging from 0.015 to 0.06 mm. The size of the probes, l_w, expressed in terms of Kolmogorov's length scales appears to be $\eta_w = l_w/\eta = 13$ for the greatest scales and 52 for the smallest scales. The scales at error start at about half of these values, 7 and 26 respectively. Based on these values, which determine the upper limit of the valid part of the spectrum, estimates of the power spectral density of the spatially filtered scales have been obtained from Wyngaard's (1969) work for subsonic flows. It appears that the spatially filtered scales amount to about 15% of the total spectral density of velocity fluctuations for measurements close to the grid where η is small and less than 4% for measurements where η is larger. The high resolution of the hot-wire probes allows us to conclude that the results obtained in regard to the compressibility effects on the viscous scales are not biased. In addition, the estimates of dissipation obtained from the decay rate of q^2 seem to be much less affected by the effects of inadequate spatial resolution than those obtained from spectra. One explanation of this immunity of ϵ to spatial resolution errors is a possible cancellation of uncertainties in the measurements of q^2 when the longitudinal gradient $\partial q^2/\partial x$ is computed. Thus the uncertainty in the estimates of η may be considerably lower than the 4% to 15% range quoted above.

In summary, the results of the present investigation indicate that dissipation rate,

No.	Grid	x/M	M_{flow}	$U_1(\mathrm{m\,s^{-1}})$	$\rho(\mathrm{kg\,m^{-3}})$	P (KPa)
1	2×2	48	0.308	121	1.59	155
2	2×2	48	0.388	151	1.74	174
3	3×3	72	0.362	139	1.7	170
4	3×3	72	0.425	161	1.84	188

TABLE 4. Bulk flow parameters for in vorticity measurements.

dissipation length scale and Taylor's microscale are strongly affected by the flow Mach number M_{flow}. In flows produced by fine grids dissipation increases with increasing M_{flow} while L_e and λ are reduced. In the case of flows generated by coarse grids, dissipation decreases with increasing M_{flow} and L_e and λ increase with M_{flow}. Lateral integral length scales and viscous length scales are reduced with increasing M_{flow}. This work also demonstrates that for high Mach numbers flows, all length scales, i.e. L_e, λ and η, increase with increasing mesh size or Re_M.

14. Vorticity and enstrophy

Four additional experiments were carried out with the new multi-wire vorticity probe. Table 4 shows the bulk flow parameters of the experiments, which were performed at two different flow Mach numbers and with two different grids.

Figures 29(*a*) and 29(*b*) show the power spectral density of the turbulent kinetic energy (TKE) $\frac{1}{2}u_iu_i$ and enstrophy $\frac{1}{2}\omega_i\omega_i$ weighted by the wavenumber $k_1 = 2\pi/\lambda$ as measured in the present investigation for the case of the 2×2 grid. The streamwise wavenumber $k_1 = 2\pi f/U_1$ was computed by assuming the local longitudinal mean velocity as the convection velocity (Taylor's hypothesis). Wavenumbers have been non-dimensionalized by the mesh size M. In the case of $M_{flow} = 0.308$ which is shown in figure 29, the maximum value of the spectral density of turbulent kinetic energy occurs at approximately $k_1M = 4.5$ while the maximum value of the spectral density of enstrophy occurs at about $k_1M = 7$. This difference in the maxima of spectral energies indicates a shift towards higher wavenumbers of enstrophy fluctuations, which suggests that they are mainly a result of a greater proportion of contributions by the smaller scales whereas the kinetic energy contains contributions from relatively larger eddies.

In the case of $M_{flow} = 0.388$, shown in figure 30, the maximum energy of TKE is found to occur at about the same wavenumber as in the case of $M_{flow} = 0.308$ i.e. at $k_1M = 4.5$, while the maximum energy of enstrophy occurs at a lower wavenumber $k_1M = 5.8$. Once more, the data show that there is a shift towards higher wavenumbers in the case of enstrophy maxima. However, it appears that increasing M_{flow} reduces the difference between the wavenumbers where the maxima of kinetic energy and enstrophy occur. If one considers that the peak in TKE represents the size of large-energy-containing eddies and that the peak in enstrophy represents mostly small energy dissipating eddies then it would be expected that this difference or shift increases with increasing Reynolds number. The fact that this shift decreases with Mach number in the present case indicates that the effect of M_{flow} in reducing this difference becomes stronger than the effect of Reynolds number in increasing it.

Similar observations can be made in the case of the 3×3 grid for the two experiments carried out with this grid. Figures 29(*c*) and 29(*d*) show the spectral

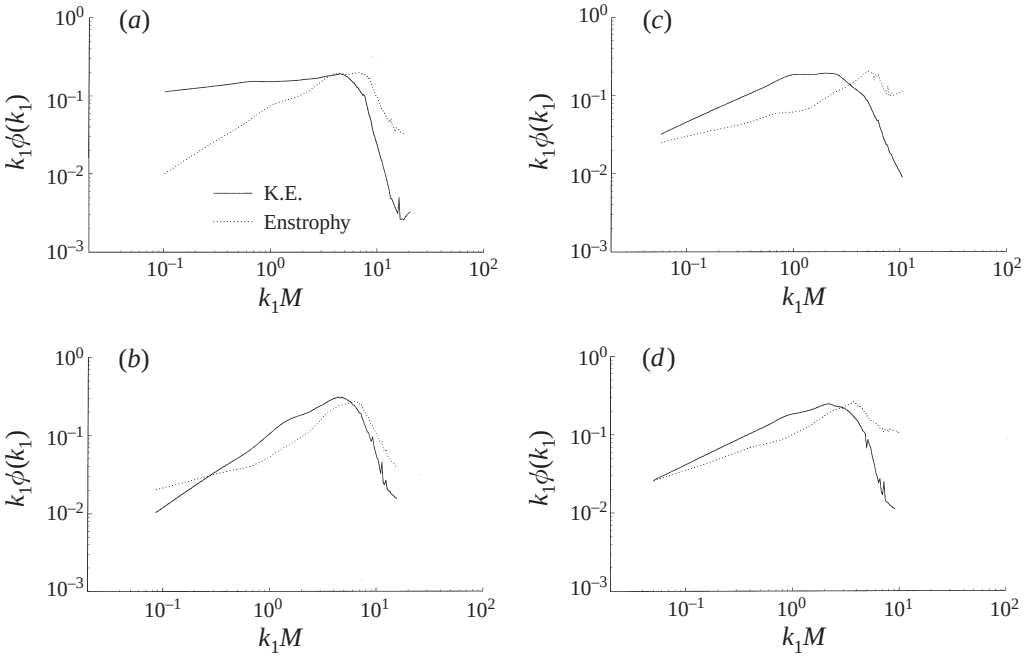

FIGURE 29. Weighted power spectral densities for turbulent kinetic energy and enstrophy: (*a*) $M_{flow} = 0.308$, $M = 12.7$ mm; (*b*) $M_{flow} = 0.388$, $M = 12.7$ mm; (*c*) $M_{flow} = 0.362$, $M = 18.4$ mm; (*d*) $M_{flow} = 0.425$, $M = 8.4$ mm.

densities of TKE and enstrophy for the $M_{flow} = 0.362$ and 0.425 cases respectively. The maximum spectral density of TKE occurs at about $k_1M = 2$ in both flows. However, the maximum spectral density of enstrophy occurs at $k_1M = 5.6$ in the case of $M_{flow} = 0.362$ and at $k_1M = 3.8$ in the case of $M_{flow} = 0.425$. Thus the initial wavenumber difference of 3.6 observed in the lower Mach number case is reduced by about 50% in the case of $M_{flow} = 0.425$.

Figure 30(*a*) shows a semi-logarithmic plot of the probability density function (p.d.f.) of the three vorticity components for the case of $M = 12.7$ mm and $M_{flow} = 0.308$. The quantity M/U_1 has been used to non-dimensionalize vorticity. The data show that the p.d.f.s of the vorticity components overlap substantially, as is expected to occur under isotropic conditions. The present data also indicate that these p.d.f.s have a Gaussian distribution. As the flow Mach number increases to $M_{flow} = 0.388$ the p.d.f.s of vorticity start to deviate from the Gaussian distribution (see figure 30*b*). The data show that the three p.d.f.s collapse quite well on each other indicating a good degree of isotropy. However, the probability of higher amplitudes which are characterized by the tails of the distributions are lower than the probability predicted by the Gaussian distribution. This is the first evidence that compressibility starts to affect the high-amplitude events of vorticity first.

Similar behaviour can be seen in the p.d.f.s of vorticity components for the case of $M = 8.47$ mm. These p.d.f.s are plotted in figures 30(*c*) and 30(*d*) for the flow cases with $M_{flow} = 0.362$ and 0.462 respectively. Both figures indicate a good degree of isotropy of the vorticity field. In the higher M_{flow} case, as in the case with the $M = 12.7$ mm grid, the tails of the distributions start to deviate from the Gaussian distribution, indicating the effect of compressibility.

The p.d.f.s of the enstrophy $\omega_k\omega_k$ for the two cases of experiments with the two

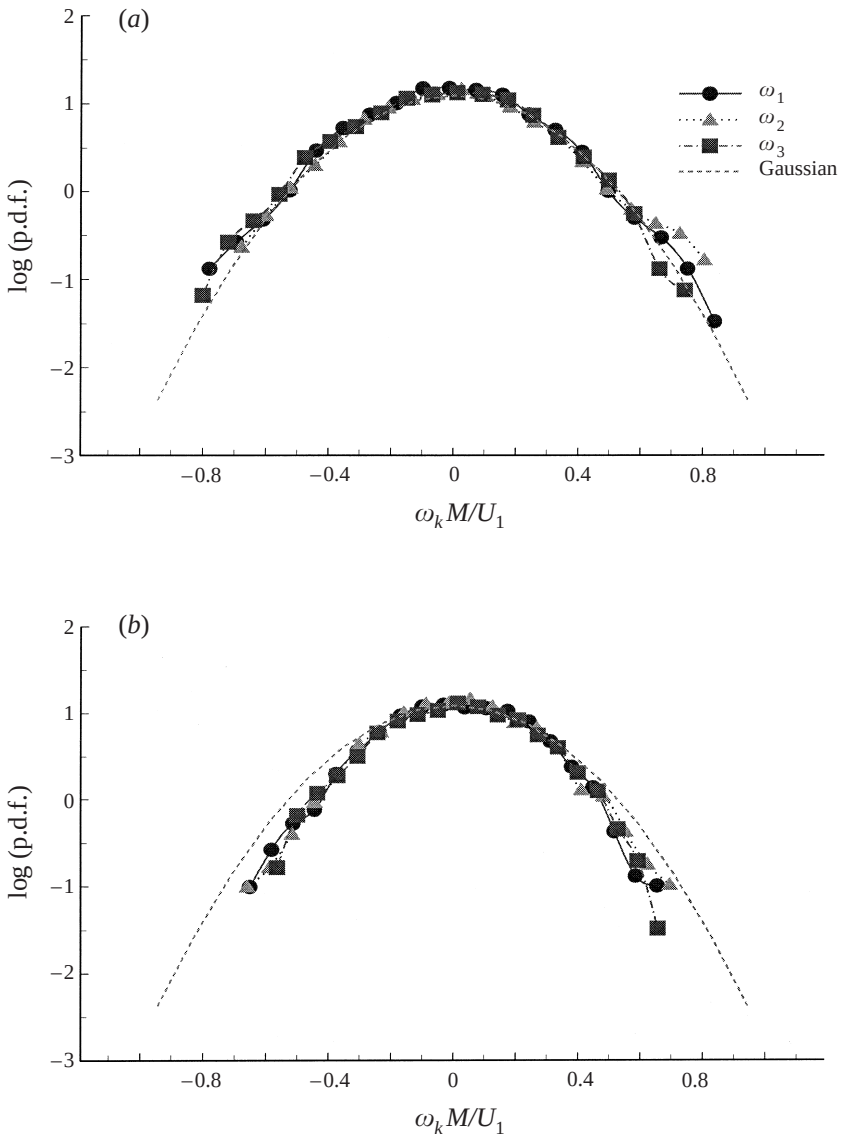

FIGURE 30 (*a*, *b*). For caption see page 268.

different grids, $M = 12.7\,\text{mm}$ (2×2) and $M = 8.46\,\text{mm}$ (3×3), are shown in figure 31. Enstrophy values have been non-dimensionalized by $(M/U_1)^2$. Enstrophy is a very significant quantity in fluid dynamics. It is not only related to the solenoidal dissipation, as was mentioned in § 6, but also to the invariants of the rate-of-strain matrix s_{ij}. In addition, enstrophy is a source term in the transport equation of dilatation s_{kk}:

$$\frac{\mathrm{D}(s_{kk})}{\mathrm{D}t} = -s_{ik}s_{ki} + \tfrac{1}{2}\omega_k\omega_k + \frac{1}{\rho^2}\frac{\partial\rho}{\partial x_k}\frac{\partial p}{\partial x_k} - \frac{1}{\rho}\frac{\partial^2 p}{\partial x_k \partial x_k} + \frac{\partial}{\partial x_k}\frac{1}{\rho}\frac{\partial \tau_{kq}}{\partial x_q}. \tag{14.1}$$

This transport equation shows the change of dilatation along a particle path, which can be caused by the straining action of the dissipative motions ($s_{ik}s_{ik}$) as well as by the

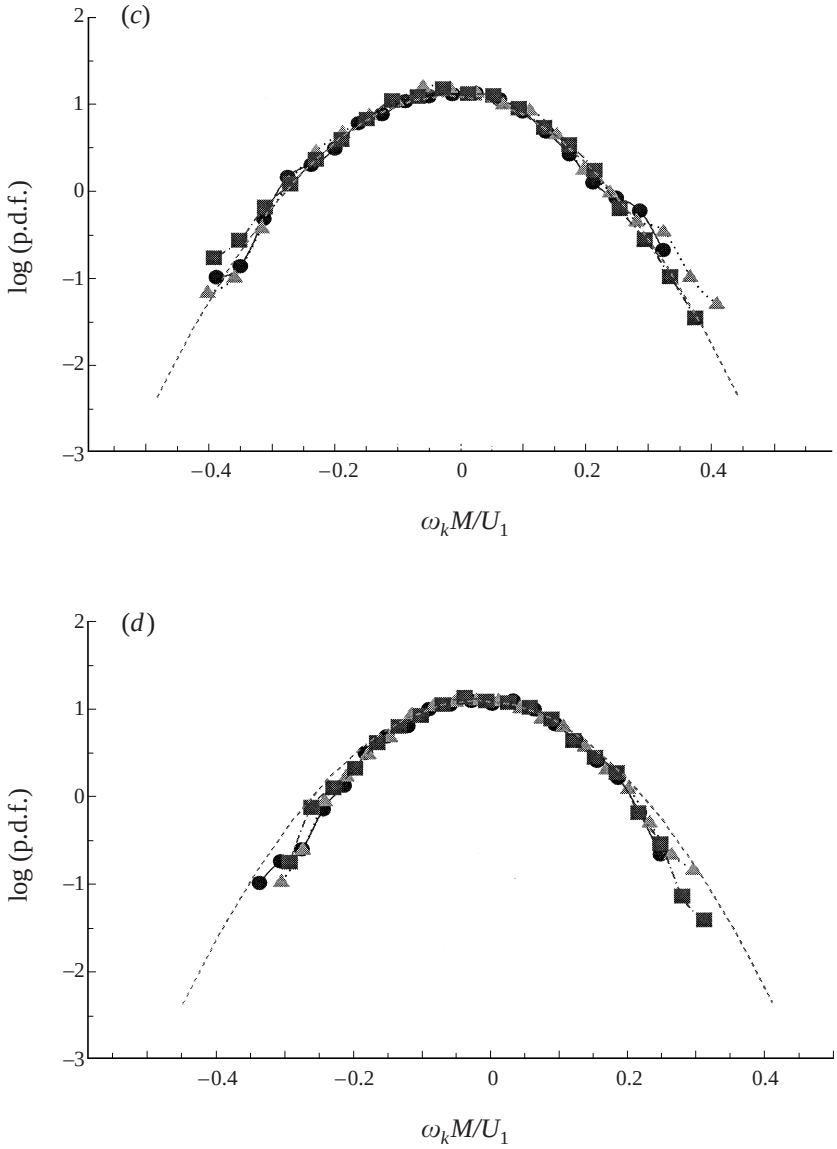

FIGURE 30. Probability distributions of vorticity components; (*a*) $M_{flow} = 0.308$, $M = 12.7$ mm; (*b*) $M_{flow} = 0.388$, $M = 12.7$ mm; (*c*) $M_{flow} = 0.362$, $M = 8.4$ mm; (*d*) $M_{flow} = 0.425$, $M = 8.4$ mm.

rotational energy of the spinning motions as expressed by the enstrophy $(1/2)\omega_k\omega_k$. Pressure and density gradients as well as viscous diffusion can also affect dilatation. It should be noted that the above transport equation reduces to the well-known Poisson equation

$$\frac{1}{\rho}\frac{\partial^2 p}{\partial x_k \partial x_k} = -s_{ik}s_{ki} + \tfrac{1}{2}\omega_k\omega_k \tag{14.2}$$

for incompressible flows of constant density ($s_{kk} = 0$).

The distribution of the p.d.f.s shown in figure 31 indicates that most of the data i.e. data with high frequency of occurrence are mainly associated with low-

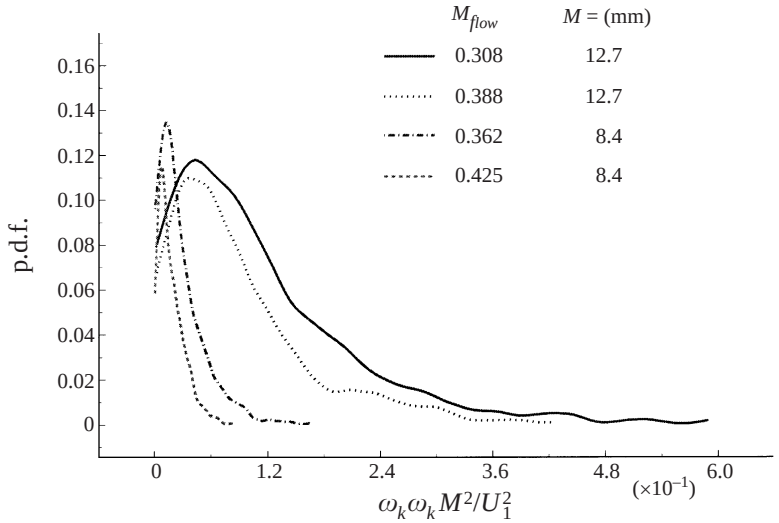

FIGURE 31. Probability distributions of enstrophy.

amplitude fluctuations of enstrophy. However, it appears that there exist rare events, i.e. events with low probability of occurrence, which have extremely high amplitude of enstrophy and which may be of significant importance in the dynamics of the fluid. This behaviour, observed in all experiments, is indicative of highly fluctuating quantities.

Since the distributions shown in figure 31 are not normalized, the area under each them is indicative of the mean value of enstrophy. The data show that enstrophy decreases with increasing M_{flow}. In the case of the 2×2 grid with $M = 12.7$ mm, for instance, the mean value of enstrophy reduces by 25% when the flow Mach number increases by about 25%. In the case of the 3×3 grid enstrophy is decreased by 50% when the Mach number increases by 17%. Thus it appears that the effect of compressibility is to reduce enstrophy fluctuations. Even in the present cases of rather weakly compressible flows the effects on enstrophy are rather substantial.

It is very interesting to compare the effects of compressibility on velocity fluctuations with those on enstrophy fluctuations. Velocity fluctuations increase with increasing M_{flow} while enstrophy fluctuations decrease. Are these two results incompatible? The answer is no, if one considers that enstrophy varies as u^2/λ^2 or better in non-dimensional terms as $(u/U)^2(M/\lambda)^2$. It appears that $(\lambda/M)^2$ increases substantially faster with M_{flow} than $(u/U)^2$, confirmed by the present data. In addition, the variation of dissipation rate with the flow Mach number is exactly the same as that of enstrophy. Thus the conclusion that compressibility decreases enstrophy fluctuations and increases velocity fluctuations, appears to be genuine.

Figure 32 shows distributions of the p.d.f.s of the dilatation $(1/\rho)\mathrm{D}\rho/\mathrm{D}t = -s_{kk}$ as measured in the four different experiments of the present investigation. Values are non-dimensionalized by M/U_1. The mean value of dilatation in this homogeneous flow is expected to be zero and the experimental data confirm it. The level of dilatation fluctuations is about 1/8 to 1/20 of the level of vorticity fluctuations. A comparison of the level of dilatational fluctuations with the range of vorticity fluctuations as depicted from the p.d.f.s shown in figures 30 and 32 indicates that the former are about 5% to 7.5% of the latter in the case of the 2×2 grid ($M = 12.7$ mm) depending on M_{flow}, and

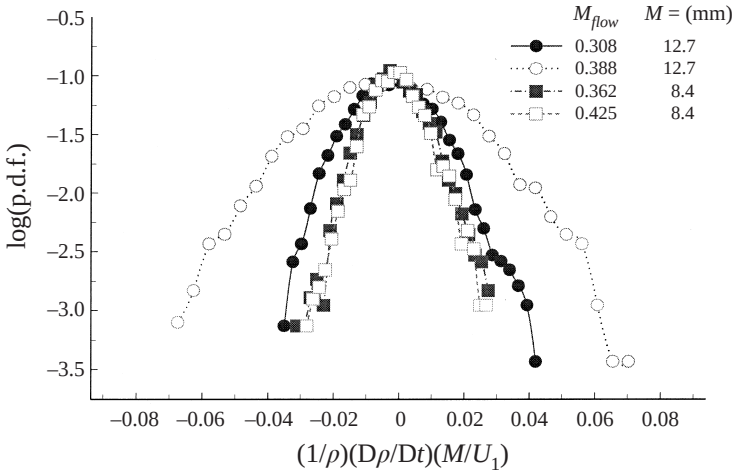

FIGURE 32. Probability distributions of dilation rate.

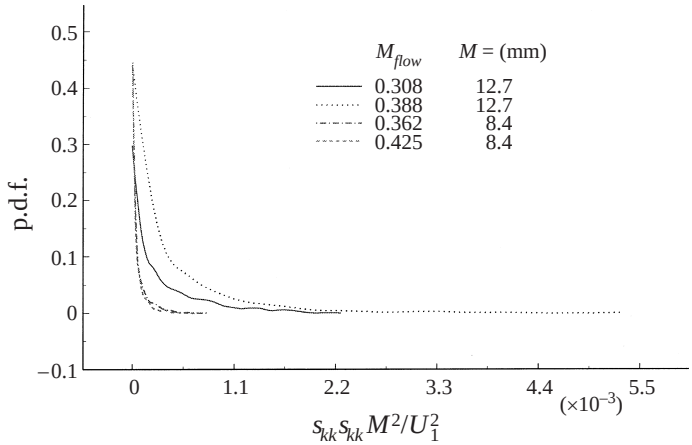

FIGURE 33. Probability distributions of compressible dissipation.

13% in the case of the 3×3 grid ($M = 8.4$ mm). These values are typical of weakly compressible turbulence with rather low fluctuations of Mach number (turbulent Mach number). Nevertheless compressibility effects are detectable. For instance, the data of figure 32 in the case of the 2×2 grid clearly show that dilatational fluctuations increase considerably with M_{flow}, while vorticity and enstrophy fluctuations decrease.

In the case of the 3×3 grid no substantial differences between the flows with two different Mach numbers could be detected. However, this may be an effect of the way dilatation is non-dimensionalized by M/U_1 since dimensionalized values of $(1/\rho)\mathrm{D}\rho/\mathrm{D}t$ fluctuations are about 20% higher in the case of the $M_{flow} = 0.425$ than those in the lower $M_{flow} = 0.388$ case.

Distribution of p.d.f.s of the non-dimensionalized quantity $s_{kk}s_{kk}(M/U_1)^2$ which represents the dilatational part of dissipation are shown in figure 33. This term in the present case of rather weakly compressible turbulence is about 50 to 100 times smaller than the corresponding solenoidal dissipation. In that sense its direct effect on turbulence may not be significant. Nevertheless it is important to understand how it

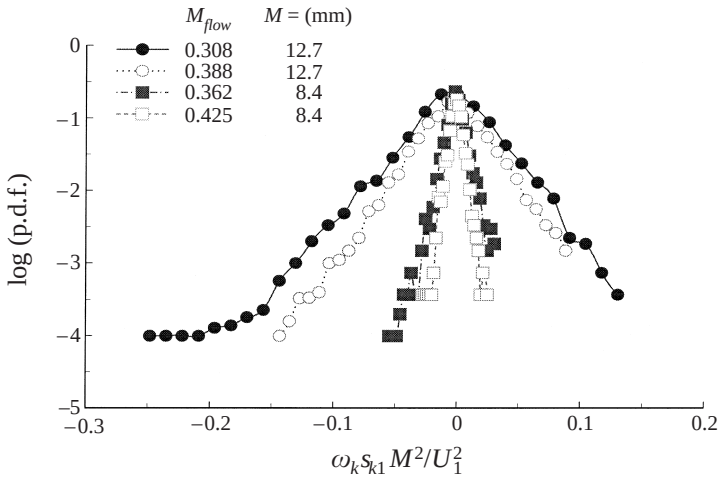

FIGURE 34. Probability distributions of stretching component $\omega_k s_{kl}$.

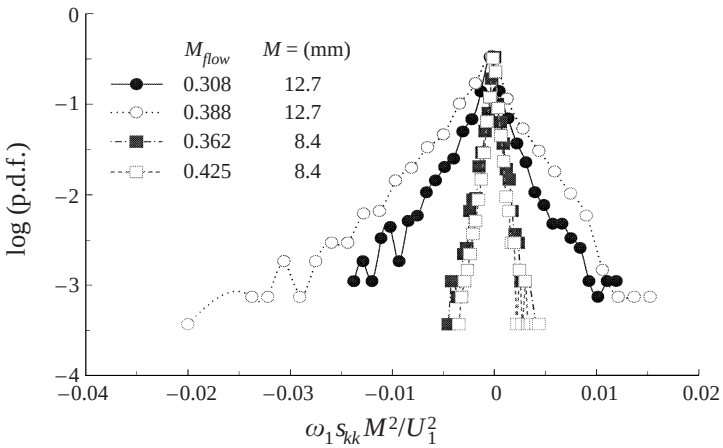

FIGURE 35. Probability distributions of compressible stretching component $\omega_l s_{kk}$.

changes with Mach number. In the case of the 2×2 grid ($M = 12.7$ mm) compressible dissipation increases with M_{flow} while solenoidal dissipation decreases. The data also show that rare events with stronger amplitudes are present in the $M_{flow} = 0.425$ case than in the $M_{flow} = 0.388$ case.

No differences in the distributions of compressible dissipation between the two flows could be discerned in the case of the 3×3 grid. However, this effect can be attributed to the non-dimensionalizing parameter $(M/U_1)^2$ because the raw, dimensionalized data indicated a 50% increase in the values of compressible dissipation.

The transport equation of vorticity

$$\frac{\mathrm{D}\omega_i}{\mathrm{D}t} = s_{ik}\omega_k - \omega_i s_{kk} + \epsilon_{iq\eta}\frac{1}{\rho^2}\frac{\partial \rho}{\partial x_q}\frac{\partial p}{\partial x_\eta} + \epsilon_{iq\eta}\frac{\partial}{\partial x_q}\left(\frac{1}{\rho}\frac{\partial \tau_{\eta j}}{\partial x_j}\right) \tag{14.3}$$

describes four dynamically significant processes for the vorticity vector $\boldsymbol{\omega}$, namely stretching or compression and tilting by the strain s_{ik}, vorticity generation through

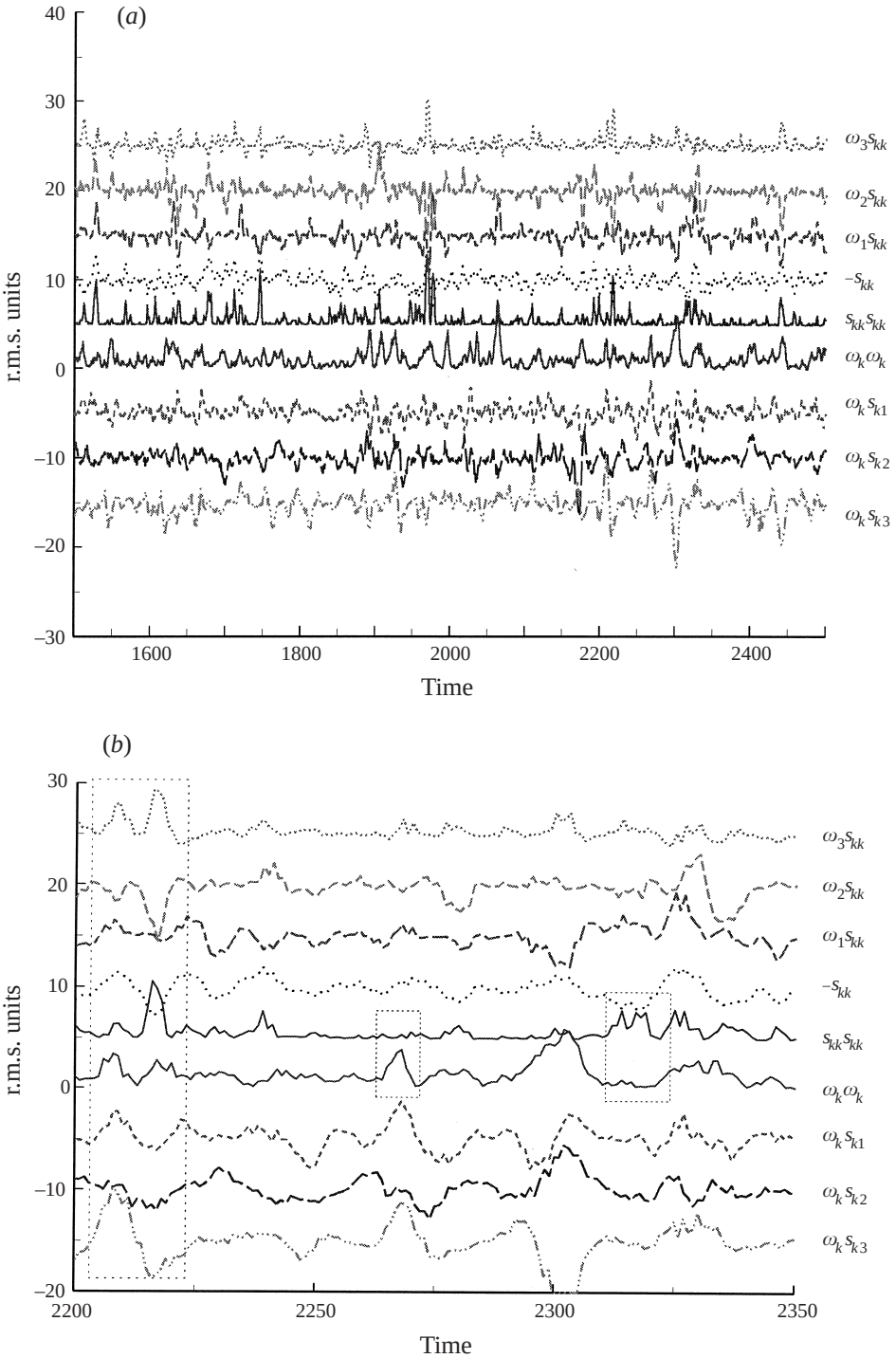

FIGURE 36. Typical signals of various quantities normalized by their r.m.s. value. (Actual signals are displayed.) $M_{flow} = 0.308$, $M = 12.7$ mm.

dilatation, baroclinic generation through the interaction of pressure and density gradients and viscous diffusion. In the present work the first two terms have been evaluated directly. The baroclinic term could not be measured but order of magnitude analysis showed that it is rather small in the present flow. If the viscous term can be also ignored since its magnitude is also small, then the change of vorticity of a fluid element in a Lagrangian frame of reference can be entirely attributed to vortex stretching and/or tilting and to dilatational effects.

Figure 34 shows distributions of the p.d.f.s of the longitudinal component of the stretching vector $s_{1k}\omega_k$ for the four experiments carried out in the present investigation. Values are non-dimensionalized by $(M/U_1)^2$ and plotted in semi-logarithmic scale. A typical characteristic of all distributions is their long tails which are indicative of strong but rare events with substantial contribution to the stretching process. The data also show that stretching fluctuations decrease with increasing M_{flow}. In both experiments with the two different grids, mean and fluctuating stretching appears to be lower in the cases of high M_{flow} than in the cases of low M_{flow}. This behaviour is not surprising because vorticity is reduced with increasing flow Mach number and therefore source terms are expected also to decrease. However the dilatational generation of vorticity is affected by the flow Mach number in the opposite way. Figure 35 shows the distributions of the p.d.f.s of $\omega_1 s_{kk}$ which describes the generation of vorticity by the expansion or compression of the rate of change of the specific volume since $-(1/\rho)(\mathrm{D}\rho/\mathrm{D}t) = (1/V)(\mathrm{D}V/\mathrm{D}t) = s_{kk}$. In the case of the 2×2 grid ($M = 12.7$ mm), a substantial increase in the level of fluctuations can be observed when the flow Mach number increases. This indicates that dilatational fluctuations, which increase with increase in M_{flow}, dominate over vorticity fluctuations which are reduced with increased M_{flow}. Since dilatational stretching $\omega_1 s_{kk}$ enters equation (14.3) with opposite sign to $s_{1k}\omega_k$, the net effect is that the quantity $s_{1k}\omega_k - \omega_1 s_{kk}$ decreases with increasing M_{flow}. Thus vorticity fluctuations are expected to decrease with increasing Mach number.

No substantial differences can be observed between the two distributions in the case of the 3×3 grid ($M = 8.4$ mm). This again can be attributed to the way the data are made non-dimensional, since the raw dimensionalized data show that compressibility increases the fluctuations of $\omega_1 s_{kk}$. The long tails of the distributions also suggest that rare but violent events are substantially affecting these processes.

Some further insight of the dynamical processes involved in these flows can be gained by looking at the instantaneous signals of the various quantities present in the transport equations mentioned above. Figure 36(*a*) shows signals of dissipation $\omega_k\omega_k$, dilatational dissipation $s_{kk}s_{kk}$, the three components of the vorticity stretching vector $s_{1k}\omega_k, s_{2k}\omega_k, s_{3k}\omega_k$, and the three components of the dilational stretching vector $\omega_1 s_{kk}$, $\omega_2 s_{kk}$, $\omega_3 s_{kk}$. Each signal has been normalized by its r.m.s. and has been displaced by a multiple of 5 r.m.s. units for better visual aid. All signals exhibit a rather strong intermittent behaviour which is characterized by bursts of high-amplitude events, which sometimes reach values up to 5 to 8 r.m.s. units, followed by less violent periods. Several of these bursts are evident in all signals, suggesting the existence of a dynamical flow phenomenon which may be the common cause.

It is also interesting to observe that the correlation between any two of these signals seems to be higher during any of the those violent events. In general there is some statistical correlation in several of the signals. For instance, a correlation coefficient of about ± 0.04 has been obtained between enstrophy and any of the vorticity stretching components. During violent events which involved substantial vorticity stretching or compressing activities, this coefficient can be 2 to 5 times higher.

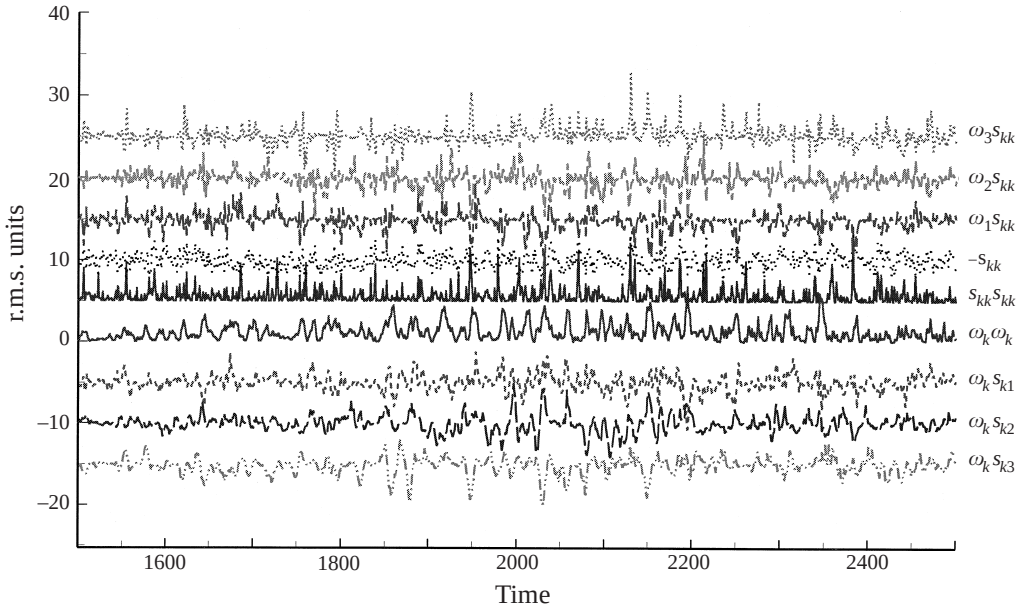

FIGURE 37. Typical signals; $M_{flow} = 0.388$, $M = 12.7$ mm.

A comparison between $\omega_k \omega_k$ and $s_{kk} s_{kk}$ shows that there is some correlation between them since some bursts can be observed on both signals. However there are same strong events on one signal without a corresponding event on the other. Figure 36(*b*) shows a portion of the previously signals expanded in time, with annotated boxes where several of the previous discussed characteristics and features are highlighted. The first box, centred at about time = 2212, for instance, shows strong events which can be identified on all signals. The second box at about time = 2260 shows an event detectable on $\omega_k \omega_k$ but not on $s_{kk} s_{kk}$. The third box at about time = 2330 shows an event on $s_{kk} s_{kk}$ without a corresponding counterpart on $\omega_k \omega_k$. The signals also indicate that the duration of the strong events on $s_{kk} s_{kk}$ is considerably shorter than the events identified on the $\omega_k \omega_k$ signal.

The signals obtained in the experiment with $M_{flow} = 0.388$ and grid of $M = 12.7$ mm are shown in figure 37. They exhibit similar characteristics to the signals of figure 36. However the amplitude and the frequency of these bursting events appear to be higher while their duration is shorter than in the experiment with the lower Mach number.

15. Conclusions

The effects of compressibility in a nearly homogeneous and nearly isotropic flow of decaying turbulence have been investigated experimentally by carrying out high-resolution measurements in a large-scale shock tube research facility. A variety of grids of rectangular pattern of different mesh size was used to generate the flow field. The Reynolds number of the flow based on the mesh size, Re_M, ranged from 50 000 to 400 000, while the turbulent Reynolds number Re_λ based on Taylor's microscale λ was between 200 and 700, which constitutes one of the highest scales ever achieved in laboratory flow. The range of Mach number of the flows investigated was between 0.3 and 0.6 which was low enough to assure a shock-free flow and high enough to contain compressibility effects.

The effects of compressibility can be classified into two categories. The first category includes those effects which have a direct impact on the flow. Compressible dissipation, for instance, is a typical example of a quantity which expresses a direct effect of compressibility on total dissipation. The indirect effects comprise the second category, which include those which change the local or global behaviour of the flow and therefore may cause significant changes of the incompressible part of the flow. Increasing the Mach number of the flow, for instance, can change the level of turbulent fluctuations in the flow which may subsequently affect the dissipation rate, particularly the incompressible part which accounts for most of the total dissipation in cases like the present subsonic flow. Direct effects of compressibility on turbulence may be described by the turbulent Mach number M_t, while indirect effects on turbulence may be characterized by the flow Mach number M_{flow}, and the Reynolds number Re_M. The parameters M_t, M_{flow} and Re_M, however, are not completely independent from each other. A change in any of the three may cause a change in the other two. In that respect, the effects which each of the nominally independent variables impose on the flow may be difficult to distinguish. An attempt has been made here to identify the effects of M_{flow} and Re_M on homogeneous and isotropic turbulence.

The isotropy of the present flow was verified experimentally and it was found to be within the range reported for incompressible flows. In fact, it was established for the first time that isotropic compressible turbulence at moderate subsonic Mach numbers can be set up experimentally. The decay of Mach number fluctuations was found to follow a power-law behaviour similar to that describing the decay of incompressible isotropic turbulence

$$M_t^2 = B\left[\frac{x}{M} - \left(\frac{x}{M}\right)_0\right]^{-n},$$

where $B, (x/M)_0$ and n are constants depending on the flow Mach number as well as on Re_M and the grid. These constants have been determined concurrently so that the residual deviation from the original data is minimized. This approach represents a departure from previous practices where one of the three parameters was fixed and the other two were determined through a best fit of the data. In that context, direct comparison of the present data with previously obtained values of any of the three constants may not be feasible. A direct consequence of the procedure followed in this investigation may be that the exponent n has been found to reach values below 1, which indicates, in principle, a slower decay rate than that found in many previous cases under the assumption that one of the three unknown constants should be fixed.

In the present work, it was possible to investigate the effects of the Mach number and Re_M on the flow development independently from each other. The virtual origin tends to a reasonably constant value of 4.5 at high Re_M which is independent of the flow Mach number. The decay coefficient B and the decay exponent n decrease with increasing Mach number while the virtual origin $(x/M)_0$ increases with increasing Mach number at a fixed Re_M.

Most probably the mechanism responsible for this effect is the inherently slow growth rate of compressible shear layers emanating from the cylindrical rods of the grid. Figure 38(*a*) shows a typical merging of shear layers to form an isotropic flow in the case of incompressible flows. The case of compressible shear layers is depicted in figure 38(*b*) where it is shown how a lower growth rate can result in a longer virtual origin. If a shock wave had been formed in the vicinity of the grid as in the case of Zwart *et al.* (1997) the decay rate would have been drastically affected. Shock waves or shocklets are not likely to appear at the present Mach numbers and therefore it

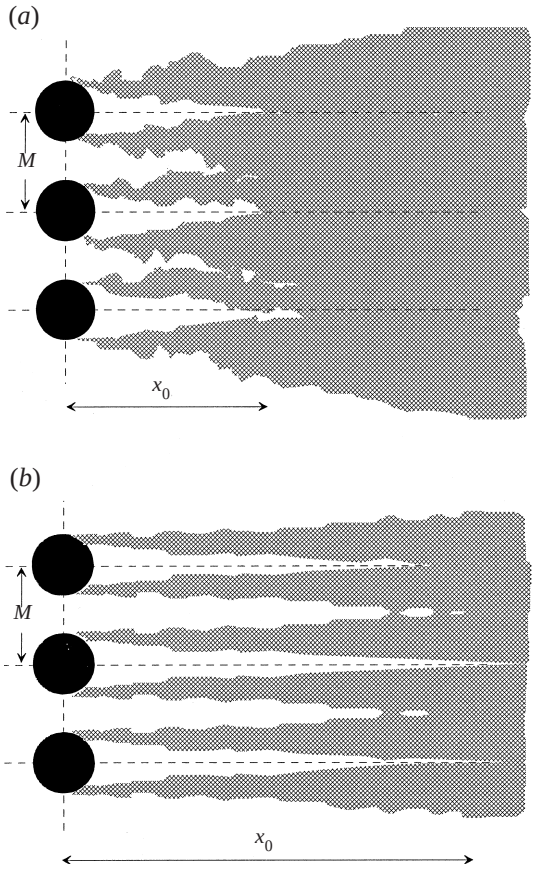

FIGURE 38. (*a*) Incompressible and (*b*) compressible shear layer growth.

is plausible to attribute the present results to the lower growth rate of compressible shear layers.

The dissipation rate of turbulent kinetic energy was found to increase with increasing flow Mach number for fine grids and decrease with increasing M_{flow} for coarse grids. As a result L_e and λ follow a similar pattern.

All longitudinal length scales increase with increasing M_{flow} while lateral integral length scales and viscous length scales are reduced with increasing M_{flow}. This work also demonstrated that in high Mach numbers flows, all length scales, i.e. L_e, λ and η, increase with increasing mesh size or Re_M.

An attempt has also been made to measure all time-dependent velocity gradients involved in vorticity, its stretching, enstrophy and dissipation rates, with adequate spatial and temporal resolution. This allowed estimates of dilatation s_{kk}, compressible dissipation s_{kk}^2 and compressible stretching $\omega_i s_{kk}$ to be obtained. These quantities are directly associated with compressibility effects. A common feature of all these quantities is that their fluctuations, properly normalized by M and U_1, increase with increasing Mach number of the flow. Although this behaviour may be expected, if one considers that in compressible shear layers increasing M_{flow} suppresses turbulent fluctuations then this conclusion is surprising.

The results of the present investigation have also shown that enstrophy fluctuations, which comprise the solenoidal part of dissipation, reduce with increasing M_{flow}, a

	Increasing M_{flow}	Increasing Re_M/M
A	$\Downarrow$	$\Updownarrow$
$(x/M)_0$	$\Uparrow$	$\Downarrow$
n	$\Downarrow$	$\Updownarrow$
u	$\Uparrow$	$\Updownarrow$
M_t	$\Uparrow$	$\Updownarrow$
ϵ	$\Uparrow$ Fine grids;	$\Updownarrow$
	$\Downarrow$ Coarse grids	
$\epsilon M/U^3$	$\Uparrow$ Fine grids;	$\Updownarrow$
	$\Downarrow$ Coarse grids	
L_e	$\Uparrow$ Coarse grids;	$\Uparrow$
	$\Downarrow$ Fine grids	
λ	$\Uparrow$ Coarse grids;	$\Uparrow$
	$\Downarrow$ Fine grids	
η	$\Downarrow$	$\Uparrow$
$L_{11}(\xi_1)$	$\Updownarrow$	$\Downarrow$
$L_{11}(\xi_2)$	$\Downarrow$	$\Updownarrow$
$s'_{kk}M/U^3$	$\Uparrow$	
$s^2_{kk}M/U^3$	$\Uparrow$	
$\omega_i s'_{kk}M/U^3$	$\Uparrow$	

TABLE 5. Summary of conclusions for the decaying isotropic flow field: $\Uparrow$ represents that the parameter increases with increasing M_{flow} or increasing mesh size/Re_M; $\Downarrow$ that it decreases; and $\Updownarrow$ that it presents no specific trend.

conclusion which is also verified by the results of dissipation obtained through the decay rate of turbulent kinetic energy for the case of coarse grids. The present data also indicate that the fundamental reason for the reduced turbulent fluctuations with increasing flow Mach number is the reduction in the stretching activities at higher Mach numbers.

The time-dependent signals of enstrophy $\omega_k\omega_k$, dilatation s_{kk}, compressible dissipation s^2_{kk}, and the three components of the stretching vectors $\omega_k s_{ki}$ and $\omega_i s_{kk}$ indicated a highly intermittent behaviour which is characterized by bursts of high amplitude followed by less violent periods. The results also show that the mean values of all these quantities are considerably smaller than their r.m.s. values, which suggests that time-averaged vorticity transport equations are of very limited value in understanding vorticity related phenomena.

Table 5 summarizes the conclusions for the parameters that were investigated in this work and their response to an increase of the mean flow Mach number and an increase in the mesh size/Re_M.

The financial support provided by NASA Grant #NAG-1590 monitored by Mr Dennis Bushnell and by AFOSR Grant #F49620-98-0358 monitored by Dr Steve Walker is greatly acknowledged.

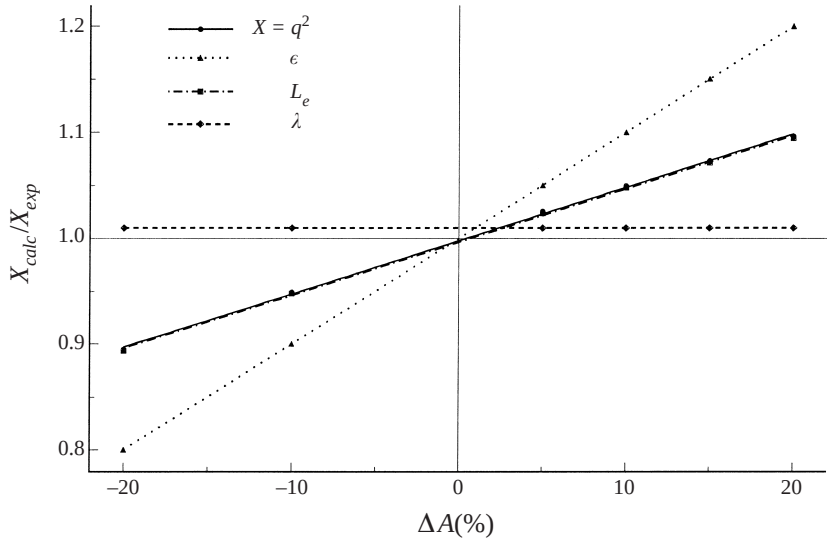

FIGURE 39. Effects of variation of A on several flow parameters.

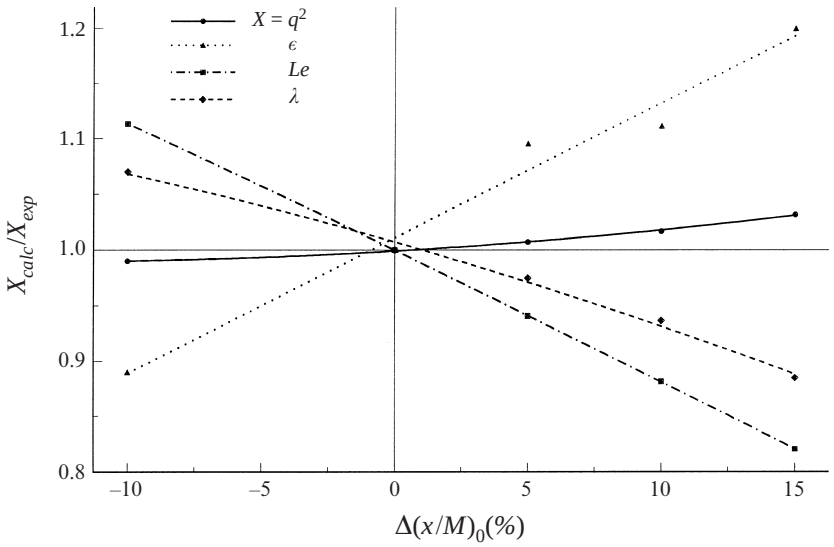

FIGURE 40. Effects of variation of $(x/M)_0$ on several flow parameters. Symbols as figure 39.

Appendix. Sensitivity analysis of decay relations

The sensitivity of the power law coefficients A, $(x/M)_0$, and n to changes of the level of the average values of the turbulent kinetic energy was found by introducing modified values of turbulent kinetic energy, within the limit of their uncertainties, into the optimization algorithm to determine the new values of these coefficients and subsequently their effect on the dissipation rate of kinetic energy, ϵ, the dissipative length scale, L_e and Taylor's microscale λ.

When the values of kinetic energy were allowed to change consistently and uniformly for all measurements, then the effect was only felt in A and ϵ, which changed by the same amount, while the dissipative length scale (L_e) changed by approximately half as much and Taylor's microscale (λ) by much less. For example, if the values of

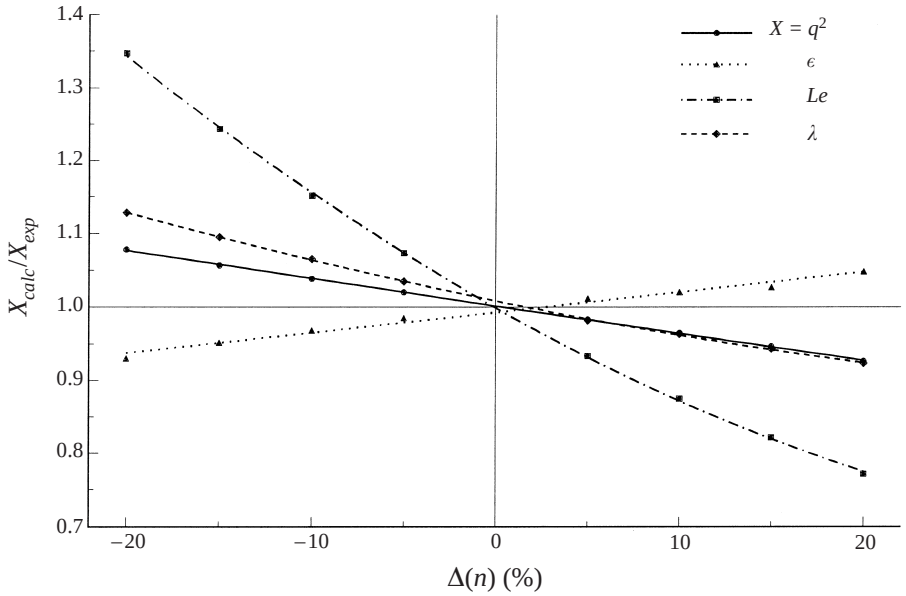

FIGURE 41. Effects of variation of n on several flow parameters. Symbols as figure 39.

kinetic energy were consistently increased by 10% then A and ϵ increased by 10%, L_e increased by approximately 5%, and λ increased from 3% to less than 1% depending on x/M. For larger sizes of λ (greater x/M) the least deviation from the reported values was found. The opposite trend was found when the values of turbulent kinetic energy were consistently decreased by 10%.

Turbulent kinetic energy was also allowed to vary in an alternating fashion. Thus every other measurement was allowed to increase or decrease by 10%, i.e. the first measurement was increased by 10%, the second was decreased by 10%, the third was increased by 10% and so on. The effect was felt, as expected, on all coefficients of the power law: A decreased by 20%, the position of the virtual origin increased by 15% and the power exponent decreased by 26%. As a result, the dissipation rate of kinetic energy decreased by 17%, the dissipative length scale increased between 6.7% and 20% and Taylor's microscale increased by 4% to 10% depending on x/M. The opposite trend was found for all power-law coefficients and flow field parameters when the first measurement was decreased by 10%, the second increased, etc.

Since all data were acquired simultaneously at multiple locations in the flow field, the uncertainty associated with the measurements of velocity fluctuations is expected to be consistent for all measured locations. Therefore the first case, where consistent variation was applied to the measured kinetic energy fluctuations, will provide the most probable estimate of the uncertainty propagation in the computation of ϵ, L_e and λ. That is, a maximum change of 10% in ϵ, 5% in L_e and 3% in λ can be assumed if a 10% perturbation in the values of turbulent kinetic energy is introduced.

In addition to the above, several tests were performed to determine the effects of variation of the coefficients of the power law individually on q^2, ϵ, L_e and λ. Figure 39 presents the effect of the decay coefficient variation on the above-mentioned flow parameters; the virtual origin $(x/M)_0$, and the decay exponent were kept constant. It can be seen that the fluctuations of kinetic energy and the dissipative length scale react linearly to the variation of A. For a $\pm 20\%$ variation in A, q^2 and L_e vary up to

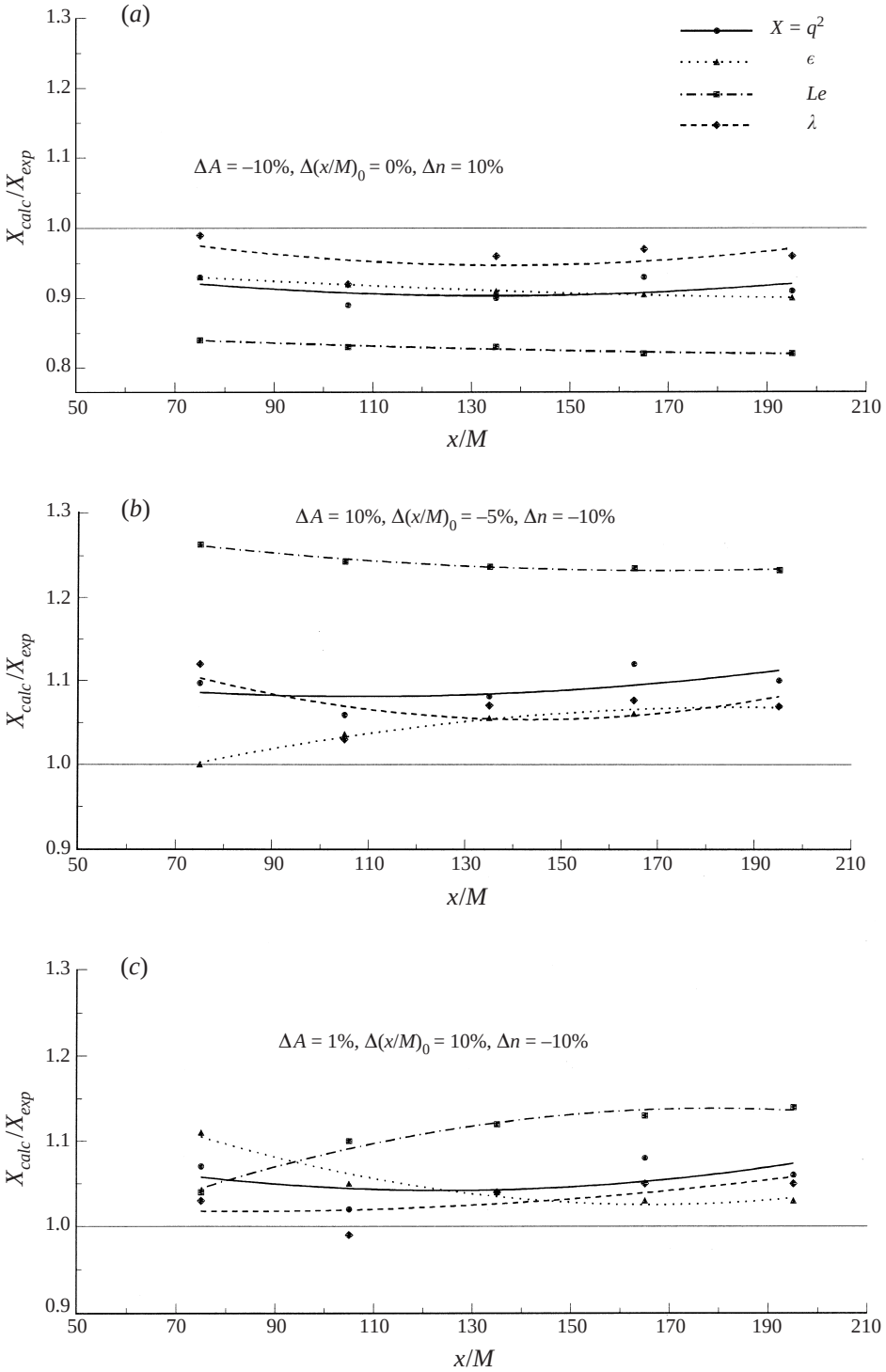

FIGURE 42 (*a–c*). For caption see facing page.

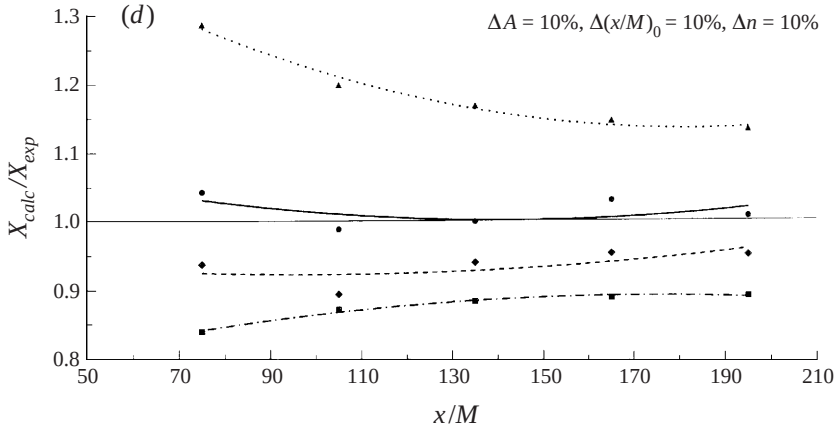

FIGURE 42. Effects of ΔA, $\Delta(x/M)_0$ and Δn variation on several flow parameters.

$\pm 10\%$. Similar behaviour is found for ϵ where for $\pm 20\%$ variation in A there is the same variation in ϵ. Taylor's microscale is insensitive to the variation of A.

The effect of change of the location of the virtual origin is shown in figure 40. It can be seen that there is a minimal effect on turbulent kinetic energy while for $\pm 10\%$ variation in the location of the virtual origin none of the flow parameters is affected more than $\pm 12\%$. Of interest is also the inversely proportional trend of the variation of L_e and λ on $\Delta(x/M)_0$. Again here the variation of ϵ is proportional to the variation applied (i.e. $\Delta(x/M)_0$).

The effect of variation of the decay exponent (n) on the flow parameters was also examined by performing an analysis with a $\pm 20\%$ variation of its original value. The results of this test are shown in figure 41. The first observation is that q^2 and ϵ were not affected more than $\pm 7\%$; the second is that L_e and λ were nonlinearly affected by the variation of n with L_e being affected most when n was decreased.

These results indicate that individual variations of the decay coefficients up to $\pm 10\%$ produced, in most of the cases, variations in the flow parameters less or at most equal to 10% for q^2, ϵ or λ and up to 15% for L_e. The question that remains to be answered is what are the combined effects of concurrent variations of the decay coefficients on the flow parameters. Because of the multiple combinations in the variation of the decay coefficients, only a few cases will be presented here to illustrate the combined effects. Several of these cases are presented in figure 42. It is interesting to investigate if the resultant effect will compound or be additive. In the first case, regardless of the variation of the decay coefficients, the change will keep adding and therefore it will never cancel out. If the second case holds then it is possible to cancel the various partial effects in one or more flow parameters. Indeed if we will consider the combined variation introduced by the variation of the individual power law coefficients (shown in figures 39 to 41) then it can be verified for the different cases presented in figure 42 that the average total effect on q^2 and ϵ appears to be approximately additive and not compound. The same behaviour does not hold for L_e and λ.

Nevertheless figure 42 shows that even if each of the power-law coefficients is overestimated by 10% the total effect propagated in q^2 is minimal, while the dissipative length scale and Taylor's microscale will be underestimated by 13% and 7% respectively. Overestimation of the dissipation rate of kinetic energy will occur in the order of 20%.

From all of the above results, it can be concluded that the flow parameters remain within reasonable limits of deviation even when the power-law coefficients are allowed to vary in an arbitrary manner.

REFERENCES

Andreopoulos, J. 1981 Comparative test of the response to pitch angles of various digital hot wire techniques. *Rev. Sci. Instrum.* **52**, 1376.

Andreopoulos, J. 1983*a* Improvements of the performance of triple hot wire probes. *Rev. Sci. Instrum.* **54**, 733.

Andreopoulos, J. 1983*b* Statistical errors associated with turbulence intensity and probe geometry in hot-wire anemometry. *J. Phys.* E: *Sci. Instrum.* **16**, 1264.

Andreopoulos, Y., Agui, J. H. & Briassulis, G. 2000 Shock wave–turbulence interactions. *Ann. Rev. Fluid Mech.* **32**, 309.

Andreopoulos, J. & Honkan, A. 1996 Experimental techniques for highly resolved measurements of rotation, strain and dissipation rate tensors in turbulent flows. *Meas. Sci. Technol.* **7**, 1462.

Andreopoulos, J. & Muck, K. C. 1987 Some new aspects of the shock-wave boundary layer interaction in compression ramp corner. *J. Fluid Mech.* **180**, 405.

Balint, J., Wallace, J. M. & Vukoslavcevic, P. 1991 The velocity and vorticity vector fields of a turbulent boundary layer. Part 2. Statistical properties. *J. Fluid Mech.* **228**, 53.

Batchelor, G. K. 1953 *The Theory of Homogeneous Turbulence*. Cambridge University Press.

Batchelor, G. K. & Townsend, A. 1947 Decay of vorticity in isotropic turbulence. *Proc. R. Soc. Lond.* A **190**, 534.

Batchelor, G. K. & Townsend, A. A. 1949 The nature of turbulent motion at high wave numbers. *Proc. R. Soc. Lond.* A **199**, 238.

Bendat, J. S. & Piersol, A. G. 2000 *Random Data Analysis and Measurements Procedures*. Wiley.

Bennett, J. C. & Corrsin, S. 1978 Small Reynolds number nearly isotropic turbulence in a straight duct and contraction. *Phys. Fluids* **21**, 2129.

Betchov, R. & Lorenzen, C. 1974 Phase relations in isotropic turbulence. *Phys. Fluids* **17**, 1503.

Bradshaw, P. & Huang, G. P. 1995 The law of the wall in turbulent flow. *Proc. R. Soc. Lond.* A **451**, 165.

Briassulis, G. 1996 Interaction of isotropic an homogeneous turbulence with shock waves. PhD Thesis, City University of New York.

Briassulis, G., Agui, J., Andreopoulos, J. & Watkins, B. C. 1996 A shock tube research facility for high-resolution measurements of compressible turbulence. *Expl Therm. Fluid Sci.* **13**, 430.

Briassulis, G. & Andreopoulos, J. 1994 Unsteady pressure field in shock wave interaction with grid generated turbulence in a shock tube. *AIAA Paper* 94–2277.

Briassulis, G. & Andreopoulos, J. 1996 High resolution measurements of isotropic turbulence interacting with shock waves. *AIAA Paper* 96–0042.

Briassulis, G., Honkan, A., Andreopoulos, J. & Watkins, B. C. 1995 Applications of hot-wire anemometry in shock tube flows. *Exps. Fluids* **19**, 29.

Budwig, R., Zwart, P. J., Nguyen, V. & Tavoularis, S. 1995 Grid generated turbulence in compressible streams. *ASME 2nd Symp. on Transitional and Turbulent Compressible Flows, Aug. 1995.*

Compte-Bellot, G. & Corrsin, S. 1966 The use of contraction to improve the isotropy of grid-generated turbulence. *J. Fluid Mech.* **25**, 657.

Compte-Bellot, G. & Corrsin, S. 1971 Simple Eulerian time correlation of full- and narrow-band velocity signals in grid-turbulence, isotropic turbulence. *J. Fluid Mech.* **48**, 273.

Dryden, H. L. 1943 A review of the statistical theory of isotropic turbulence. *Q. Appl. Maths* **1**, 7.

Favre, A. 1965 Équations des gaz turbulents compressibles I. *J. Méc.* **4**, 361.

Frenkiel, F. N. & Klebanoff, P. H. 1971 Statistical properties of velocity derivatives in a turbulent field. *J. Fluid Mech.* **48**, 183.

Frenkiel, F. N., Klebanoff, P. H. & Huang, T. T. 1979 Grid turbulence in air and water. *Phys. Fluids* **22**, 1606.

George, W. K. 1992 The decay of homogeneous isotropic turbulence. *Phys. Fluids* A **4**, 1492.

Groth, J. & Johansson, A. V. 1988 Turbulence reduction by screens. *J. Fluid Mech.* **197**, 139.

GUTMARK, E. J., SCHADOW, K. C. & YU, K. H. 1995 Mixing enhancement in supersonic free shear flows. *Ann. Rev. Fluid Mech.* **27**, 375.

HESSELINK, L. & STURTEVANT, B. 1988 Propagation of weak shocks through a random medium. *J. Fluid Mech.* **196**, 513.

HONKAN, A. & ANDREOPOULOS, J. 1992 Rapid compression of grid-generated turbulence by a moving shock wave. *Phys. Fluids* A **4**, 2562.

HONKAN, A. & ANDREOPOULOS, Y. 1997 Vorticity, strain-rate and dissipation characteristics in the near-wall region of turbulent boundary layers. *J. Fluid Mech.* **350**, 29 (referred to herein as HA).

HONKAN, A., WATKINS, C. B. & ANDREOPOULOS, J. 1994 Experimental study of interactions of a shock wave with free stream turbulence. *Trans. ASME*: *J. Fluids Engng* **116**, 763.

KELLER, J. & MERZKIRCH, W. 1990 Interaction of a normal shock with a compressible turbulent flow. *Exps. Fluids* **8**, 241.

KISTLER, A. L. & VREBALOVICH, T. 1966 Grid turbulence at large Reynolds numbers. *J. Fluid Mech.* **26**, 37.

KLEBANOFF, P. S. 1954 Characteristics of turbulence in a boundary layer with zero pressure gradient. *NACA TN* 3178.

KLEWICKI, J. C. 1989 On the interactions between the inner and outer region motions in turbulent boundary layers. PhD dissertation, Michigan State University.

KOVASZNAY, L. S. G. 1950 The hot-wire anemometer in supersonic flows. *J. Aeronaut. Sci.* **17**, 565.

KUO, A. Y. & CORSSIN, S. 1971 Experiments on internal intermittency and fine structure distribution functions in fully turbulent flows. *J. Fluid Mech.* **50**, 285.

LAWS, E. M. & LIVESEY, J. L. 1978 Flow through screens. *Ann. Rev. Fluid Mech.* **10**, 247.

LEE, L., LELE, S. K. & MOIN, P. 1993 Direct numerical simulation of isotropic turbulence interacting with a weak shock wave. *J. Fluid Mech.* **251**, 533.

LELE, S. K. 1994 Compressibility effects on turbulence. *Ann. Rev. Fluid Mech.* **26**, 211.

LEMONIS, G. C. 1995 An experimental study of the vector fields of velocity and vorticity in turbulent flows. Doctoral Thesis, Swiss Federal Institute of Technology, Institute of Hydromechanics and Water Resources.

MILS, R. R., KISTLER, A. L., O'BRIEN, V. & CORSSIN, S. 1958 Turbulence and temperature fluctuations behind a heated grid. *NACA TN* 4288.

MOHAMED, S. M. & LARUE, C. J. 1990 The decay power law in grid generated turbulence. *J. Fluid Mech.* **219**, 195.

MORKOVIN, M. V. 1956 Fluctuations and hot-wire anemometry in compressible flows. *AGARDOgraph* 24.

SIMMONS, L. F. G. & SALTER, C. 1934 Experimental investigation and analysis of the velocity variation in turbulent flow. *Proc. R. Soc. Lond.* A **145**, 212.

SMITS, A. J. & MUCK, K. C. 1987 Experimental study of three shock wave/boundary layer interactions. *J. Fluid Mech.* **182**, 291.

SPALART, P. R. 1988 Direct simulation of a turbulent boundary layer up to $R_\theta = 1410$. *J. Fluid Mech.* **187**, 61.

SPINA, E. F., SMITS, A. J. & ROBINSON, S. K. 1994 The physics of supersonic turbulent boundary layers. *Ann. Rev. Fluid Mech.* **26**, 287.

STEWART, R. W. & TOWNSEND, A. A. 1951 Similarity and self preservation in isotropic turbulence. *Phil. Trans. R. Soc.* A **243**, 359.

TAN-ATICHAT, J., NAGIB, H. M. & LOEHRKE, R. I. 1982 Interaction of free-stream turbulence with screens and grids: a balance between turbulence scales. *J. Fluid Mech.* **114**, 501.

TAVOULARIS, S., BENNETT, J. C. & CORRSIN, S. 1978 Velocity derivative skewness in small Reynolds number, nearly isotropic turbulence. *J. Fluid Mech.* **88**, 63.

TENNEKES, H. & LUMLEY, J. L. 1972 *A First Course in Turbulence.* MIT Press.

TSINOBER, A., KIT, E. & DRACOS, T. 1992 Experimental investigation of the field of velocity gradients in turbulent flows. *J. Fluid Mech.* **242**, 169.

WILKS, J. 1962 *Mathematical statistics.* Wiley.

WYNGAARD, J. C. 1969 Spatial resolution of the vorticity meter and other hot-wire Arrays. *J. Phys.* E: *Sci: Instrum.* **2**, 983.

ZEMAN, O. 1990 Dilatation dissipation: the concept and application in modeling compressible mixing layers. *Phys. Fluids* A **2**, 178.

ZWART, P., BUDWIG, R. & TAVOULARIS, S. 1997 Grid turbulence in compressible flow. *Exps. Fluids* **23**, 550.